

DISSERTATION
SUBMITTED TO THE
COMBINED FACULTIES FOR THE NATURAL SCIENCES AND FOR MATHEMATICS
OF THE RUPERTO-CAROLA UNIVERSITY OF HEIDELBERG, GERMANY
FOR THE DEGREE OF
DOCTOR OF NATURAL SCIENCES

Put forward by

Diplom-Physicist: Victoria Zinyuk

Born in: Moscow, Russia

Oral examination: May 10, 2016

SYSTEMATIC STUDY OF STRANGENESS PRODUCTION AND DYNAMIC
BEHAVIOUR WITH THE FOPI EXPERIMENT AT SIS-18

Referees:

Prof. Dr. Norbert Herrmann

Prof. Dr. Jürgen Schaffner-Bielich

Kurzfassung

Die vorliegende Arbeit beschäftigt sich mit der Untersuchung der Eigenschaften seltsamer Teilchen im nuklearen Medium.

Die Erzeugung und Ausbreitung von K^+ und K^- Mesonen in der nuklearen Materie wird mit Hilfe des FOPI-Spektrometers in $^{58}\text{Ni} + ^{58}\text{Ni}$ Kollisionen untersucht. Die verwendete Einschussenergie von $E_{beam} = 1,91$ AGeV liegt nah der Produktionsschwelle für seltsame Teilchen. Ein schwacher, den Protonen entgegen gerichteter Fluss in der Reaktionsebene, sowie eine geringe dazu senkrecht gerichtete Emission ist in der Azimuthalverteilung der K^+ Mesonen beobachtet worden. Die Emission von K^- Mesonen ist, im Rahmen großer statistischer Unsicherheiten, isotrop. Der Vergleich mit zwei unabhängigen Transportrechnungen, HSD und IQMD, suggeriert ein schwach abstoßendes KN -Potential von $U_{KN} = 20 \pm 5$ MeV und ein attraktives $\bar{K}N$ -Potential von $U_{\bar{K}N} = -40 \pm 10$ MeV.

Die Produktion von $K^{+/-/0}$, ϕ Mesonen und dem Λ Baryon wird in π^- -induzierten Reaktionen mit C, Cu und Pb Targets bei einem Einschussimpuls von $p_{\pi^-} = 1.7$ GeV/c untersucht. Aus dem Vergleich der Phasenraumverteilungen aus der Produktion im leichten und im schweren Target, wird geschlossen, dass die K^+ und K_S^0 Mesonen eine Abstoßung in nuklearen Medium erfahren. Bei dem letzteren, alleinig auf die starke Wechselwirkung zurückzuführen. Der analoge Vergleich für K^- Mesonen suggeriert eine starke Absorption in nuklearen Medium. Die beobachtete Menge der ϕ Mesonen unterstützt die Vermutung eines Z^α -Skalierungsverhaltens des Produktionswirkungsquerschnitts.

Abstract

This work is dedicated to the investigation of in-medium behaviour of strange particles.

In-medium production and propagation of K^+ and K^- mesons is studied with the FOPI apparatus in $^{58}\text{Ni} + ^{58}\text{Ni}$ collisions at the incident beam energy of $E_{beam} = 1.91$ AGeV, i.e. near the strangeness production threshold energies. Weak in-plane ‘anti-flow’ with respect to protons and a slight ‘squeeze-out’ is found in the azimuthal emission pattern of K^+ mesons. K^- mesons exhibit an isotropic emission pattern within large statistic uncertainties. The comparison to the predictions of two independent transport calculations, HSD and IQMD, suggests a weakly repulsive KN in-medium potential of $U_{KN} = 20 \pm 5$ MeV and an attractive $\bar{K}N$ in-medium potential of $U_{\bar{K}N} = -40 \pm 10$ MeV.

Production of $K^{+/-/0}$, ϕ mesons and the Λ baryon at normal nuclear matter density is studied in $\pi^- + A$ reactions with C, Cu and Pb targets at incident beam momentum of $p_{\pi^-} = 1.7$ GeV/c. Differences in the final state phase space distributions measured in heavy and light targets point to repulsion for K^+ and K_S^0 mesons in nuclear medium. The latter is solely attributed to the strong interaction. The corresponding comparison for K^- mesons suggests a strong absorption in nuclear medium. Observed ϕ meson yields support the hypothesis of Z^α -scaling of the production cross section.

Contents

1	Introduction	5
1.1	Structure of this Work	7
2	Strange Particles in Nuclear Medium	10
2.1	Chiral Symmetry – Breaking and Partial Restoration	10
2.2	K Mesons in Nuclear Matter	12
2.3	Light Vector Mesons in Nuclear Matter	16
2.4	Transport Calculations	18
2.4.1	IQMD	18
2.4.2	HSD	19
3	The FOPI Experiment	21
3.1	Setup of the FOPI Detector	21
3.2	Detector Acceptance	24
3.3	Particle Identification (PID)	25
3.4	The S325 Experiment	26
3.4.1	Trigger	27
3.5	The S339 Experiment	29
3.5.1	Trigger	30
4	The S325 Experiment	32
4.1	Reconstruction of Charged Kaons	33
4.1.1	Finite Lifetime Correction	38
4.2	Asymmetries in the Azimuthal Emission Pattern	39
4.2.1	Fourier Expansion of the Azimuthal Particle Distribution	39
4.2.2	Reaction Plane Reconstruction	41
4.2.3	Reaction Plane Resolution: Ollitrault Corrections	42
4.2.4	Anisotropies of the Reaction Plane Distribution	43
4.2.5	Systematic Errors	44
4.3	Centrality Selection	44
4.4	Systematic Investigation of Flow Patterns	47
4.4.1	Influence of the Coulomb Interaction on the In-Plane Emission Pattern	48
4.4.2	First Fourier Coefficient	51
4.4.3	Second Fourier Coefficient	54

5	The S339 Experiment	58
5.1	Charged Particles in C, Cu und Pb Targets	59
5.2	Reconstruction of K^+ and K^- Mesons	62
5.3	Reconstruction of Neutral Particles	67
5.3.1	Combinatorial Background	68
5.4	The ϕ mesons	70
5.4.1	Reconstruction Efficiency	72
5.4.2	The Transparency Ratio	74
5.5	The Λ Baryons	76
5.6	The K_S^0 meson	82
5.6.1	Investigation of the Combinatorial Background	83
5.6.2	Reconstruction Efficiency Considerations	86
5.6.3	Phase Space Distributions of K_S^0 Mesons from Reactions with Dif- ferent Targets	88
5.7	Transport Model Comparison	89
6	Conclusion	94
A	Journal Publication on Charged Kaon Flow	97
B	Supplementary Graphics	104
B.1	Neutral Kaons in S339 Experiment	104
B.1.1	Reconstruction Efficiency of K_S^0 Mesons	111
B.2	Identification of K^+ mesons in S339 Experiment	112
C	Centrality Selection in IQMD	115
D	Kinematic Variables	116
E	Supplimentary Information of the Targets of the S339 Beam Time	118
F	Strangeness Production Cross Sections in Pion-Induced Reactions	120

Chapter 1

Introduction

One of the biggest discoveries in modern physics was the discovery of the Higgs boson in 2013. After the ATLAS and CMS collaborations announced an independent measurement of a statistically significant excess in the expected decay channels, François Englert and Peter W. Higgs were awarded the nobel prize, according to the laudatio “for the theoretical discovery of a mechanism that contributes to our understanding of the origin of mass of subatomic particles, and which recently was confirmed through the discovery of the predicted fundamental particle, by the ATLAS and CMS experiments at CERN’s Large Hadron Collider”. In the standard model of particle physics, the masses of elementary particles, i.e. quarks and gauge bosons, are generated by their interaction with the Higgs field.

In ‘ordinary matter’ quarks are bound into protons and neutrons by the strong interaction (QCD). The total mass of these hadrons is only to a small extend determined by the quark masses. A proton, consisting of 3 quarks $\langle uud \rangle$, has a mass of $M_p \sim 1 \text{ GeV}/c^2$, whereas the sum of its (current) quark masses¹ is $\sum m_i \sim 15 \text{ MeV}/c^2$. The remaining, major contribution is attributed to the mechanism of the spontaneous breaking of the chiral symmetry.

Chiral symmetry is a fundamental symmetry of the strong interaction. It states that the interaction is the same for a particle and its mirror image. In the limit of vanishing bare quark masses, chiral symmetry is an exact symmetry. Since the bare quark masses are small, the symmetry is still approximately fulfilled. It is referred to as the (negligible) explicit breaking of the chiral symmetry. In nature, the chiral symmetry is additionally broken spontaneously by the so-called scalar quark condensate, which fills up the QCD vacuum. The expectation value of the quark condensate is closely connected to the mass generation mechanism of hadrons. The manifest consequence is the creation of $\sim 99 \%$ of the nucleon mass.

The large expectation value of the quark condensate decreases with increasing temperature and density. Thus, the chiral symmetry is expected to be partially restored in hot and/or dense nuclear matter. The physical consequence is a modification of hadron properties. Compressed and heated strongly interacting matter can be experimentally

¹There are two common definitions of a ‘quark mass’: The *current quark mass* - the bare quark mass, generated by the Higgs mechanism, and the *constituent quark mass* - the binding energy of a quark in a hadron.

created in heavy ion reactions, therefore opening the possibility to test the fundamental concepts of strong interaction in the laboratory.

Hadronic models were developed to quantify the influence of the medium on the observable properties of hadrons. Predictions for mesons like ρ , ω , η' and ϕ foresee a shift of in-medium mass compared to the mass in vacuum, and a broadening of the spectral function. So far, only the mass of the η' was observed to be lowered by the interaction with the medium. The TABS collaboration reported a mass shift of $\Delta m \approx 40 \pm 10$ MeV [Nan13]. No evidence of a dropping of in-medium mass was found in the line shape analysis of vector mesons: ω mesons [Nan10, Thi13], ρ mesons [Nas07, Nar06] and ϕ mesons [Ish05]. On the other hand, all mesons mentioned above were observed to experience in-medium broadening, which was attributed to inelastic processes (ω mesons [Kas07, Kot08]; ρ mesons [Nas07]; ϕ mesons [Har12, Pol11] and η' meson [Nan12]). The contribution from a possible restoration of the chiral symmetry remains a matter of debate.

In the mean-field picture, the interaction between hadrons and the medium can be seen as an attraction or repulsion, depending on the particle species. In this representation it is evident that mesons and nucleons can form bound states. Evidence for deeply bound pionic states in Pb and Sn isotopes were found at FRS@GSI Darmstadt [Ita00, Suz04]. Also the η' -nucleus and ω -nucleus bound states are predicted [Mar01]. Especially the η' meson is considered to be a good candidate for a meson-nucleon bound state due to its small width.

Of particular interest is the in-medium behaviour of strange particles. Strangeness is exactly conserved in strong interactions. Consequently the absorption of a produced strange particle requires another strange particle with the reverse strangeness content. Strangeness can be produced in kaon² - antikaon³ pairs or by simultaneous kaon-hyperon⁴ production. The reaction requiring least energy to produce a $s\bar{s}$ pair is the reaction $NN \rightarrow N\Lambda K^+$ with a threshold energy of $E_{beam} = 1.58$ GeV in a fixed target experiment. In heavy-ion collisions kaon production is possible even below this energy, i.e. sub-threshold. Additional energy can be provided by the Fermi motion of the nucleons or accumulated in multi-step processes using nuclear resonances as energy reservoirs. Sub-threshold production ensures that the kaons are produced in the high density phase of the collision. Consequently it is particularly interesting for the study of in-medium effects.

Once produced, a K^{+0} meson has no counterpart to annihilate with and can leave the fireball. The resulting long mean free path makes these particles a good penetrating probe for the hot and dense phase of the collision. The final state properties of kaons are influenced only by the elastic interactions with the nucleons and propagation in potentials.

The cheapest way to produce a K^- is in strangeness-exchange reactions: $\Lambda(\Sigma)\pi \rightarrow K^-N$. It is the main source of K^- in heavy-ion collision at the considered energies, since the threshold energy for the direct production in $NN \rightarrow NNK^+K^-$ reactions of E_{beam}

²I.e. $K^+(\bar{u}s)$ and $K^0(\bar{d}s)$.

³I.e. $K^-(u\bar{s})$ and $\bar{K}^0(d\bar{s})$.

⁴Hyperons are baryons containing one or more strange quark. For the current discussion only the lightest hyperons, i.e. $\Lambda(uds)$ and the Σ -triplet: $\Sigma^-(dds)$, $\Sigma^0(uds)$, $\Sigma^-(uus)$ are of interest.

$= 2.5$ GeV can not be reached. In contrast to K^+ , K^- are likely to be reabsorbed due to the large cross section and the exothermic nature of the inverse reaction $K^- N \rightarrow \Lambda(\Sigma)\pi$. As a result, antikaons observed in the final state are likely to be created close to the surface and are not influenced by the strongly interacting medium.

Though challenging, the measurement of a possible in-medium modification of antikaons' properties is especially compelling. A strong reduction of the in-medium mass of K^- mesons could have dramatic consequences for the stability of neutron stars. In this scenario a K^- condensate builds up in the interior of a neutron star, adding additional negative charge and thus requiring an increasing of the proton fraction. The result is a softer equation-of-state of the neutron star, which puts restrictions on its maximal mass [Lat07, Wei12]. However, recent astrophysical observation of a neutron star as heavy as two solar masses rules out some of the K^- condensate scenarios [Dem10]. Furthermore, if the attraction between K^- and nucleons is strong enough, it could lead to kaonic atoms, i.e. deeply bound K^- states [Aka02].

Conclusions about the existence and strength of the K^-N in-medium potential can be derived from the comparison of experimental observations to transport model calculations. Transport models simulate the collisions by taking into account all relevant cross sections and potentials. If the reabsorption and scattering cross sections are known and implemented realistically, their contribution to the final phase space distribution of antikaons can be disentangled from the K^-N interaction of interest.

A lot of experimental effort was dedicated to the search for in-medium properties of kaons and antikaons. Heavy-ion experiments KaoS, FOPI and HADES, operating at the heavy-ion synchrotron (SIS) of GSI, delivered high precision data on the production and propagation of kaons and antikaons in heavy systems. All measurements point to the existence of a weakly repulsive KN interaction. The conclusions on the strength, however, are strongly model dependent. The investigation of K^- mesons in SIS energy regime is additionally complicated by the small production rate. So far, it has not been possible to establish the magnitude or even the existence of the $\bar{K}N$ in-medium potential.

1.1 Structure of this Work

The analysis presented in this work is focused on the investigation of the effects nuclear medium of different density and temperature has on the production and propagation of K^+ , K^- , K_S^0 , ϕ mesons, and the Λ baryons.

The collective motion of charged kaons in nuclear matter compressed to $2-3 \rho_0^5$ and heated to ~ 100 MeV is studied in $^{58}\text{Ni}+^{58}\text{Ni}$ collisions at the beam energy of $E_{beam} = 1.9$ AGeV (internal name 'S325(e)'). The production of $K^{+/-/0}$, ϕ and Λ at normal nuclear matter density is investigated in pion-induced reactions (internal name 'S339'). In the latter, conclusions on the influence by the medium are drawn from the comparison of the production in a light (Carbon) and heavy (Lead) nucleus.

The manuscript starts with an introduction of the basic concepts of chiral symmetry and the explicit and spontaneous symmetry breaking. Special emphasis is put on the

⁵ $\rho_0 = 0.16$ nucleons/fm³ is the normal nuclear matter density.

properties of the chiral condensate. The discussion of the general properties of QCD is followed by the effective theory description of the particles of interest. The in-medium effective mass of kaons is derived in the framework of chiral perturbation theory. Since the same approach is not applicable to antikaons in medium, the idea and the basic procedure of a coupled channel calculation is sketched. Possible in-medium modifications of ϕ , a light vector meson, are elaborated on the basis of hadronic model predictions. Chapter 2 closes with a short description of the two transport models which are used to interpret the experimental data. The key principles and the implementation of the in-medium potentials for kaons and antikaons are summarised.

Chapter 3 is devoted to the experimental setup. The relevant sub-detectors of the FOPI spectrometer are portrayed by their operation principle and measuring capabilities. Detector limitations in terms of resolution and acceptance are demonstrated. The general strategy of particle identification within the FOPI setup is explained. Both runtimes which delivered data for the following analysis are characterised by relevant experimental details such as trigger conditions and measured cross sections.

Chapter 4 summarises the analysis of the S325(e) experiment. In this experiment possible in-medium modifications of charged K mesons are investigated by the means of their collective motion, referred to as ‘flow’. The chapter starts with technical details of the analysis, explaining the identification procedure for charged kaons with FOPI and showing its results. Furthermore, the principle of how the information about the collective motion is reconstructed from the final state phase space distribution of a particle is clarified. Necessary corrections due to experimental limitations are addressed. The obtained flow patterns are compared to HSD and IQMD transport model calculations. Within this comparison certain properties, such as the contributions from the Coulomb interaction to the flow pattern, its centrality and momentum dependence as well as a possible modification due to the interaction with the strong medium, are studied. Additionally, the results of the present analysis are compared to earlier measurements published by FOPI and KaoS collaborations.

In Chapter 5 the analysis of the S339 experiment is presented. For the study of the in-medium production, the signals of $K^{+/-/0}$, ϕ meson and the Λ baryon were reconstructed. Details, strategy and challenges of the particular reconstructions are pointed out.

The electrically neutral particles ϕ and K_S^0 mesons do not leave a trace in the FOPI detector, but decay within the apparatus due to their short lifetime and can be reconstructed from their decay products. The strategy, topological selection and the results of such a reconstruction are discussed. The background estimation by a so-called ‘mixed event method’ is explained. The reconstruction efficiency is evaluated with a Monte Carlo based GEometry ANd Tracking simulation-Geant. Special emphasis is put on the differences in reconstruction efficiency for the carbon and lead targets, as the comparison is symptomatic of the in-medium effects.

A signature for in-medium modification is seen in the difference of the momentum distributions of a particle produced in the light compared to the one originating from the heavy target. Expectations for an attraction and repulsion scenario are explicated, as well as the actual measurements for $K^{+/-/0}$ mesons and the Λ baryon. Measured signatures are compared to the available transport calculations and discussed in the

context of previous measurements.

The yields of ϕ mesons, produced in different targets, are compared within the so - called ‘transparency ratio’.

The work is concluded with a discussion of the results from both experiments in Chapter 6.

Chapter 2

Strange Particles in Nuclear Medium

The investigation of low energy behaviour of Quantum Chromodynamics (QCD) and especially the so-called in-medium effects has been the motivation behind many experiments of the FOPI collaboration and, in particular, the analysis presented in this work. The aim of this section is to provide the connection between fundamental properties of QCD and the experimentally accessible final state observables. Therefore, a short overview of the theoretical concept of chiral symmetry – its breaking and partial restoration in hot and dense nuclear matter – is given (based on [Koc97]). Possible modifications of hadron properties are discussed as well as the concept and basic principles of transport calculations, which are used to evaluate the influence of the nuclear medium later on in this work.

2.1 Chiral Symmetry – Breaking and Partial Restoration

Consider the QCD Lagrangian. The only way mass enters in the equation is in the form of explicit quark-mass terms. For ordinary matter only the up (u) and down (d) quark flavours need to be considered. The current u- and d-quark masses (5-10 MeV/ c^2) are much smaller than the QCD energy scale, characterized by the $\Lambda_{QCD} \approx 217$ MeV. Therefore, the mass term can be seen as a small perturbation to the Lagrangian and, to a good approximation, neglected.

In the limit of massless quarks, the QCD Lagrangian reads

$$\mathcal{L}_{QCD} = \bar{\psi}_L(i \not{D})\psi_L + \bar{\psi}_R(i \not{D})\psi_R + \mathcal{L}_{glue} \quad (2.1)$$

where $\psi = (u, d)^T$ is a vector in the flavour space.

This Lagrangian is invariant under rotating the left-handed and the right-handed components independently in the two dimensional flavour space. The transformation can be described by unitary matrices U_L and U_R , i.e. QCD Lagrangian(2.1) has the $U(2)_L \times U(2)_R$ chiral symmetry, which can be decomposed into $SU(2)_L \times SU(2)_R \times U(1)_V \times U(1)_A$.¹

¹For N ‘light’ quark flavours (especially N=3, i.e. u, d and s) the corresponding symmetries is

Symmetries of the Lagrangian lead to conserved quantities (currents). The singlet vector symmetry, $U(1)_V$, corresponds to baryon number conservation. The singlet axial symmetry, $U(1)_A$, is explicitly violated and does not correspond to a conserved quantity. However, it is not of interest here. Relevant for the following discussion is the remaining component. Following Noether's theorem, the $SU(2)_L \times SU(2)_R$ chiral symmetry leads to conserved vector V_μ and axial-vector A_μ currents.

Chiral symmetry implies that hadrons have chiral partners, i.e. hadron multiplets with equal quantum numbers but different chiralities. The axial transformation, associated with the axial-vector current rotates the states into each other. Hence, the states are expected to have equal Eigenvalues, i.e. equal mass. The mass degeneracy is nearly realised between proton and neutron and for the three pion states, but not observed in many other cases like ρ_0 and a_1 mesons. The experimentally observed mass difference is too large to be attributed to the current quark masses. On the other hand, there is experimental evidence supporting the partial² conservation of axial-vector current. The axial-vector symmetry is considered to be spontaneously broken. ‘Spontaneous breaking’ means the symmetry is realised in the Lagrangian but not in the ground state – the vacuum. The QCD vacuum breaks the symmetry by forming a quark condensate. The quark condensate is partially responsible for giving hadrons mass.

In the framework of chiral perturbation theory (ChPT), some properties of the quark condensate, relevant for the physics of hot and dense matter, can be derived:

Temperature dependence:

To the leading order, changes in the quark condensate are expected to be small, i.e. a drop $\sim T^2$

$$\langle \bar{q}q \rangle_T = \langle \bar{q}q \rangle_0 \left(1 - \frac{T^2}{8f_\pi^2}\right), \quad (2.2)$$

where $\langle \bar{q}q \rangle_0$ is the expectation value of the quark condensate at temperature $T = 0$ and density $\rho = 0$. f_π denotes the pion decay constant.

ChPT is not expected to work well for higher temperatures. Lattice gauge calculations predict the temperature at which the quark condensate vanishes, i.e. the critical temperature. A current value from the calculations with $N_f = 3$ flavours is $T_C \approx 150$ MeV and with $N_f = 2$ flavours is $T_C \approx 170$ MeV [Kar01].

Density dependence:

The quark condensate is expected to drop linearly in density:

$$\langle \bar{q}q \rangle_\rho = \langle \bar{q}q \rangle_0 \left(1 - \frac{\Sigma_{\pi N}}{m_\pi^2 f_\pi^2} \rho + \dots\right). \quad (2.3)$$

$\Sigma_{\pi N}$ is the so-called pion-nucleon sigma term. It originates from the explicit symmetry breaking and contributes to the hadron mass. Its value is determined from pion-nucleon scattering to be $\Sigma_{\pi N} \simeq 45$ MeV [Hoe83]. With this value, already at normal nuclear matter density the quark condensate is expected to be reduced by 35 %:

$$\langle \bar{q}q \rangle_\rho = \langle \bar{q}q \rangle_0 \left(1 - 0.35 \frac{\rho}{\rho_0}\right), \quad (2.4)$$

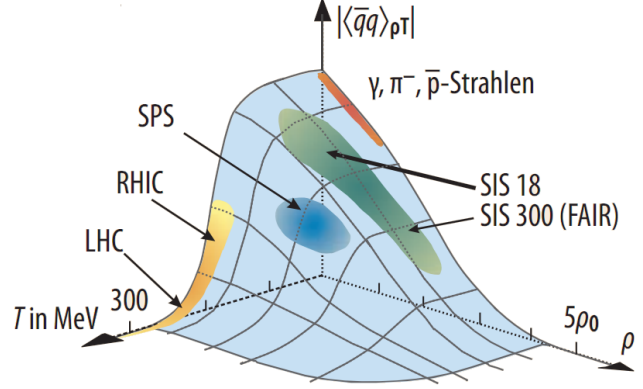
$SU(N)_L \times SU(N)_R \times U(1)_V \times U(1)_A$ and the chiral symmetry breaking is analogous.

²PCAC (partially-conserved axial-vector current). Small explicit symmetry breaking due to non-vanishing quark masses is assumed.

where ρ_0 is the normal nuclear matter density.

Temperature and density dependence of the quark condensate are illustrated in Fig. 2.1. Coloured surfaces show how by varying the beam energy and colliding systems, as realised by the different accelerator facilities, various stages of ‘hot and dense’ can be created.

Figure 2.1: The expectation value of the quark condensate as function of temperature (T) and density (ρ) [PJ09].



In heavy-ion collisions at the SIS-18 energy regime, where the FOPI experiment was operating, the created nuclear matter is heated up to temperatures of ~ 100 MeV and compression of about 2-3 ρ_0 net baryon density can be reached [Fuc06, Hon98].

In summary: chiral symmetry is broken explicitly by the current quark masses and spontaneously by the QCD vacuum. The QCD vacuum is ‘filled’ by the scalar quark condensate with a non-zero expectation value. The quark condensate is partially responsible for the masses of hadrons. Its expectation value reduces with increasing temperature and density, therefore partially restoring the chiral symmetry and altering the properties of hadrons in hot and/or dense nuclear matter.

The reduction of the quark condensate will be linked to the experimentally measurable properties of strange particles in the following section.

2.2 K Mesons in Nuclear Matter

The coupling constant of QCD increases with decreasing energy. Consequently the low energy behaviour of QCD can not be treated perturbatively. The common framework to describe the low energy dynamics of QCD is the chiral perturbation theory (ChPT) – an effective field theory. The idea of ChPT is that the low energy dynamics is determined by light hadrons (motivated by the confinement) and the symmetries of QCD. Hereby, the explicit breaking of chiral symmetry is considered to be negligibly small. An effective chiral Lagrangian is formulated respecting the relevant QCD symmetries and using hadrons as the degrees of freedom.

For the low energy pion-nucleon interaction ($SU(2)$ flavour sector), ChPT is considered to be an exact theory. ChPT has to be extended to the $SU(3)$ flavour sector to describe the properties of kaons in nuclear matter. Kaplan and Nelson were the first to formulate a chiral $SU(3)_L \times SU(3)_R$ Lagrangian [Kap86, Nel87].

The analysis of the full Kaplan - Nelson Lagrangian leads to a complicated coupled channel problem. To study the interaction between kaons and nucleons in a mean field approximation, an effective Lagrangian can be formulated based on kaon and nucleon degrees of freedom.

With kaon and nucleon fields given by

$$K = \begin{pmatrix} K^+ \\ K^0 \end{pmatrix}, \quad \bar{K} = (K^- \ K^0) \quad \text{and} \quad N = \begin{pmatrix} p \\ n \end{pmatrix}, \quad \bar{N} = (\bar{p} \ \bar{n}) \quad (2.5)$$

the effective Lagrangian reads:

$$\begin{aligned} \mathcal{L}_{eff} = & \bar{N}(i\gamma^\mu \partial_\mu - m_N)N + \partial^\mu \bar{K} \partial_\mu K - \left(m_K^2 - \frac{\Sigma_{KN}}{f_\pi^2} \bar{N}N \right) \bar{K}K \\ & - i \frac{3}{8f_\pi^2} \bar{N} \gamma^0 N \bar{K} \overleftrightarrow{\partial}_t K. \end{aligned} \quad (2.6)$$

Where m_N and m_K nucleon and kaon mass at rest, f_π the pion decay constant and Σ_{KN} the kaon - nucleon sigma term. For details of the derivation see [Fuc06] and references within.

The Lagrangian contains two terms describing the interaction between kaons and nucleons: The *vector interaction* (the last term in Eq. 2.6) – repulsive for kaons and attractive for antikaons and the attractive *scalar interaction* (the third term in Eq. 2.6). The latter results from the explicit chiral symmetry breaking and depends on the kaon - nucleon sigma term.

Under the assumption of $SU(3)_V$ symmetry, the full pseudoscalar meson octet can be seen as Goldstone bosons of chiral symmetry breaking. Therefore, the kaon mass can be related to the chiral condensate by the Gell - Mann - Oakes - Renner (GOR) relation [Gel68]:

$$m_K^2 = \frac{1}{2}(m_u + m_s) \langle \bar{u}u + \bar{s}s \rangle, \quad (2.7)$$

with $m_{u,s}$ the up- and strange-quark current masses.

Accordingly the kaon - nucleon sigma term reads:

$$\Sigma_{KN} = \frac{1}{2}(m_u + m_s) \langle N | \bar{u}u + \bar{s}s | N \rangle. \quad (2.8)$$

The numerical value of Σ_{KN} is restricted by measurements and different types of calculations (lattice QCD [Bro96 I, Don96, Bor02], heavy baryon ChPT [Bor99], chiral quark model calculations [Ino04]). Recent values range from $300 < \Sigma_{KN} < 450$ MeV.

Using the mean-field approximation for nucleon fields and applying the Euler-Lagrange equation, the in-medium Klein-Gordon Equation is obtained from Eq. 2.6:

$$\left[\partial_\mu \partial^\mu + i \frac{3}{4f_\pi^2} \rho_N \partial_t + \left(m_K^2 - \frac{\Sigma_{KN}}{f_\pi^2} \rho_S \right) \right] K = 0, \quad (2.9)$$

with nuclear density $\rho_N = \langle \bar{N} \gamma^0 N \rangle$ and scalar density $\rho_S = \langle \bar{N} N \rangle$.

From this the dispersion relation for kaons in nuclear matter can be deduced:

$$\omega^2(\mathbf{k}, \rho_N) = m_K^2 + \mathbf{k}^2 - \frac{\Sigma_{KN}}{f_\pi^2} \rho_S \pm \frac{3}{4} \frac{\omega}{f_\pi^2} \rho_N, \quad (2.10)$$

where \mathbf{k} is the three-momentum of the kaon and ‘+’ and ‘-’ refer to kaons and antikaons respectively. Rephrased in terms of kaon in-medium energy:

$$E(\mathbf{k}, \rho_N) = \left[m_K^2 + \mathbf{k}^2 - \frac{\Sigma_{KN}}{f_\pi^2} \rho_S + \left(\frac{3}{8} \frac{\rho_N}{f_\pi^2} \right)^2 \right]^{1/2} \pm \frac{3}{8} \frac{\rho_N}{f_\pi^2}. \quad (2.11)$$

The in-medium (effective) mass is defined as the in-medium energy for particles at rest, i.e. $E(\mathbf{k} \rightarrow 0, \rho_N)$. In the effective ChPT on the tree level as discussed so far, the effective mass reads:

$$m_K^* = \sqrt{m_K^2 - \frac{\Sigma_{KN}}{f_\pi^2} \rho_S + V_\mu V^\mu}. \quad (2.12)$$

Higher order corrections and their importance can be estimated from the kaon-nucleon scattering lengths.

Fig. 2.2 shows the density dependence of kaon in-medium energy and effective mass for the mean field ChPT calculations (solid lines) and the results of calculation including higher order corrections. The predictions agree in the general trend of a weak repulsion for kaons and strong attraction of antikaon by nuclear medium. More sophisticated calculations predict a large energy (mass) shift for kaons and antikaons. The experimental data (shaded bands) from measurements of K^+N scattering and K^- atoms [Bat97] suggest an even stronger effect. However, more recent measurements of kaonic hydrogen by the Siddharta collaboration [Baz11] and the interpretation of the data, do not support the depicted depth of the potential.

ChPT works well for the description of the KN interactions because kaons retain good quasi-particle properties in dense matter. Antikaons are different. In-medium properties of K^- are strongly influenced by their ability to form resonances with baryons and the appearance of the $\Lambda(1405)$ resonance near the K^-p threshold. A non-perturbative treatment is necessary.

The calculation of the two body kaon-nucleon scattering in the non-perturbative approach requires to solve the Bethe-Salpeter equation (here in schematic representation):

$$T_{KN \rightarrow KN} = V_{KN \rightarrow KN} - i \int V_{KN \rightarrow MB} G_B D_M T_{MB \rightarrow KN}, \quad (2.13)$$

where T is the two-body scattering amplitude and V the interaction kernel. G_B and D_M are the baryon and meson propagators respectively:

$$G_B(p) = \frac{1}{\not{p} - m_B + i\epsilon}, \quad D_M(k) = \frac{1}{k^2 - m_M^2 + i\epsilon}. \quad (2.14)$$

This approach contains the complete baryon ($B = N, \Lambda, \Sigma$) and pseudoscalar meson ($M = \pi, K$) octet as the degrees of freedom in the chiral Lagrangian and therefore is a coupled channel calculation. This ansatz pursues the strategy of expanding the interaction kernel V (instead of the scattering amplitude as before) and iterate the kernel to all orders in the Bethe-Salpeter equation. The leading order of the expansion yields the s-wave contribution, i.e. the vector interaction as in the tree level calculations [Kai95]. p-wave and higher order contribution have been calculated with coupled channel and

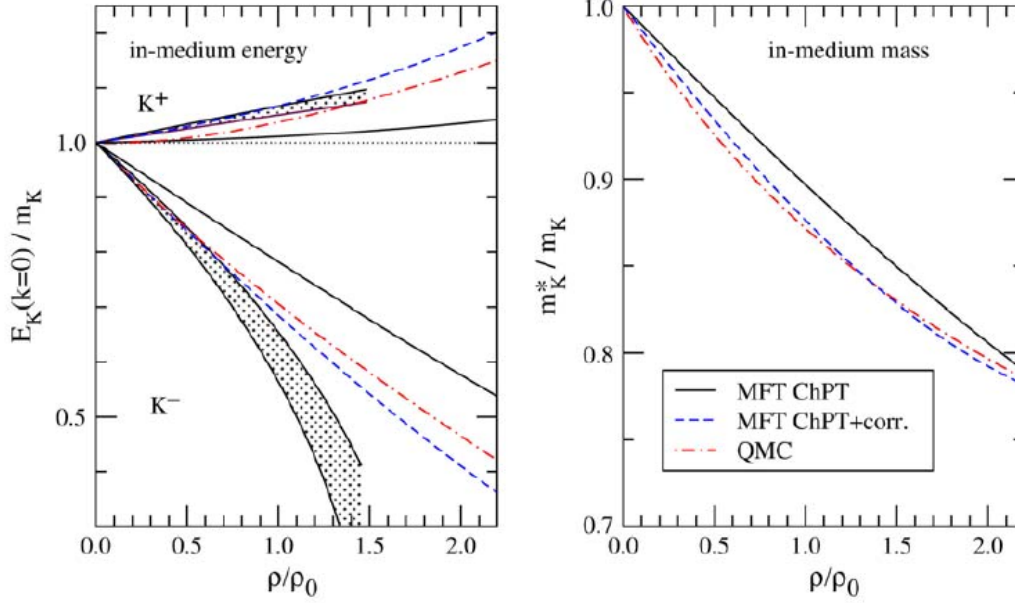


Figure 2.2: In - medium energy shift (left panel) and effective mass (right panel) of K^+ and K^- mesons as function of nuclear matter density as obtained by ChPT on the tree level (MFT ChPT), as well as the mean field calculations including higher order corrections (MFT ChPT+corr.) [Bro96 II] and quark meson coupling model (QMC) [Tsu98]. Results represented by the shaded bands are extracted from K^+N scattering and K^- atoms [Bat97]. The figure is taken from [Fuc06].

G - Matrix calculations by [Kol95, Lut02, Tol01, Tol02, Mul90].

The incorporated modifications by the medium are Pauli-blocking, dressing of the \bar{K} -propagator by in-medium self energy, dressing of the nucleon propagator due to interaction with other nucleons and dressing of the pion propagator due to Δ - and N -hole excitations. While nucleon dressing seems to contribute only minory, Pauli-blocking and pion dressing have been shown to influence the K^-N interaction significantly [Waa96, Kai97] and [Ram00, Tol01] respectively.

Results of various coupled channel calculations for K^- in-medium energy are shown in Fig. 2.3. All calculations suggest an attractive $\bar{K}N$ interaction, (more or less) linear in density, however of a different strength. Moreover, these results are comparable to the mean field calculations (Fig. 2.2) even though antikaons gain a considerable in-medium width and can not be seen as good quasi-particles.

In summary, the properties of kaons and antikaons are significantly modified by the medium. In nuclear matter kaons can be successfully treated as quasi particles and therefore, described in the framework of the mean field ChPT. The in-medium energy/mass is connected to the expectation value of the quark condensate by the GOR relation. Antikaons on the contrary, are strongly influenced by resonances in medium,

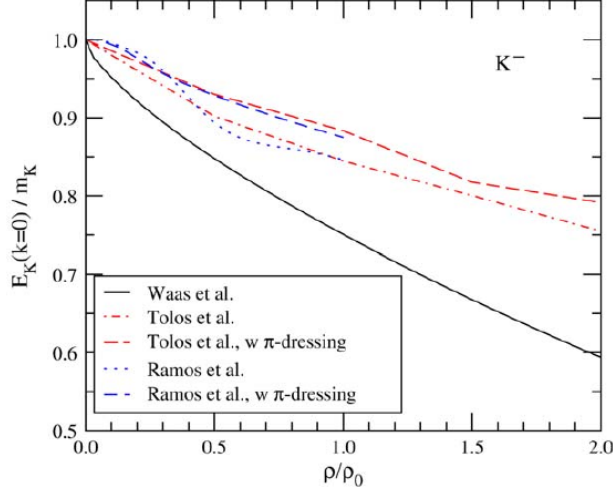


Figure 2.3: In-medium energy shift of K^- mesons as function of nuclear matter density as obtained in coupled channel calculations including different effects of the medium such as Pauli-blocking [Waa96], dressing of the kaon propagator [Ram00] and results with and without the dressing of the pion propagator [Ram00, Tol01]. The figure is taken from [Fuc06].

which makes the mean field approach highly questionable. The more sophisticated treatment for \bar{K} mesons are coupled channel calculations.

All theoretical predictions suggest a moderate repulsion of K by the nuclear medium and a strong attraction of \bar{K} , both increasing with nearly linear density dependence. The strength of the repulsion/attraction, however, is highly model dependent and especially for \bar{K} uncertain.

2.3 Light Vector Mesons in Nuclear Matter

Many hadronic models predict modification of the mass and width of vector mesons, such as ρ , ϕ and ω , in nuclear matter due to partial restoration of chiral symmetry.

Meson-nucleon optical potential can be written as:

$$U_{opt}(r) = V(r) + iW(r) \quad (2.15)$$

with meson mass shift:

$$V(r) = \Delta m(\rho_0) \cdot \frac{\rho(r)}{\rho_0}, \quad (2.16)$$

and meson absorption:

$$W(r) = -\Gamma_0/2 \cdot \frac{\rho(r)}{\rho_0}. \quad (2.17)$$

A possible mass shift can be experimentally investigated by measuring the line shape, spectral function or meson - nucleon bound states. The meson absorption manifests itself

in the so-called transparency ratio, i.e. the comparison of the production probability inside a nucleus (per nucleon) vs. on a free nucleon.

Of particular interest for this work is the ϕ meson. As a pure $\langle s\bar{s} \rangle$ state with no significant resonance overlap (unlike ρ or ω mesons) it is a convenient probe to study strangeness and anti-strangeness behaviour in dense nuclear matter.

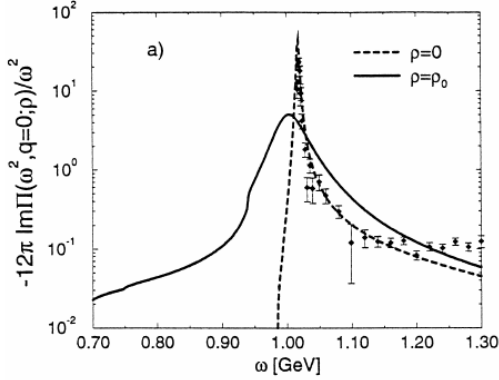


Figure 2.4: Spectral function of $\phi \rightarrow e^+e^-$ in vacuum (dashed line) and at normal nuclear matter density (solid curve) [Kli98]. The data points depict the ratio $\sigma(e^+e^- \rightarrow K^+K^-)/\sigma(e^+e^- \rightarrow \mu^+\mu^-)$ originating from [Iva81]. The normalization is chosen such that both curves are directly comparable.

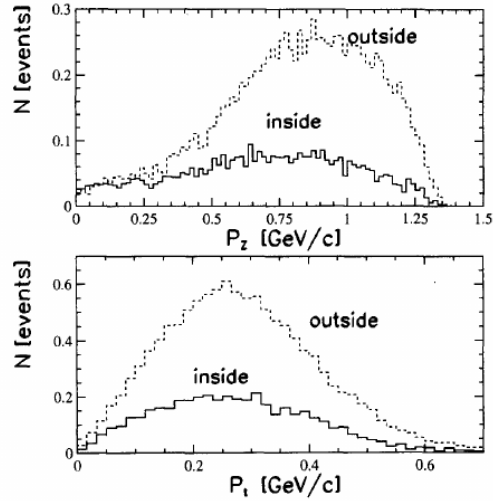


Figure 2.5: Calculated longitudinal (P_z) and transverse (P_t) momentum distribution for ϕ mesons produced in $\pi^- + Pb$ reactions decaying in- and outside the lead nucleus [Gol97].

In order to be sensitive to in-medium effects, the ϕ mesons need to decay in the hot and dense region of the collision. The vacuum width $\Gamma_\phi = 4.4$ MeV is too small, and therefore the lifetime too large to expect any medium modifications. However, calculations published in [Kli98] predict a significant increase of the ϕ width in medium already at normal nuclear matter density (Fig. 2.4), resulting in a lifetime $\tau_\phi < 5$ fm/c. Following this calculation, ϕ mesons with low momentum are expected to decay inside the ‘hot and dense’ medium. This expectation is supported by the results of intra-nuclear cascade calculations published in [Gol97]. Fig. 2.5 shows the momentum distribution in longitudinal and transverse direction of ϕ mesons produced in $\pi^- + Pb$ fixed target reactions with pion momentum of $p_\pi = 1.7$ GeV/c.³ The fractions of decays inside and outside the nucleus are disentangled. In the low momentum region almost as many ϕ mesons are expected to decay inside as outside the lead nucleus. Such experimental conditions can be reached in pion induced reactions in SIS 18 energy regime.

³ Even though this process is suppressed due to the OZI rule, the production is expected to be well detectable due to substantial $\omega\phi$ mixing.

2.4 Transport Calculations

Heavy-ion reactions are highly dynamic, multi-particle processes. No equilibration is reached in the intermediate stages of the reaction, i.e. the phase space distribution in the final state is influenced by the entire dynamical evolution of the system. To establish the connection between experimental observations and the underlying physics, the entire reaction dynamics have to be accounted for. This is possible in the framework of transport model calculations.

Transport calculations model the collision on a microscopic level. Production and scattering cross sections, as well as, various potentials are implemented⁴ to describe the evolution of the collision. Two fundamentally different models are commonly used in the SIS energy regime: The *Hadron-String-Dynamics* (HSD) - a one-body description and *Isospin Quantum Molecular Dynamics* (IQMD) - an n-body approach. In the following the basic ideas of these two models are summarised with a special focus on the description of kaon production and propagation in nuclear medium.

2.4.1 IQMD

IQMD transport model is a member of the QMD (*Quantum Molecular Dynamics*) transport family [Hart98, Aich91]. The basic principle of QMD models is a semi-classical simulation of a collision on an event by event basis. This approach allows to account for all particle correlations and is able to describe the formation of heavy fragments.

Particles are represented by a single-particle Wigner density with time-dependent position and momentum parameters and a fixed parameter describing the extension of the wave packet in phase space. The total Wigner density is the sum over all nucleons. The Hamiltonian is constructed from the total Wigner density and the in-medium nucleon-nucleon interaction. Particle transport is described by the Hamiltonian equations of motion. The potential for the in-medium nucleon-nucleon interaction has various contributions: Skyrme-type interaction, finite-range Yukawa potential, a momentum-dependent interaction, a symmetry interaction (difference between protons and neutrons) and the Coulomb interaction between charged particles. For details see [Hart98, Hart95].

The idea behind IQMD is to explicitly account for the isospin dependence of the cross sections and the nucleon potential. Later on in this work it is used to evaluate the flow pattern from heavy-ion collisions and to generate particle distribution for the Geant simulation of the FOPI detector.

Kaon - Nucleon Interaction

In IQMD both kaons and antikaons are treated as stable quasi-particles. The (anti)kaon-nucleon interaction is described by the Schrödinger-type optical potential:

$$U_{opt} = \omega(\mathbf{k}, \rho) - \sqrt{\mathbf{k}^2 + m^2}. \quad (2.18)$$

⁴In different models to a different extent, though.

The energy $\omega(\mathbf{k}, \rho)$ is calculated in the relativistic mean field picture [Scha01, Scha97]:

$$\omega(\mathbf{k}, \rho) = \sqrt{(\mathbf{k} - \Sigma_v)^2 + m^2 + m\Sigma_S} \pm \Sigma_v^0. \quad (2.19)$$

The scalar self energy Σ_S is related to the scalar density and the vector self energy (Σ_v^0 , Σ_v) to the baryon density. The sign of the vector term is positive for kaons and negative for antikaons. Compare Eq. 2.10.

An effective mass at density ρ , i.e. $\omega(\mathbf{k} = 0, \rho) = m_{K+}(\rho)$, can be approximated by a linear relation:

$$m_{K+}(\rho) = m_{K+}(\rho = 0) \left(1 + \alpha_{K+} \frac{\rho}{\rho_0} \right) \quad (2.20)$$

$$m_{K-}(\rho) = m_{K-}(\rho = 0) \left(1 + \alpha_{K-} \frac{\rho}{\rho_0} \right). \quad (2.21)$$

A factor α is applied to the scalar and vector potentials, to modify the value for the potential within this transport framework:

$$\omega_\alpha(\mathbf{k}, \rho) = \sqrt{(\mathbf{k} - \alpha\Sigma_v)^2 + m^2 + m\alpha\Sigma_S} \pm \alpha\Sigma_v^0. \quad (2.22)$$

Calculations without any KN -potential are done with $\alpha = 0$. The ‘normal’ IQMD potential is obtained with $\alpha = 1$. In Chapter 4 the experimental data is compared to ‘half’ the potential, i.e. $\alpha = 0.5$. The state-of-the-art of the evaluated transport models is captured in [Hart98].

2.4.2 HSD

In the HSD transport model [Cas97, Brat97, Cas99], the time evolution of a single particle phase space, under the influence of a mean field, is described by the *Boltzmann - Uehling - Uhlenbeck* transport equation. Nuclear matter is parametrised as a mean field in the Skyrme parametrisation. The solution of the BUU-equation is done numerically by a Monte-Carlo method using test particles.

Kaon - Nucleon Interaction

In HSD kaon-nucleon interaction is modelled similarly to the IQMD approach, i.e. the effective mass increases linearly with nuclear matter density according to Eq. 2.20. Different is the treatment of the elastic scattering with nucleons. Here HSD uses the effective mass, while IQMD calculates with on-shell particles.

The treatment of antikaons is significantly different. HSD employs a self-consistent coupled channel G-Matrix approach.

For \bar{K} a single-particle potential can be given in Brueckner-Hartree-Fock approach by:

$$U_{\bar{K}}(p_{\bar{K}}, E_{\bar{K}}^{qp}) = \sum_{N \leq F} \langle \bar{K}N | G_{\bar{K}N \rightarrow \bar{K}N} \left(\Omega = E_{\bar{K}}^{qp} + E_N^{qp} \right) | \bar{K}N \rangle, \quad (2.23)$$

with E_K^{qp} and E_N^{qp} antikaon and nucleon quasi particle energy. For definition and details see [Cas03].

\bar{K} self energy can be deduced from the optical potential:

$$\Sigma_{\bar{K}}(p_{\bar{K}}, \omega) = 2\sqrt{p_{\bar{K}}^2 + m_{\bar{K}}^2} U_{\bar{K}}(p_{\bar{K}}, \omega), \quad (2.24)$$

with $\omega = E_K^{qp}(p_{\bar{K}})$.

The HSD model take the effects of Pauli - blocking and pion self energy into account.

Chapter 3

The FOPI Experiment

The FOPI spectrometer is an azimuthally symmetric – 4π – apparatus, comprised of various sub-detectors in a HE-typical onion-like structure, constructed around a fixed target. The detector was operating till late 2011 at the ‘*Schwerionensynchrotron*’ (SIS-18) of the ‘*Gesellschaft für Schwerionenforschung*’ (GSI) in Darmstadt, Germany. In 2013 the experiment was dismantled.

The machine was designed to detect charged particles such as light mesons, protons, deuterons and heavier fragments. The identification of (short-lived) neutral particles is possible from their charged decay products. Azimuthal symmetry and large phase space coverage of the combined detector setup allow for an almost complete characterisation of an event.

The detector setup was upgraded in several stages. The last major upgrade, the so-called Phase III, prepared the machine for the highest possible beam energies of the SIS-18 accelerator by including a high resolution time-of-flight detector – the RPC. For the last physics run, the detector was upgraded with an additional vertex detector – the GEM-TPC. The data from this experiment is evaluated in the presented work, however the vertex detector is not included in the analysis. For the GEM-TPC analysis see [Böhmer Ph.D.].

The purpose of the following chapter is to provide a short overview of the relevant technical details and experimental conditions. The subset of used FOPI detectors is introduced by their composition, operation principle and limitations. The particle identification (PID) capability of various sub-detectors and overall PID strategy are explained. In this work data sets from two experiments, S325(e)¹ and S339², are analysed. Trigger conditions and relevant setup details of these experiments are summarised.

3.1 Setup of the FOPI Detector

Sub-detectors of the FOPI apparatus can be divided in two main groups:

The multiwire proportional chambers, ***Central Drift Chamber (CDC)*** and ***Helitron***, recording particle’s track and energy loss and the time-of-flight (ToF) detec-

¹ $^{58}\text{Ni} + ^{58}\text{Ni}$ reaction, with $E_{\text{beam}} = 1.91$ AGeV.

² $\pi^- + \text{C}$, $\pi^- + \text{Cu}$ and $\pi^- + \text{Pb}$ reactions, with $p_{\pi^-} = 1.7$ GeV/c.

tors, *Plastic Barrel (BAR)*, *Resistive Plate Counter (RPC)* and the *Plastic Wall (PLAWA)*, measuring the velocity of transpassing particles.

All sub-detector, with the exception of the plastic wall, are placed in a homogeneous magnetic field parallel to the beam axis. The nominal field strength of $B_Z = 0.6$ T is produced by the solenoidal, superconducting magnet operated with a current of $I = 720$ A [Rit95].

The full configuration of the FOPI detector (in Phase III) is depicted in Fig. 3.1.

Note: Helitron is not used in the current analysis.

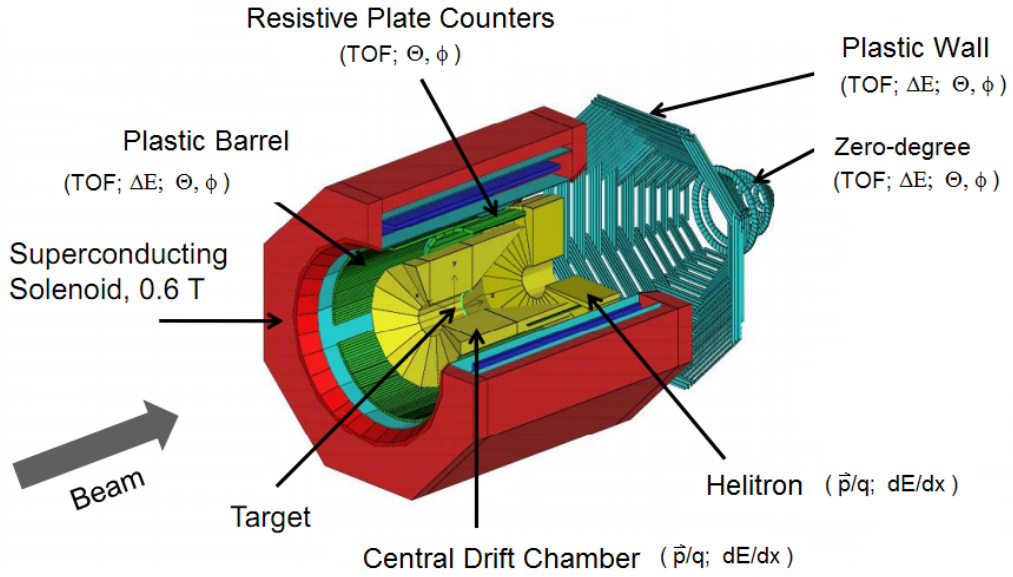


Figure 3.1: Configuration of the FOPI detector with information provided by individual sub-detectors.

The core of the FOPI detector is the central drift chamber:

CDC: The chamber volume is divided into 16 sectors in the azimuthal plane. The sectors are defined by a field cage, separating the sectors' active volume from the neighbouring one. Each sector contains a plane of 60 sense wires, measuring the signal. The electric field for the electron drift and multiplication is produced by 61 potential wires, located in the same plane as the sense wires. The wires are arranged in the alternating order in the x-y plane and align parallel to the beam axis.

Sectors of the CDC are tilted by 8° with respect to the target to distinguish real tracks from the mirrored ones³. The tilt ensures that only real tracks, extrapolated to the target, go through the vertex. The chamber is filled with a gas mixture of 88 % Ar, 10 % iso- C_4H_{10} and 2 % CH_4 . It is operated at atmospheric pressure.

³A priori the wire can not distinguish the signals coming from left or right. Therefore, the reconstruction algorithm sees two tracks - the real and the mirrored one.

The position resolution for minimum ionising particles (MIPs) in the azimuthal plane is $\sigma_{xy} \sim 300 \mu\text{m}$ [Sch91]. The longitudinal uncertainty is constrained by the charge division to the both ends of the wire. Only a low resolution of $\sigma_z \sim 5 - 7 \text{ cm}$ [Rit95] can be reached in the z -direction.

The energy loss and track information of the CDC is complemented by the time-of-flight measurements in the plastic barrel and the RPC ToF barrel. The two barrels surround the CDC (see Fig. 3.2) without significant overlap on their active areas.

BAR: The plastic barrel consists of 30 modules, each containing 6 scintillator bars ($150 \times 4 \times 3 \text{ cm}^3$). Photo-multiplier tubes are used to read out scintillator bars on both ends.

A time resolution of $\sigma_t \approx 200 - 300 \text{ ps}$ is reached. The corresponding position resolution is about $\sigma_z \approx 3 \text{ cm}$ [Rit95].

RPC: The RPC ToF-barrel is constructed from **M**ulti-**s**trip **M**ulti-**g**ap **R**esistive **P**late **C**ounters (MMRPC). Each counter consists of 10 glass plates (window glass) as resistive material and 8 gaps between them, defined by $220 \mu\text{m}$ fishing line. Five MMRPCs are summed up into a supermodule. In total 30 supermodules are arranged around the CDC with a geometrical coverage of 88.7 %.

MMRPC was shown to reach an outstanding time resolution of $\sigma_{MMRPC} \leq 65 \text{ ps}$ and the full-system time resolution of $\sigma_{ToF} \leq 88 \text{ ps}$ [Kis10].

In the polar angle range $\theta_{lab} = 7^\circ$ to $\theta_{lab} = 24^\circ$ an additional ToF detector – the PLAWA – records low transverse-momentum particles. This information is used for online triggering and later on, in the analysis, for centrality selection and reaction plane reconstruction.

PLAWA: The plastic wall consists of 512 plastic scintillator bars arranged in a concentric array with 8 sectors, 64 bars each. The scintillators are read out on both ends by photo-multipliers. The time resolution of $\sigma_t \sim 80 - 120 \text{ ps}$, translates into position resolution $\sigma_{xy} \sim 1.2 - 2 \text{ cm}$ [Gob93].

All sub-detectors require a time reference. The reference is provided by a signal in the start counter.

Start counter: The *plastic start counter* is a thin scintillator foil, tilted by 45° around the vertical axis. The foil was placed $\sim 2 \text{ m}$ upstream of the target. Light signal from ions passing through the foil can be detected by two photomultipliers placed perpendicular to the beam. To reject non-target events, two additional concentric scintillator-array (*veto detector*) were placed around the beam at $\sim 2 \text{ m}$ and $\sim 20 \text{ cm}$. In the S325e experiment, an additional start detector, a polycrystalline-chemical vapour deposit (*p-CVD diamond*), was used to comply with the RPC's high time resolution. The time resolution of the combined system was found to be $\sigma_t \leq 50 \text{ ps}$ [Kis10].

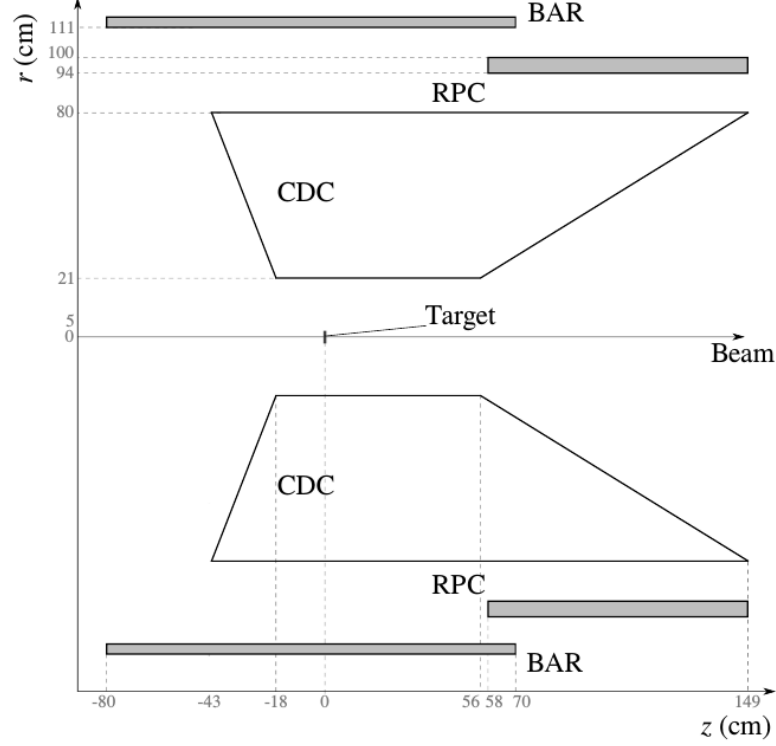


Figure 3.2: Schematic view of the FOPI detector in the y - z plane, showing only sub-detectors relevant for the following analysis. Note: Here the target is shifted by 20 cm upstream with respect to nominal target position in accordance with the setup of the S339 experiment. The figure (with slight changes) is taken from [Böhmer Ph.D.].

More information about the detector can be found in [Gob93] [Rit95] [Sik00].

3.2 Detector Acceptance

Detector acceptance is defined as the region of phase space which is covered by the active area of the detector. In the following analysis the particle identification is done with the CDC alone, CDC+RPC or CDC+BAR detector subsystems. The acceptance is limited by two geometrical restrictions of the setup:

Minimal transverse momentum: In the transverse plane the FOPI detector system covers nearly the full azimuthal angle range but all sub-detectors have a transverse distance to the beam axis (see Fig. 3.2). In the magnetic field a path of a charged particle is bent. The bending radius is proportional to particle's momentum. Only particles with sufficient transverse momentum can transpass the gap to a certain detector. To reach the CDC, a $p_t \geq 20$ MeV/ c is required. To reach the RPC/BAR detectors a particle has to move with $p_t \geq 100$ MeV/ c .

Polar angle: From Fig. 3.2 it is obvious that sub-detectors only have a limited extension in the beam direction. In Table 3.1 the longitudinal acceptance of the sub-detectors of interest is summarised for the different target positions. For the S325(e) experiment, the target was shifted by -40 cm⁴ with respect to the nominal target position. In the S339 beam time this shift was -20 cm. Such target displacement serve the enlargement of the phase space for the desired processes.

Target position	BAR	CDC	RPC
nominal	$132^\circ < \Theta_{lab} < 68^\circ$	$131^\circ < \Theta_{lab} < 33^\circ$	$67^\circ < \Theta_{lab} < 37^\circ$
-20 cm (S339)	$126^\circ < \Theta_{lab} < 60^\circ$	$123^\circ < \Theta_{lab} < 30^\circ$	$58^\circ < \Theta_{lab} < 33^\circ$
-40 cm (S325)	$119^\circ < \Theta_{lab} < 53^\circ$	$112^\circ < \Theta_{lab} < 27^\circ$	$50^\circ < \Theta_{lab} < 30^\circ$

Table 3.1: Geometrical acceptance of several sub-detectors in terms of the longitudinal angle Θ_{lab} . All values are rounded numbers.

3.3 Particle Identification (PID)

In the following section only the basic principle of the PID within the FOPI apparatus is discussed. The identification of the particles of interest is discussed later on in more detail.

When a charged particle moves through the gas volume of the CDC, it interacts with the atoms of the gas mixture and loses energy through the excitation or ionisation of the gas atoms. The mean energy loss per distance can be related to particle's velocity by the Bethe-Bloch formula:

$$-\frac{dE}{dx} \propto \frac{z^2}{\beta^2} \left[\ln \left(\frac{2m_e c^2 \gamma^2 \beta^2}{I} \right) - \beta^2 \right] , \quad (3.1)$$

where $\beta = v/c$ the velocity of incident particle; $\gamma^2 = 1/(1 - \beta^2)$
 z - particle's charge, I - the mean ionisation potential and $m_e c^2$ - the electron mass.

The CDC is placed in a magnetic field. The recorded trace of a charged particle is bent due to the deflection in the magnetic field. The radius of the track is related to particle's transverse momentum per unit charge as:

$$p_t/q(\text{GeV}/c) = 0.3 \cdot B \cdot R , \quad (3.2)$$

$$p = p_t / \sin \Theta , \quad (3.3)$$

with B is the magnetic field in Tesla and R is the radius of track's curvature in meters.

Correlating energy loss and momentum, particles of different mass become disentangled. Energy loss as a function of momentum per unit charge, as measured in the

⁴Negative shift is defined as upstream.

S325(e) experiment, is shown in the left panel of Fig. 3.3. In this representation particles with different mass arrange in separated branches allowing for particle identification. The separation is clear for particles such as pions and protons, however, the more rare particle – like kaons – are contaminated by their ‘neighbours’.

PID capability for kaons can be improved by combining the CDC analysis with the information from the ToF detectors: BAR and RPC. By measuring the time a particle takes to traverse the detector and the time the signal needs to reach the read-out at both ends of the strip, ToF detectors provide information about the hit position (Θ_{lab}, ϕ) and the velocity of a particle. Through the coordinates of the hit position, tracks from the CDC can be matched to tracks in the ToF barrels, yielding a simultaneous and independent measurement of momentum and velocity. The momentum-velocity correlation is shown in the right panel of Fig. 3.3. In the combined analysis the separation of kaons, especially for higher momenta, becomes significantly cleaner.

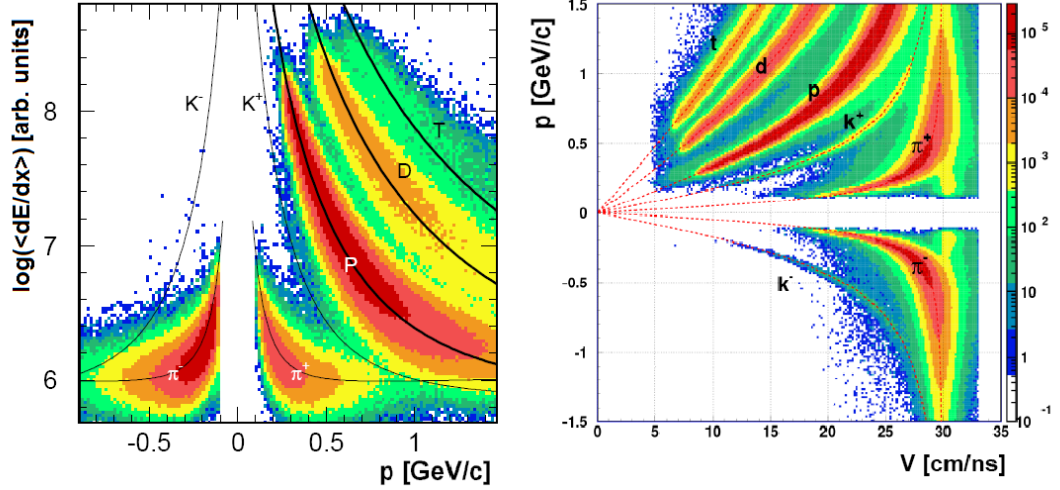


Figure 3.3: Left panel: Energy loss as a function of momentum per unit charge, measured in the CDC [Fin01]. Right panel: Momentum (CDC) - velocity (ToF) correlation [Kan10].

3.4 The S325 Experiment

The beam-time with the proposal name ‘S325’ was executed in two parts: The S325, a short experiment, performed in September 2007 ($\sim 1/5$ of the accumulated statistics) and the main part, S325e, performed in March 2008. S325 was the first experiment after the FOPI apparatus was upgraded with the RPC ToF detector and the p-CVD diamond start counter. In order to enlarge the geometrical acceptance and make the best use of the newly installed RPC, the target position was shifted by -40 cm, i.e. upstream, with respect to the nominal target position. Furthermore, to reduce the background events originating from the interaction of the beam ions with the target surrounding gas, the target was placed inside a helium bag.

The **beam**, used for S325, consisted of $^{58}\text{Ni}^{28+}$ ions at a kinetic energy of 1.91 AGeV⁵ with the average beam intensity of $I \sim 10^7$ ions per spill and 10 s spill length.

The **target material** was a thin foil ($d = 405\mu\text{m}$) of enriched (95 %) ^{58}Ni with an areal density of $\rho = 360 \text{ mg/cm}^2$.

The resulting interaction probability of the beam with the target can be calculated as follows:

$$p_{\text{reac}} = \rho \cdot d \cdot \frac{N_A}{A} \cdot \sigma_{\text{tot}}^{\text{geom}} \quad (3.4)$$

$$= \rho \cdot d \cdot \frac{N_A}{A} \cdot \left(\sqrt[3]{A_p} + \sqrt[3]{A_t} \right) \cdot 1.2 \text{ fm} , \quad (3.5)$$

where N_A is the Avogadro constant, A the atomic weight of the target material⁶, $\sigma_{\text{tot}}^{\text{geom}}$ the total geometrical cross section for a reaction between target and projectile nucleus and $A_p(A_t)$ number of projectile (target) nucleons.

For the given system the interaction probability is $p_{\text{reac}} \approx 1\%$.

The main goals of the S325 beam-time were the search for hypernuclei and the investigation of the in-medium behaviour of strange hadrons.

3.4.1 Trigger

Event rates of the order of 10 kHz can be reached in fix target experiments at SIS-18. To reduce the amount of data, which needs to be stored, and suppress the background, potentially interesting events are preselected by using an online trigger.

In FOPI, event classes (so-called ‘trigger bits’) are defined by imposing conditions on beam quality and require a signal in certain sub-detectors. Usually various triggers are active during a beam-time. In the S325(e) a dominant trigger required:

$$\text{PB} \ \& \ \text{PLA} > 4 \ \& \ (\text{RPC} > 0 \vee \text{BAR} > 0),$$

i.e. ‘proper beam’ (PB), at least 4 charged hits in the PLAWA and at least one hit in the RPC or BAR detector for a positive trigger decision. For the ‘proper beam’ condition, the beam particles need to generate a signal in the start detector and no signal in the veto counter. In addition pile-up events in the start counter and pre-protection in an 100 ns interval were active.

A *down-scale* can be introduced to enrich the data with certain type of events. In this scenario only a fraction (for technical reasons in powers of 2) of events is recorded by the data acquisition system (DAQ).

Knowing the experimental conditions, the triggered cross section $\sigma_{\text{trig.}}$ can be calculated as follows:

$$\frac{\sigma_{\text{trig.}}}{\sigma_{\text{tot}}^{\text{geom}}} = \frac{N_{\text{trig.}} \cdot f_{\text{non target}}}{N_{\text{proper beam}} \cdot d s_{\text{tot.}} \cdot d s_{\text{trig.}} \cdot p_{\text{reac}}} , \quad (3.6)$$

⁵GeV per nucleon.

⁶ $N_A = 6.022 \cdot 10^{23} \text{ mol}^{-1}$ and $A(\text{Ni}) = 58.69\text{u}$; $A(\text{C}) = 12.0107\text{u}$; $A(\text{Cu}) = 63.546\text{u}$; $A(\text{Pb}) = 207.2\text{u}$.

with

$$ds_{tot.} = \frac{N_{inh}}{N_{raw}} \quad \text{and} \quad ds_{trig.} = \frac{N_{acc}}{N_{inh}},$$

$N_{trig.}$: number of observed events for a given trigger per second,
$f_{non\ target}$: fraction of events with vertex outside the target,
$N_{proper\ beam}$: number of incoming ions per second,
$ds_{tot.}$: dead - time induced down - scale factor,
$ds_{trig.}$: hardware down - scale factor,
N_{inh}	: number of events outside dead - time of detector,
N_{raw}	: total number of events,
N_{acc}	: number of events accepted.

The initial number of accepted beam particles, N_{raw} , is reduced in two steps (see Fig. 3.4): by a dead time, required to write the data on tape and a possible downscale. The dead time is accounted for by the factor $ds_{tot.}$. The number of remaining events is referred to as ‘after inhibit’ - N_{inh} . If a downscale factor is applied, only every 2^n th event of the events after inhibit is accepted. The factor $ds_{trig.}$ includes it into the calculation and reduces the number of events to N_{acc} .

Note: there was no down scaling during the S325(e) runtime.

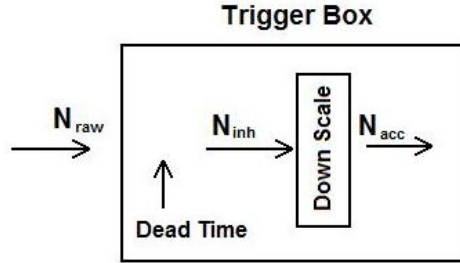


Figure 3.4: Sketch of the trigger system. For details see text.

The required quantities can be reconstructed from the data stored on data summary tapes (DST) and in the list mode data (LMD) files as follows:

$N_{trig.} \cdot f_{non\ target}$ - number of accepted events with a start signal (t_s) and a valid vertex position for a certain run with the desired trigger.

$N_{proper\ beam} \cdot ds_{tot.} \cdot ds_{trig.} = N_{acc}$ - scaler information, stored in LMD files.

For S325e the triggered centrality was found to be $\sim 60\%$ of the geometrical cross section, i.e.:

$$\sigma_{trig.} = 1530 \pm 90 \text{ mb.} \quad (3.7)$$

The corresponding impact parameter can be estimated in the sharp cut - off approximation: $b_{cut} \approx 7 \text{ fm}$.

The total geometric cross section is calculated as:

$$\sigma_{geom}(A) = \pi \cdot b_{max}^2 = \pi \cdot (2 \cdot r_A)^2 = \pi \cdot \left(2 \cdot r_0 \cdot \sqrt[3]{A}\right)^2, \quad (3.8)$$

$$\sigma_{geom}(\text{Ni}) = 2711 \text{ mb}. \quad (3.9)$$

with $r_0 = 1.2 \text{ fm}$ and $b_{max} = 9.3 \text{ fm}$.

Fig. 3.5 shows the results of Eq. 3.6 for each run of the S325 and S325e experiment. The triggers cross section is nearly constant throughout all runs. The few instabilities of the system are caused by a defocused beam. They amount to a negligible part of the statistics.

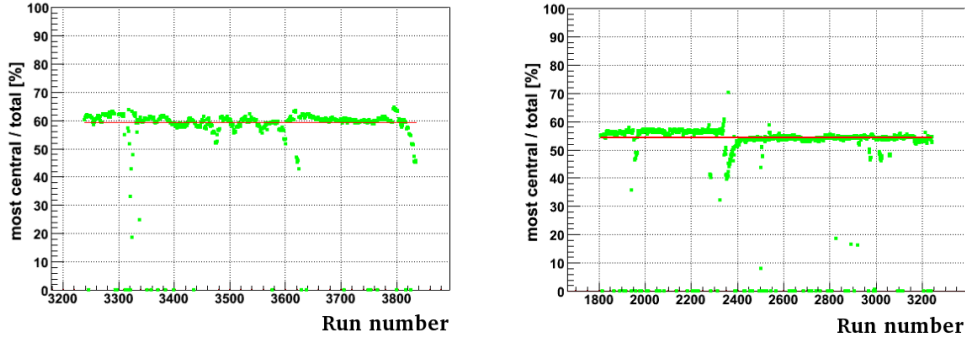


Figure 3.5: Triggered cross section as a function of the run number for the S325 (left panel) and S325e (right panel) experiment [KPia].

3.5 The S339 Experiment

The S339 experiment was performed in June 2011 and was the last FOPI experiment pursuing a physics program.

The measurements were made using a secondary pion beam, created with a primary $^{14}\text{N}^{7+}$ beam of $E_{beam} \sim 1.9 \text{ AGeV}$ on beryllium target. The produced pions had a beam momenta of $p_{\pi^-} = 1.7 \pm 0.03 \text{ GeV}/c$ and a beam intensity of $\sim 9 \cdot 10^3 \text{ pion/s}$.

Three different targets were used during this beam-time: carbon, copper and lead. Experimental conditions and the accumulated statistics for each target are summarised in Table 3.2. Note: The data from runs 3093-3166 is not analysed in this work.

Table 3.3 gives an overview of relevant target properties, the corresponding geometrical cross sections, calculated from Eq. 3.8, as well as the interaction probability for a given target, calculated using Eq. 3.4.

Detailed information on the targets can be found in Appendix E.

The goals of this beam-time were to measure the production and absorption of K_S^0 , K^+ mesons and Λ baryons in order to investigate their in-medium behaviour, and to study the production of the $\phi(1020)$ resonance in pion-induced reactions.

The in-medium properties of K mesons and the Λ baryons are addressed later in this

Run numbers	Target	Target pos.[cm]	Nr. of rec. evnt	Nr. of rec. tracks
3167-3293	C	-20	5 477 355	12 473 880
3594-3618	Cu	-20	2 557 994	6 167 072
3093-3166	Cu	-40	n.a.	n.a.
3346-3531	Pb	-20	5 579 509	12 992 921

Table 3.2: Technical characteristics of the S339 experiment, sorted by targets. The internal run identification - run number, shifted target position with respect to the nominal target position and the total number of events and tracks processed in the following analysis.

Target	d[mm]	$\rho \cdot d$ [g/cm ²]	σ_{tot}^{geom}	p_{reac} [%]
C	10	1.87	237.1	2.22
Cu	5	4.41	716.26	2.99
Pb	5	5.76	1588.14	2.66

Table 3.3: Physical properties of targets, used during the S339 runtime: d - thickness of the target in the beam direction; $\rho \cdot d$ - surface density of the target; σ_{tot}^{geom} - the total geometrical cross section [Eq. 3.8]; p_{reac} - beam - target interaction probability [Eq. 3.4].

work by comparing their production and dynamic behaviour in a heavy and light targets. The production of ϕ mesons is investigated by means of the so - called transparency ratio.

3.5.1 Trigger

A combination of different trigger patterns was employed during the S339 beam - time. The definitions of the individual trigger bits are summarised in Table reftab:tri. All triggers require a proper beam - ‘PB’ (i.e. signal in the start counter and no signal in the veto detector) and additionally a signal in one or several ToF detectors. Note that the triggers are not disjunct. Trigger bits T9, T14 and T15 have been downscaled during the data acquisition.

For a single run the triggered cross section is calculated according to Eq. 3.6. Fig. 3.6 shows the distribution of the cross section as a function of the run number for the employed trigger bits. Except for a few outliers, the triggered cross section remains constant through all runs for a particular target. The outliers are caused by a defocus beam or a complete deletion of a run. The values for σ_{trig} in Table reftab:tri are obtained by calculating the mean value and the standard deviation over all runs.

⁷For runs with run number > 3438 the downscale factor was changed to 4.

Trigger ID	Trigger condition	DS factor	C - Tar: σ_{trig} [mb]	Pb - Tar: σ_{trig} [mb]
T9	PB & PLA > 0	4 , 2 ⁷	85.91 ± 0.63	540.45 ± 2.23
T10	PB & PLA > 0 & RPC > 0	–	15.43 ± 0.17	100.23 ± 2.92
T11	PB & PLA > 0 & BAR > 0	–	16.19 ± 0.3	97.57 ± 2.52
T12	PB & RPC > 0 & BAR > 0	–	47.99 ± 0.28	393.01 ± 2.56
T13	PB & RPC > 2	–	54.46 ± 1.37	392.79 ± 10.58
T14	PB & RPC > 0	4	148.24 ± 3.1	1110.58 ± 14.59
T15	PB & BAR > 0	4	155.09 ± 1.32	1139.97 ± 1.05

Table 3.4: Trigger conditions as applied during the S339 runtime. See text for details. The DS factor reflects the downscale condition. σ_{trig} are the mean values \pm standard deviation over all runs. The outliers are excluded.

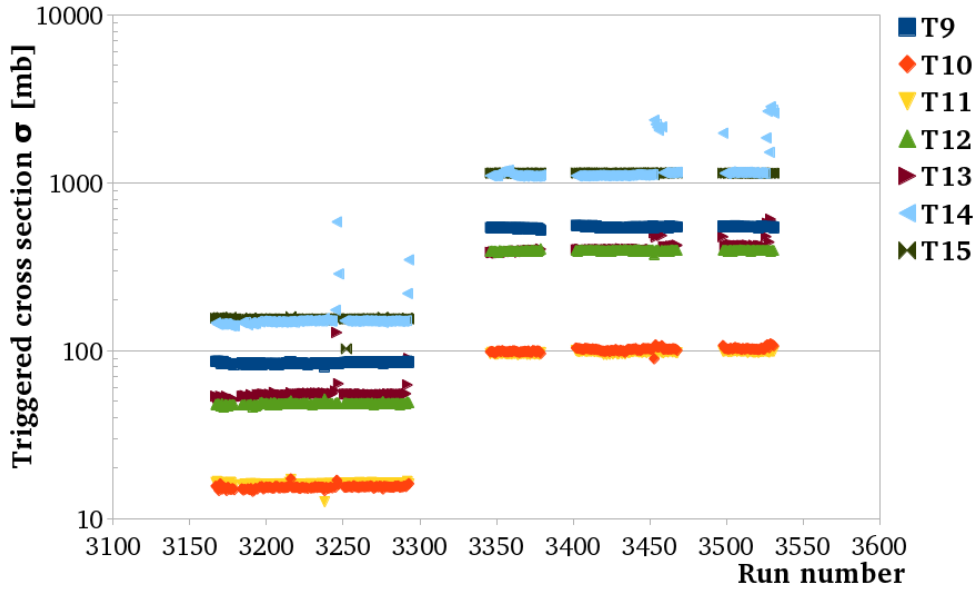


Figure 3.6: Triggered cross section as a function of the run number for the S339 experiment.

Chapter 4

The S325 Experiment

Experiment with the internal name ‘S325’ recorded $^{58}\text{Ni} + ^{58}\text{Ni}$ collisions at an incident beam energy of $E_{\text{beam}} = 1.91$ AGeV – the highest beam energy available at SIS-18. Technical details of the experiment can be found in Section 3.4.

During the collision a fireball of hot and dense nuclear matter is created. Temperature of about 100 MeV and net baryon densities of 2-3 times the normal nuclear matter density (ρ_0) are reached in the interior of the fireball in considered collisions [Fuc06, Hon98]. The aim of the following analysis is to investigate how this extreme environment influences the propagation of charged K mesons.

In collisions of free nucleons, kaons can be produced as follows:

$$NN \rightarrow K^+ \Lambda(\Sigma) N \quad E_{th} = 1.58 \text{ GeV} \quad \text{and} \quad (4.1)$$

$$NN \rightarrow K^+ K^- NN \quad E_{th} = 2.87 \text{ GeV}, \quad (4.2)$$

where E_{th} is the threshold energy for the reaction. In the discussed experiment, the beam energy was sufficiently high to produce K^+ mesons directly in the so-called ‘associative production’ channel Eq. 4.1. K^- mesons, on the contrary, can only be produced *sub-threshold*. In heavy-ion collisions, compared to elementary collisions, there are mechanisms that allow to accumulate the required energy. A positive contribution to the total available energy can be the Fermi-motion of the nucleons in the target and projectile nuclei. More commonly, however, the necessary energy is accumulated in multi-step processes. K^- mesons are produced either by exciting a nucleon resonance (e.g. Δ) first. The resonance acts as an energy deposit so that the total energy available for the subsequent collision with a nucleon is sufficiently large. Or by producing strangeness in form of a hyperon in the primary collision and then a K^- meson in a pion-hyperon reaction. Possible production channels are summarised in Table 4.1. The so-called strangeness exchange reaction: $\Lambda(\Sigma)\pi \rightarrow K^- N$ is energetically the most favourable channel and therefore the most common way to produce a K^- meson under given conditions. Unfortunate for the final state observations is the large cross section of the inverse reaction. Produced K^- mesons are likely to be reabsorbed again. On one hand the multi-step production ensures that K^- mesons originate from the dense phase of the collision. On the other hand, the production in strangeness exchange reactions is also possible close to the surface, in the low density phase. Consequently, the K^- mesons are sensitive to the full time evolution of the system.

An additional source of K^- mesons in the final state are strange particles with K^- in their decay chain. In the considered system, it is mainly the ϕ meson. A recent analysis by the FOPI collaboration, in agreement with another measurements, states that in this particular experiment 18 ± 3 % of K^- mesons in the final state originate from the decays of ϕ mesons [Pia16].

K^+					K^-				
NN	\rightarrow	NYK	NY π K	NY $\pi\pi$ K	NN($\Delta\Delta$)	\rightarrow	NNKK	NN π KK	NN $\pi\pi$ KK
N Δ	\rightarrow	NYK	NY π K	NY $\pi\pi$ K	N Δ	\rightarrow	NNKK	NN π KK	NN $\pi\pi$ KK
$\Delta\Delta$	\rightarrow	NYK	NY π K	NY $\pi\pi$ K	π N(Δ)	\rightarrow	NKK	N π KK	
π N	\rightarrow	YK	Y π K		π Y	\rightarrow	NK		
$\pi\Delta$	\rightarrow	YK	Y π K		NY	\rightarrow	NNK		
					$\pi\pi$	\rightarrow	KK		

Table 4.1: Possible production channels for K^+ and K^- mesons in heavy-ion collisions at intermediate energies. The symbol ‘Y’ denotes a hyperon, i.e. Λ or Σ baryon. The bold notation, ‘**K**’, stands for an antikaon.

This chapter is organised as follows: First the experimental reconstruction and the quality of the K^+ and K^- signal are discussed. Possible in-medium effects are studied by the evaluation of the so-called ‘flow’ – the asymmetries in the azimuthal emission pattern. The method and necessary corrections are introduced. Flow patterns are studied systematically within the comparison to HSD and IQMD transport calculations. Contributions from different potentials, as well as the momentum and centrality dependence of the in-plane and out-of-plane flow components are examined. The results of the present work are compared to similar measurements from the literature.

4.1 Reconstruction of Charged Kaons

The main strategy of particle identification within FOPI is summarised in Section 3.3. The information provided by the CDC is sufficient to reconstruct abundant particles, like pions and protons. For charged kaons, especially towards the upper momentum limit, it is beneficial to evaluate the combined information of the CDC and the ToF-Barrels, RPC and BAR.

The track recorded in the CDC is extrapolated to the vertex and to the RPC/BAR system. Two topological criteria select tracks which originate from the primary vertex: $d0$ is the transverse distance between the track and the vertex and $z0$ is the intercept of the projected trajectory with the beam axis. For the combined analysis the tracks are additionally extrapolated to the RPC/BAR and matching criteria are imposed to associate tracks in both sub-detectors. Whether the extrapolation and the ToF signal match is decided in the transverse plane by restrictions on the azimuthal angle $d\phi = \phi_{ToF} - \phi_{CDC}$ and along the beam direction by the hit position $dz = z_{ToF} - z_{CDC}$.

All four of these quantities exhibit a Gaussian-like distribution in the data. The final track selection is done by rejecting tracks with $d0$, $z0$, $d\phi$ and dz values larger than

$2 \times \text{r.m.s.}^1$ of the corresponding distribution. This particular choice of the tolerance window is motivated by the analysis summarised in [VZDTh] in order to maximise the significance of the kaon² signal.

For successfully matched tracks a second mass classification (ToF mass) is possible by correlating the independent measurements of the momentum from the CDC and the velocity in the ToF system. An example of a ToF mass spectrum, here obtained with the RPC, is shown in Fig. 4.1.

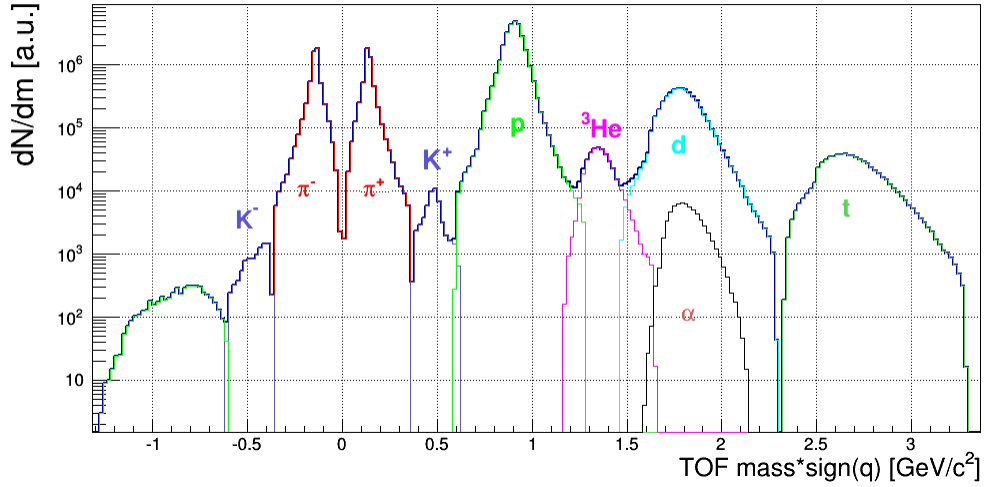


Figure 4.1: Mass distribution of charged particles, reconstructed in the time-of-flight detector sub-system, sorted by charge. Note that wide preselection mass-windows has been applied around the nominal particles' mass.

An excess around the nominal K^+ meson mass is clearly visible, the K^- signal is overshadowed by the background. The background is dominated by fast pions and can be significantly reduced by imposing an upper momentum limit.

In the following analysis only the sub-set of events is evaluated, namely those containing a kaon candidate. A kaon candidate is defined by an entry within a relatively large window around the nominal kaon mass. The strategy for the final selection of kaon candidates is depicted in Fig. 4.2 for K^+ mesons and Fig. 4.3 for K^- mesons. The momentum-velocity correlation (right panel respectively) reveals the kaon identification capabilities in the present data set. While the separation of K^+ candidates from protons and fast pions is distinct up to a relatively high momentum of $p_{max} \sim 1.2 \text{ GeV}/c$, a clear discrimination of K^- mesons is possible only for $p_{lab} < 1.0 \text{ GeV}/c$. Considering only particles which underlie the momentum limit, the two-dimensional mass correlations in the left panels are obtained. The 'CDC mass' is reconstructed from the energy loss-momentum correlation, both measured in the CDC sub-detector. The 'RPC mass' is obtained from the momentum-velocity correlation as describes above.

¹r.m.s. stands for the Root Mean Square. Since all of the above distributions are Gaussian-like, the r.m.s. is comparable to the standard deviation of the Gaussian fit to the the same distribution.

²Here and in the following the term 'kaon' is used synonymously for K^+ and K^- mesons.

Due to the different resolution in the RPC and BAR (see Chapter 3) the analysis is performed separately for both sub-detectors. Fig. 4.2 and Fig. 4.3 show only the results of the RPC analysis. Corresponding figures from the BAR analysis look similar, but with a smaller separation power and more contamination by the background. The obtained values and limitations are summarised in Table 4.2.

In order to reject as much background as possible, the kaon candidates for the flow analysis are selected by the ellipsoidally shaped cut in the two-dimensional mass correlation histogram (red ellipse in the left panels). To estimate the strength of the signal and the contribution from the background, the CDC mass is projected to the ordinate (panel in the middle). The peak around the nominal kaon mass is fitted with a Gaussian+Exponential function (not shown in the figures). The background is estimated by the exponential function with the parameters obtained from the fit. The signal ($S = N_K$) is calculated as the integral over the fitted Gaussian function in the mass limit indicated by the vertical lines (see Fig. 4.2 and Fig. 4.3) with the background (B), i.e. the integral over the fitted exponential function, subtracted. The obtained values are collected in Table 4.2.

To investigate the background fraction and optimise its description, K^- candidates are investigated differentially in small momentum intervals within the RPC sub-detector. See Fig. 4.4 and Fig. 4.5. At low momentum the kaons are clearly distinguished from other particles. With increasing momentum the background fraction rises, probably due to fast pions. Up to $p_{lab} = 0.85$ GeV/ c the background is well described by an exponential function. At the highest evaluated momentum of $0.95 < p_{lab} < 1.00$ GeV/ c a clear peak with as many kaons as background, i.e. $S/B \sim 1$ is observed. No excess over the pion tail around the nominal kaon mass is detected for $p_{lab} > 1.00$ GeV/ c , which marks the momentum limitation for K^- identification. Note: The ' S/B ' in Table 4.2 is an integrated value over all momentum bins, i.e. $0 < p_{lab} < 1$ GeV/ c .

The phase space distribution of final kaon candidates, depicted in Fig. 4.6, covers a wide range including the target rapidity $y_0 = -1$ and the mid-rapidity $y_0 = 0$ ³. The acceptance is limited by the geometry of the apparatus, i.e. the lower momentum limit, here $p_t/m > 0.3$ and spatial coverage along the beam direction⁴ (solid lines). An additional limitation, as discussed above, is the maximal momentum (dashed lines) denoting the highest possible momentum for unambiguous kaon identification.

³For the definition of kinematic variables see Appendix D.

⁴For details see the discussion in Chapter 3.

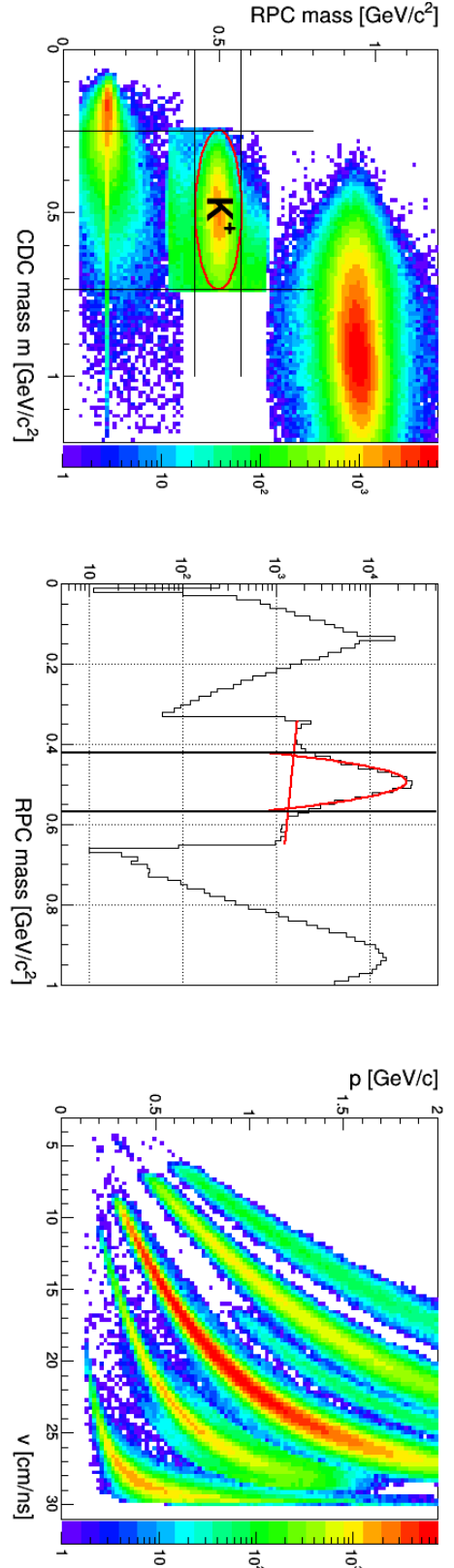


Figure 4.2: Correlated information of CDC and RPC sub-detectors, used for the selection of K^+ candidates: Two dimensional mass correlation (left panel), mass distribution in the RPC sub-detector (middle) and the momentum-velocity correlation (right panel). See text for details.

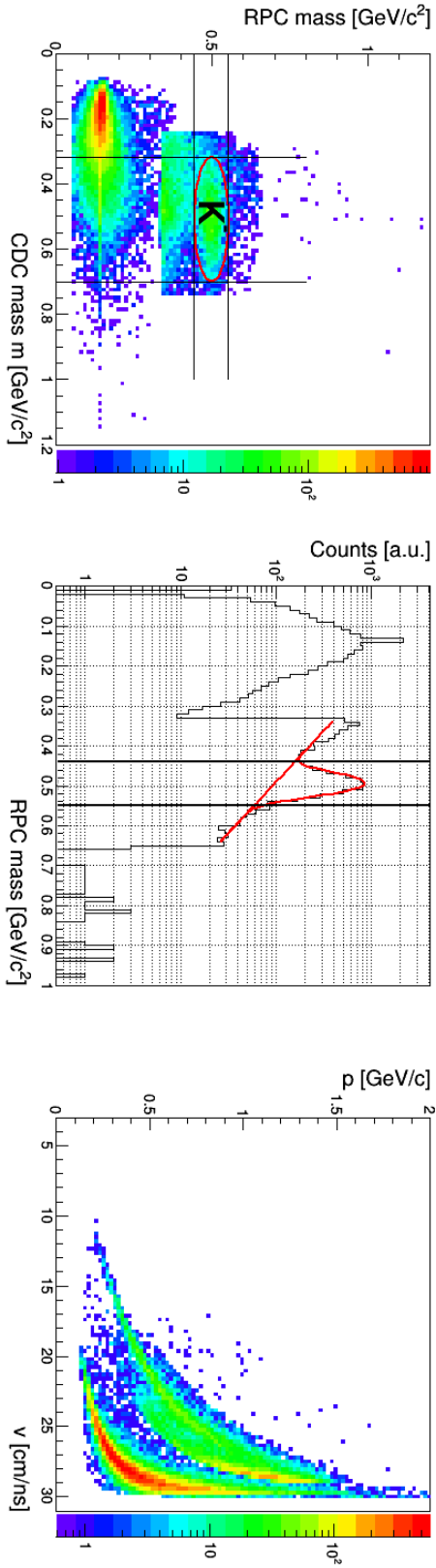


Figure 4.3: Diagrams for K^- candidat selection, analogue to Fig. 4.2.

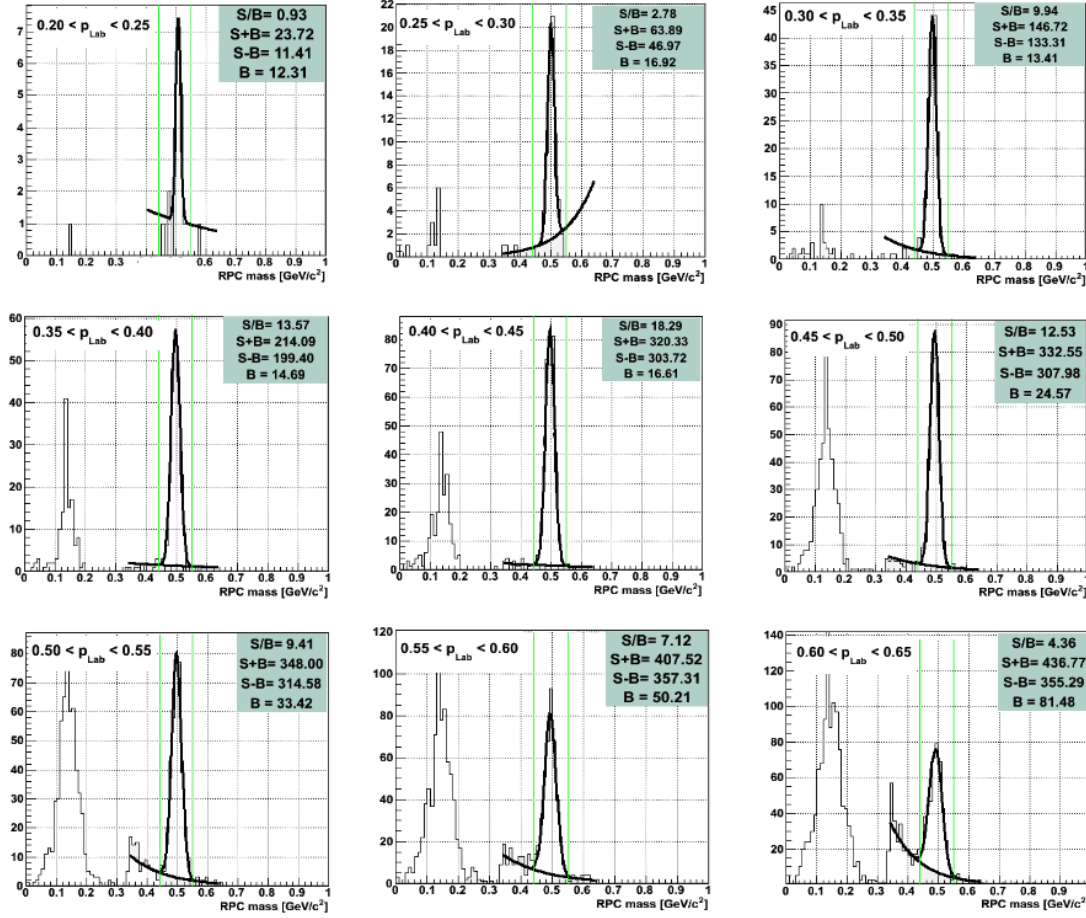


Figure 4.4: Mass distribution of negatively charged particles, obtained in the RPC sub-detector in different momentum bins. The quantity ‘S+B’ is defined as the integral of the mass histogram between the green lines. The background contribution ‘B’ is determined by the integral under the exponential function. Only events containing a $K^{+/-}$ candidate are evaluated.

		K^+	K^-
BAR	p_{max}	0.55 GeV/c	0.45 GeV/c
	S/B	~ 9	~ 7.4
	N_K	40966	645
RPC	p_{max}	1 GeV/c	1 GeV/c
	S/B	~ 15.4	~ 7.7
	N_K	142027	3792

Table 4.2: Properties of identified K mesons. p_{max} : maximal momentum for kaon identification in the listed sub-detector; S/B : signal to background ratio evaluated from the mass distribution; N_K : Number of identified kaon-candidates (corresponding background is subtracted.)

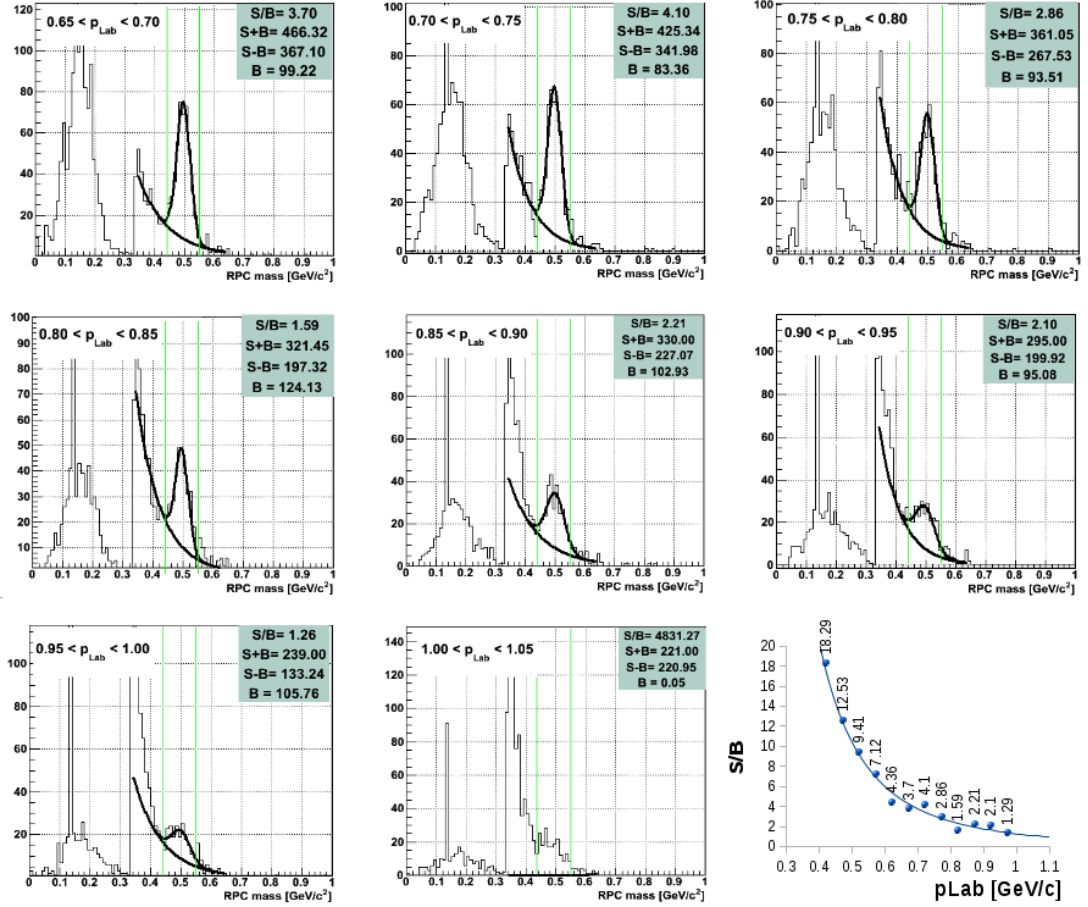


Figure 4.5: Continuation of Fig. 4.4. Lower right panel: Signal-to-background ratio obtained in the depicted momentum bins.

4.1.1 Finite Lifetime Correction

The lifetime of a charged kaon is $\tau_{K^\pm} = 12.38$ ns and its corresponding decay length is $c\tau = 3.714$ m [PDG]. Consequently there is a finite probability that a fraction of produced kaons decay before reaching the detector system. To account for the decay loss, the number of reconstructed kaons is weighted with the inverse decay probability $P(x)^{-1}$. $P(x)$ can be calculated from the momentum, p , of the considered particle as follows:

If $N(0)$ is the initial number of kaons, then after a time t the number of remaining kaons is given by

$$N(t) = N(0) \cdot \exp(-t/\tau).$$

The decay probability, therefore, is:

$$P(x) = \frac{N(t)}{N(0)} = \exp\left(-\frac{x}{\beta\gamma c\tau_0}\right) = \exp\left(-\frac{x \cdot m}{p \cdot \tau_0}\right).$$

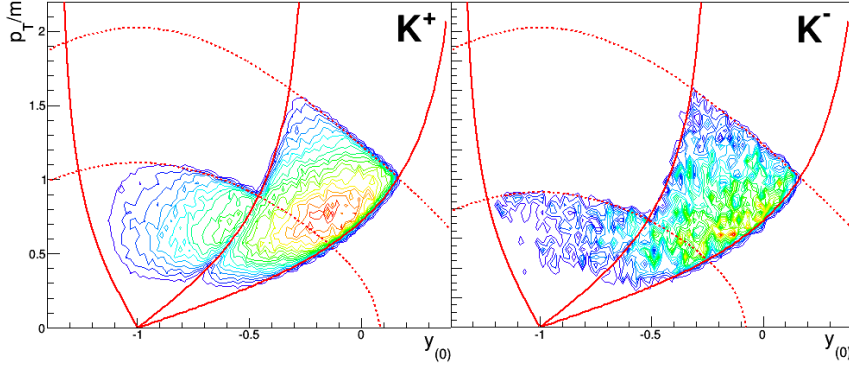


Figure 4.6: Phase space distribution of K^+ (left panel) and K^- (right panel) mesons. Solid curves show the geometrical restriction of the RPC and BAR sub-detectors, i.e. $\Theta_{lab} = 33^\circ, 53^\circ, 108^\circ$. Dashed curves depict the upper momentum limit in the corresponding sub-detectors: $p_{max} = 0.55$ & 1.0 GeV/c for K^+ mesons (left) and $p_{max} = 0.45$ & 1.0 GeV/c for K^- mesons (right). Normalised transverse momentum p_t/m and rapidity y_0 are defined in the Appendix D.

The following relations were used:

$$t = x/\beta \cdot c; \quad \tau = \gamma\tau_0; \quad \beta\gamma c = p/m$$

where m is the mass of the particle and x is the covered distance.

The path of a particle in the FOPI detector is a helix, i.e. circular in the transverse direction and linear in the beam direction.

The decay probability calculate from the total momentum along the full flight path is equivalent to the probability determined from the transverse momentum along the transverse flight path. In order to simplify the calculation, the decay probability is estimated from the transverse component. The length of the flight path is parametrised as

$$x = 2R \cdot \arcsin\left(\frac{L}{2R}\right),$$

where R is the radius of the circular path due to the deflection in the magnetic field and L is the transverse distance to the RPC (BAR) sub-detector. This correction is applied as a weighting factor to all histograms evaluating the ‘flow’ of charged kaons.

4.2 Asymmetries in the Azimuthal Emission Pattern

4.2.1 Fourier Expansion of the Azimuthal Particle Distribution

The collective motion of particles can be studied by investigating the anisotropies in their azimuthal emission. The asymmetries are qualified by the Fourier analysis of the

azimuthal distribution as proposed by [VolZha96]:

$$\frac{dN}{d\varphi} = \frac{1}{2\pi} \left(1 + 2 \sum_{n \geq 1} v_n \cos n\varphi \right), \quad (4.3)$$

with the Fourier coefficients:

$$v_n = \langle \cos n\varphi \rangle \quad n = 1, 2, \dots$$

where φ is the azimuthal angle of the particle with respect to the so-called reaction plane. Chevrons denote the average over a kinematic range.

Relevant for the present analysis are the first and the second Fourier coefficients. The first harmonic coefficient, v_1 , is given by:

$$v_1 = \left\langle \frac{p_x}{p_t} \right\rangle = \langle \cos(\varphi) \rangle.$$

It reflects the asymmetries in the reaction plane and is, therefore, referred to as ‘*directed*’ or ‘*in-plane flow*’.

The second coefficient, v_2 , is given by:

$$v_2 = \left\langle \frac{p_x^2 - p_y^2}{p_t^2} \right\rangle = \langle \cos(2 \cdot \varphi) \rangle.$$

It quantifies the anisotropies in both transverse directions, i.e. in the plane of the reaction and perpendicular to it. It is commonly referred to as ‘*elliptic flow*’.

Given a phase space distribution in terms of the transverse momentum, p_t , and normalised rapidity, y_0 , for a class of events with a certain centrality selection Δmul , a Fourier coefficient is calculated as the average over a given phase space cell (p_t, y_0) , i.e.:

$$\langle v_n(p_t, y_0) \rangle \propto \iiint \cos n\varphi \, dp_t \, dmul \, dy_0$$

The flow observables can be studied in a triply differential way by dividing the data sample into different centrality classes, and evaluating the coefficients as a function of transverse momentum and rapidity in each centrality class. The advantage of this representation is that it allows to study the flow dynamics in detail, the disadvantage – it requires a high statistics data sample to avoid large statistical fluctuations of the measured values. For particles with limited statistic the so-called *integrated flow* is evaluated. The calculated coefficients are averaged over the full transverse momentum range, instead of an interval, and analysed for different rapidity intervals and possibly with different centrality selection. The disadvantage of this representation is its lack of sensitivity to a possible momentum dependence of the flow observables and phase space limitations of the detector.

The azimuthal angle, φ , can be reconstructed from the experimentally measured azimuthal angle, ϕ , by taking into account the reaction plane. The reaction plane is

spanned by the z-direction, defined along the beam, and the impact parameter⁵ \vec{b} . If the relative orientation of the reaction plane is ϕ_R , then $\varphi = \phi - \phi_R$. The reconstruction of the reaction plane, its properties and necessary corrections are described in the following section.

4.2.2 Reaction Plane Reconstruction

The experimentally measured azimuthal angle, ϕ , is recorded with respect to the plane spanned by the direction of the beam and the impact parameter of the reaction, the so-called *reaction plane*. While the beam direction is well defined, the impact parameter is experimentally not accessible. Nevertheless there is a commonly used method, proposed by Danielewicz and Odyniec [DanOd85], to reconstruct the reaction plane event-wise from the distribution of the measured transverse momenta. The angle between the x-axis (in laboratory frame) and the direction of the impact parameter, ϕ_R , is determined by the orientation of the vector ‘ \vec{Q} ’. The \vec{Q} -vector is derived from the weighted sum of the transverse momenta of all particles in the event:

$$\vec{Q} = \begin{pmatrix} Q \cos \phi_R \\ Q \sin \phi_R \end{pmatrix} = \sum_{i=1}^N w_i \cdot \vec{p}_{t,i} \quad .$$

To avoid autocorrelations the particle of interest is excluded from the calculation. The weighting factor, w_i , is defined as:

$$w_i = \begin{cases} +1 & \text{for } y_0 > \Delta Y \\ 0 & \text{for } -\Delta Y < y_0 < \Delta Y \\ -1 & \text{for } y_0 < -\Delta Y \end{cases} \quad (4.4)$$

The particles from the mid-rapidity region ($y_0 = 0$) are not included in the calculation, because they do not carry information about the reaction plane but contribute to disturbing fluctuations.

The choice of the ΔY interval was investigated in [VZDTh] with the motivation of optimising the resolution of the reaction plane. The best results were obtained for $\Delta Y = 0.3$, therefore it is the value used for the reaction plane reconstruction in the following analysis.

For the analysis in this work the reaction plane is reconstructed from protons, deuterons and heavier fragments, measured in the CDC and all charged particles in the PLAWA sub-detectors⁶. Pions and kaons are not included, as they are produced during the collision and, therefore, do not carry the information about the initial plane of the reaction. In the Plastic wall, however, the distinction is can not be made without including the Helitron sub-detector.

⁵The impact parameter is defined as the perpendicular distance between the centres of the colliding nuclei.

⁶Internal classification: ‘RP1’.

4.2.3 Reaction Plane Resolution: Ollitrault Corrections

The reaction plane reconstruction method, as described above, requires a high (in the ideal case, infinite) number of particles in the event, the so-called *multiplicity*, to recreate the reaction plane accurately. The finite multiplicity of a physical event causes a certain imprecision in the reconstructed angles. A more realistic estimate of the reaction plane can be obtained by applying additionally a correction proposed by J.Y. Ollitrault [Oll97].

Assume that the reconstructed and the real reaction plane deviate by $\Delta\phi$. Parametrising the inclination of the particle's trajectory with respect to the reconstructed reaction plane as φ ⁷ and with respect to the real reaction plane as $\tilde{\phi}$, these quantities are related by: $\varphi = \tilde{\phi} - \Delta\phi$. Consequently, the Fourier coefficients (for independently measured ϕ and $\Delta\phi$) need to be corrected in the following way:

$$\langle \cos n\varphi \rangle = \langle \cos n\tilde{\phi} \rangle \langle \cos n\Delta\phi \rangle \quad (4.5)$$

$$\Rightarrow \text{the corrected } v_n = \langle \cos n\tilde{\phi} \rangle = \langle \cos n\varphi \rangle / \langle \cos n\Delta\phi \rangle \quad (4.6)$$

The correction factor $\langle \cos n\Delta\phi \rangle$ can be determined on event - by - event basis by dividing the event into two random sub - events with each half the multiplicity of the event and reconstructing the reaction plane separately for each of them. The difference of the obtained values $\Delta\phi_R = \phi_1 - \phi_2$ is used to calculate the dimensionless parameter χ from the relation:

$$\langle \cos \Delta\phi_R \rangle = \frac{\pi}{8} \chi^2 e^{-\chi^2/2} \left[I_0 \left(\frac{\chi^2}{4} \right) + I_1 \left(\frac{\chi^2}{4} \right) \right]^2.$$

I_n denote the modified Bessel functions.

Once the parameter χ is known, the correction factor for the n^{th} harmonic can be obtained from:

$$\langle n \cos \Delta\phi \rangle = \frac{\sqrt{\pi}}{2} \chi e^{-\chi^2/2} \left[I_{\frac{n-1}{2}} \left(\frac{\chi^2}{2} \right) + I_{\frac{n+1}{2}} \left(\frac{\chi^2}{2} \right) \right]. \quad (4.7)$$

The flow observables v_1 and v_2 in the following analysis are calculated as:

$$v_1 = \langle \cos(\phi - \phi_R) \rangle / \langle \cos \Delta\phi \rangle, \quad (4.8)$$

$$v_2 = \langle \cos 2(\phi - \phi_R) \rangle / \langle \cos 2\Delta\phi \rangle, \quad (4.9)$$

with ϕ : measured azimuthal angle,
 ϕ_R : estimated reaction plane by the method in Section 4.2.2,
 $\langle \cos n\Delta\phi \rangle$: Ollitrault correction.

The obvious consequence of the discussion above is that the magnitude of the Ollitrault correction depends on the multiplicity of the event. In the experiment, the event's

⁷ $\varphi = \phi - \phi_R$ in the previous notation.

multiplicity is closely related to the centrality of the underlying collision, as will be discussed in detail in Section 4.3. Therefore, the Ollitrault correction values are evaluated for each centrality class separately.

Fig. 4.7 shows the used correction factors for v_1 (left panel) and v_2 (right panel) as a function of the multiplicity of baryons (for definitions see Section 4.3).

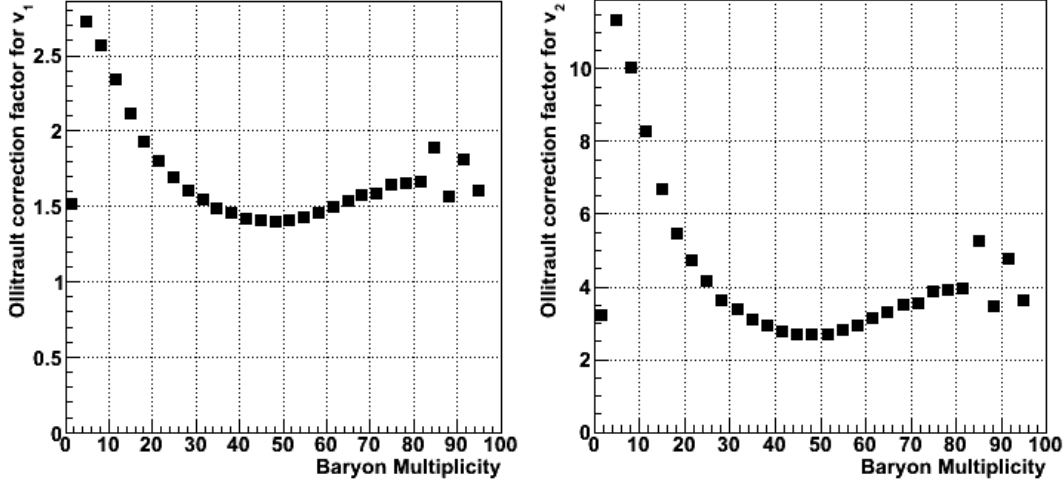


Figure 4.7: Correction factors for the first (left panel) and the second (right panel) Fourier coefficient as the function of event's multiplicity. The values are obtained by the Ollitrault method with Eq. 4.7.

4.2.4 Anisotropies of the Reaction Plane Distribution

A priori, the orientation of the reconstructed reaction plane is expected to be isotropic. In the experimental reality, however, a non-uniform distribution is usually observed. Dead channels of the detector, uncertainties of the calibration or misalignment of the detector components are discussed as possible reasons.

The anisotropic behaviour can be qualified with the procedure described in [Bare97 a, Bare97 b]. The initial, non-flat distribution of the reaction plane angle, ψ_1 , is fitted by the Fourier series and shifted on an event-by-event basis according to:

$$\psi'_1 = \psi_1 + \sum_{n=1}^{n_{max}} \frac{2}{n} (-\langle \sin(n\psi_1) \rangle \cos(n\psi_1) + \langle \cos(n\psi_1) \rangle \sin(n\psi_1)) . \quad (4.10)$$

The obtained distribution of ψ'_1 is isotropic.

The influence of the described flattening procedure on the first harmonic coefficient, v_1 of K^+ mesons was studied in [Kan10]. The observed fluctuations of the reaction plane angle are modest, due to azimuthally symmetric performance of the FOPI detector. The impact on the flow pattern was found to be negligibly small on the scale of statistic uncertainties⁸. Therefore, this correction is not implemented in the following analysis.

⁸Here the largest possible kaon sample was evaluated, i.e. the statistic uncertainties have the smallest

4.2.5 Systematic Errors

In the center of mass of a symmetric colliding system the value of the first Fourier coefficient $v_1 = \langle p_x/p_t \rangle$ is by definition equal to zero as a consequence of the fundamental momentum conservation. In the current experimental data, in consonance with other FOPI data, a deviation from zero is observed. The deviation was systematically investigated in different FOPI data sets and found to depend on the particle species, the centrality of the reaction and the system size. Simulations of the apparatus in the GEANT environment could reproduce certain properties, but not the extent of the deviation. In the considered colliding system, Ni+Ni at 1.9 AGeV, for the reaction plane reconstructed in the largest available polar angle range (see the discussion in Section 4.2.2) the deviation was found to be independent of transverse momentum. Details of this analysis can be found in [VZDTh].

To account for this effect in the current analysis a systematic error is introduced. The magnitude of the uncertainty, σ_{Sys} , reflects the deviation of the first Fourier coefficient from zero at mid-rapidity: $\sigma_{Sys} = v_1(y_0 = 0)$.

4.3 Centrality Selection

The centrality of an nucleus-nucleus collision is defined by the overlap of the colliding nuclei, i.e. the magnitude of the impact parameter. Experimentally, the centrality is also related to the multiplicity of reaction products. In central collision with a large overlap region the number of nucleon-nucleon collisions is large and, therefore, the amount of tracks in the detector is likely to be large. Vice versa a small number of tracks indicate low number of participant and therefore the peripheral character of the reaction.

In the presented analysis the centrality selection is done by the means of the ‘*baryon multiplicity*’. In this particular case, the baryon multiplicity is defined as the number of baryons (protons, deuterons, tritons, ^3He , α and rarely heavier fragments) measured in the CDC and the number of charged particles⁹ in the Plastic wall. The obtained multiplicity distribution is shown in the panel (b) of Fig. 4.8 as the blue histogram. The distribution is normalised to the total experimental cross section, as calculated in Section 3.4, i.e. $\sigma_{exp} = 1530 \pm 90$ mb.

The baryon multiplicity can be simulated in transport calculations by counting the ‘baryons’ in the geometrical acceptance of the considered sub-detector and imposing a condition on the minimum kinetic energy, necessary to reach a certain detector component. The kinematic conditions, imposed on the particles, are summarised in Appendix C. The multiplicity distribution, retrieved from IQMD calculations is shown in panel (a) of Fig. 4.8 as the black histogram. In order, to make the simulated distribution comparable to the experimental one, the trigger conditions have to be included. In the discussed experiment the so-called ‘minimum bias’ condition was applied, requiring more than 4 hits in the PLAWA and at least one hit in the RPC+BAR ToF system. The requested restriction reduces the multiplicity distribution to the blue surface in

possible values.

⁹Note that the Plastik wall is a ToF detector, therefore a distinction between charged particles is not possible without an addition detector - the Helitron, which is not part of the present analysis.

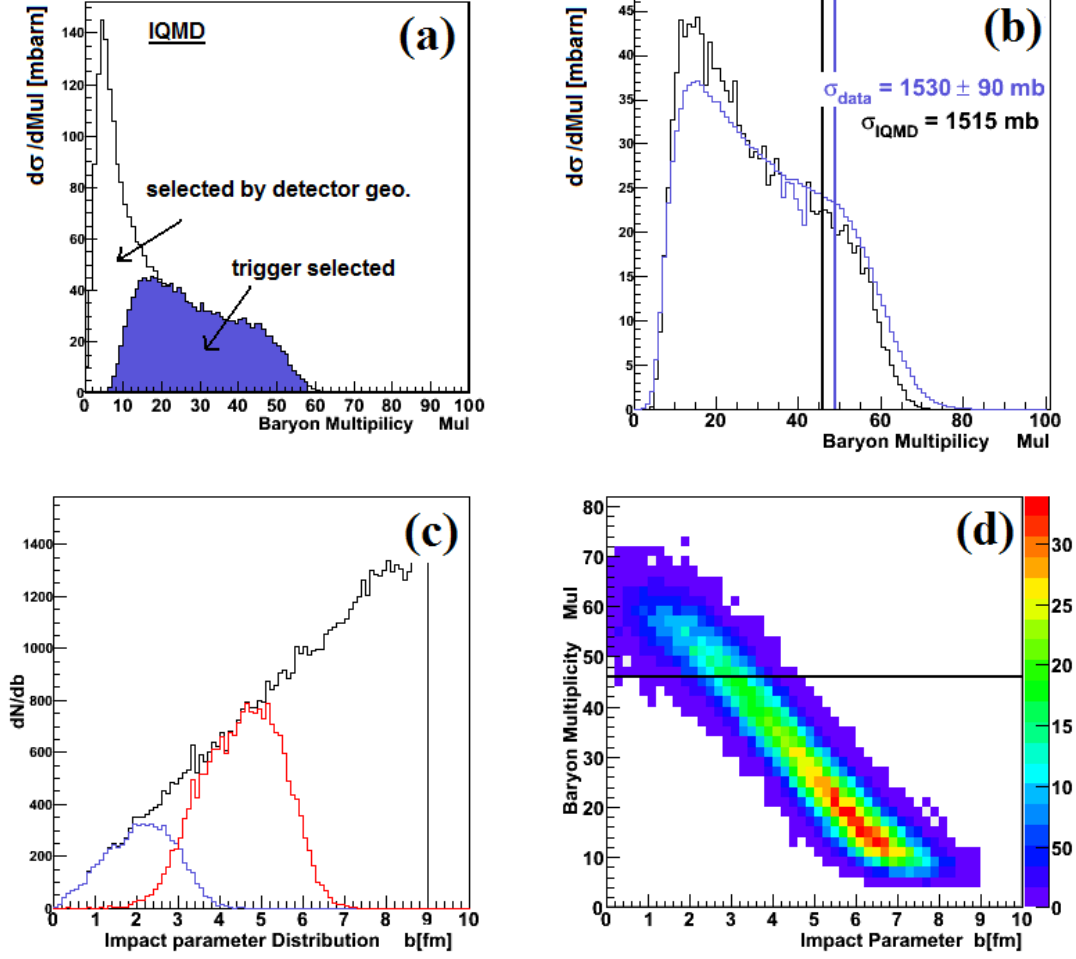


Figure 4.8: Panel (a): Baryon multiplicity (for definition see text) reconstructed from IQMD transport calculations. The blue-coloured area contains only the sub-set of events which fulfil the experimental trigger conditions. Panel (b): Triggered baryon multiplicity obtained with IQMD (black) and in the experiment (blue), each normalised to the respective cross section. Vertical lines separated the regions covering equal integrated cross section. Panel (c): Impact parameter distribution corresponding to a particular baryon multiplicity selection, evaluated within IQMD. Panel (d): IQMD based impact parameter - baryon multiplicity correlation.

panel (a) of Fig. 4.8, i.e. a part of peripheral events is rejected.

Assuming the originally reconstructed multiplicity distribution corresponds to the total geometrical cross section of the reaction, i.e. $\sigma_{geo} = 2711$ mb, then the fraction selected by the experimental trigger conditions corresponds to a cross section of $\sigma_{sel} = 1515$ mb. This value is very close to the experimentally determined $\sigma_{exp} = 1530 \pm 90$ mb. The experimental and IQMD baryon multiplicity distributions, normalised to

respective cross sections, are compared in panel (b) of the Fig. 4.8. Though similar, the distributions exhibit small differences in the amount of very central and very peripheral events.

To achieve the most accurate comparison the multiplicity in the data, Mul_{data} , and the simulated multiplicity, Mul_{IQMD} , are associated to each other by the covered cross section fraction. The blue and black lines in panel (b) of the Fig. 4.8 indicate the choice of the central event selection with $Mul_{data} > 48$ and $Mul_{IQMD} > 46$. The events, selected in this way, amount to a cross section of ~ 300 mb in both distributions.

Of particular interest is the effect the multiplicity selection has on the distribution of the impact parameters. In the evaluated transport calculations both, the impact parameter and the multiplicity are available and therefore their correlation can be studied. Two cases are examined: The central event selection with $Mul_{IQMD} > 46$ and the complementary peripheral selection with $Mul_{IQMD} < 46$. The results are shown in the panel (c) of the Fig. 4.8. The black histogram is the original input of the transport calculation, i.e. a linearly increasing b -distribution. The red and blue histograms are the impact parameter distributions of events with $Mul_{IQMD} > 46$ and $Mul_{IQMD} < 46$, respectively. The obtained b -distributions have a well defined mean value, $\langle b \rangle$, and a width characterised by the r.m.s., Δb , of the distribution. Table 4.3 summarises the definition of event classes used in the following analysis with the corresponding cross section values and parameters of the multiplicity-selected b -distributions.

	Mul_{data}	σ (b)	$\langle b \rangle \pm \Delta b$ (fm)
(a)	[20, 90]	1.09 ± 0.10	3.90 ± 1.41
(p1)	[20, 48]	0.79 ± 0.05	4.54 ± 0.95
(p2)	[13, 43]	0.98 ± 0.05	4.99 ± 1.01
(c1)	[49, 90]	0.30 ± 0.05	2.11 ± 0.80
(c2)	[58, 90]	0.22 ± 0.05	1.7 ± 0.72

Table 4.3: Definition of event classes: (a) total, (p1)/(p2) peripheral and (c1)/(c2) central events. The corresponding cross section σ , mean impact parameter $\langle b \rangle$ and the r.m.s of the b distribution: Δb .

A cluster forming algorithm has to be applied to transport calculations to be able to count the baryon multiplicity. The clustering procedure defines spatially proximate protons and neutrons with relative momentum close to the Fermi momentum into nucleons. For the versions of HSD and IQMD, utilised in the following section to interpret the data, no clustering procedure is/can be applied. The centrality classes have to be chosen by the means of the impact parameter. A priori, there are two possibilities to restrict the centrality: By a sharp cut on the impact parameter or using an impact parameter distribution that corresponds to a certain multiplicity selection, as discussed above. The implications of both method are demonstrated in Fig. 4.9.

The first Fourier coefficient is evaluated as a function of the transverse momentum in the backward rapidity interval $-1.3 < y_0 < -0.5$ for a central (left panel) and a peripheral (right panel) event selection with and without the assumption of a KN in-medium potential (solid and dashed lines, respectively). The centrality selection is

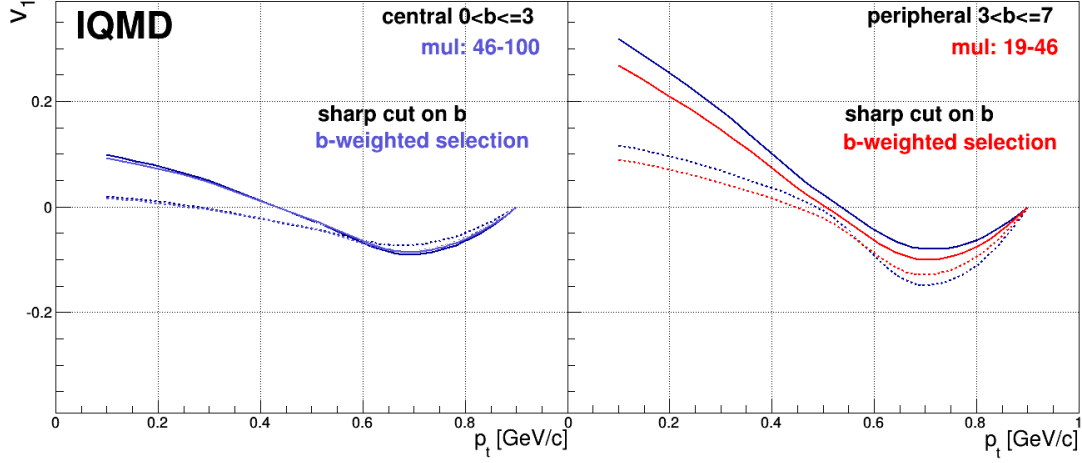


Figure 4.9: Predictions of the IQMD transport approach for in plane flow of K^+ mesons as a function of transverse momentum, p_t , in central (left panel) and peripheral (right panel) event selection. Two centrality selection methods are compared: ‘sharp cut’ on the impact parameter (black lines) and impact parameter fraction selected by imposing restriction of the baryon multiplicity (see Fig. 4.8, panel (c)). Solid lines represent the calculation with the assumption of a KN in-medium potential, dashed lines – the free propagating scenario.

accomplished through a sharp cut on the impact parameter (black lines) or a weighted impact parameter distribution (coloured lines), as depicted in panel (c) of Fig. 4.8. In the central event selection the effect is negligibly small. For the peripheral classification, on the contrary, a significantly deviating set of events is selected. The method of b-weighted selection allows a more accurate comparison of the model calculation and experimental data and therefore is chosen for the following analysis.

4.4 Systematic Investigation of Flow Patterns

In the following section the properties of the first and the second Fourier harmonic for K^+ and K^- mesons are investigated systematically by comparison to transport models. The basic concepts of the utilised calculations, HSD and IQMD, are described in Section 2.4. In order, to facilitate the comparison to the experimental data, results of the transport calculations are filtered for the detector acceptance (see Section 3.2). The applied centrality selection procedure and the used parameters are described in Section 4.3.

The possible influence of an in-medium potential is studied in the divergence of transport calculations with and without the assumption of in-medium modifications. The implemented values of the KN and $\bar{K}N$ in-medium potential at normal nuclear matter density for particles at rest are summarised in Table 4.4. Note that in HSD the \bar{K} are treated in a coupled channel approach. The potential $U_{\bar{K}N}$ of a quasi particles

picture is estimated in order to enable a comparison [Hart98].

	HSD	IQMD
$U_{KN}(\rho_0, p = 0)$	20 ± 5 [MeV]	20 ± 5 [MeV]
$U_{\bar{K}N}(\rho_0, p = 0)$	-50 ± 5 [MeV]	-45 ± 5 [MeV]

Table 4.4: In-medium potentials as employed in presented HSD and IQMD calculations.

The choice of the potential's magnitude is motivated by earlier measurements, as well as, the observed pattern in the presented analysis. The rescattering and absorption processes are, to the best of the knowledge, taken into account by the transport calculations.

4.4.1 Influence of the Coulomb Interaction on the In-Plane Emission Pattern

Charged kaons propagate in nuclear matter under the influence of two different mean field potentials. One is caused by the strongly interacting matter, i.e. the KN or $\bar{K}N$ in-medium potential, which is the subject of the present analysis. The second is generated by electrically charged particles due to electromagnetic interaction. Both interactions are repulsive for K^+ mesons and attractive for K^- mesons and therefore influence the collective motion of the charged K mesons in the same manner.

In contrast to the strong interaction, the Coulomb potential exhibits a $1/r$ distance dependance and therefore impacts the propagation of charged particles not only in the dense phase of the collisions but also on the flight path to the detector.

In the following section the contribution of the Coulomb field to the attraction/repulsion effect in the flow patters is studied separately for the ‘short-range’ and the ‘long-range’ parts of the interaction.

Influence of the Coulomb Potential within the Interaction Region

In the isospin symmetric system K^+/K^- and K^0/\bar{K}^0 are treated equally by the strong interaction. The influence of the Coulomb interaction can be studied by the comparison of the flow patterns of charged K mesons and their neutral counterparts. Note: The mixing of strong eigenstates K^0 and \bar{K}^0 into weak eigenstates K_S^0 and K_L^0 is not included in transport calculations for being considered negligible for the current discussion.

Fig. 4.10 shows the in-plane flow, obtained with HSD transport calculations, as a function of rapidity, integrated over the full momentum range. In the left panel the flow patters of K^+ and K^0 are compared with and without the assumption of a strong KN -potential (solid and dashed lines, respectively). Free propagating kaons (purple-coloured, dashed line) exhibit an isotropic distribution in the plane of the reaction, i.e. $v_1 \sim 0$. Influence of every additional potential manifests itself in the cumulatively repulsive behaviour. The amount of ‘anti-flow’ with respect to protons gradually increases.

The right panel in Fig. 4.10 shows a similar comparison in the antikaon sector. The in-plane propagation of K^- and \bar{K}^0 mesons is slightly influenced by the Coulomb inter-

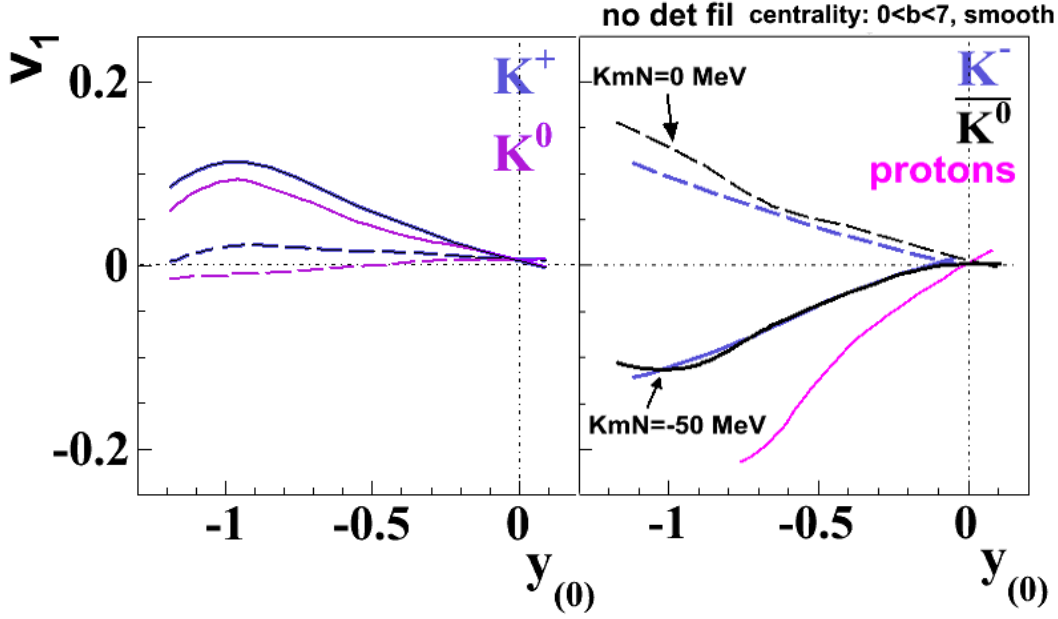


Figure 4.10: HSD simulations of the directed flow pattern as a function of normalised rapidity for kaons (K^+ and K^0) (left panel), antikaons (K^- and \bar{K}^0) and protons (right panel). Solid lines reflect the flow patterns under the influence of a KN - and $\bar{K}N$ in-medium potentials, respectively. The dashed lines depict the results without. No detector filter is applied.

action if the antikaons do not feel a strong potential (dashed lines). If a $\bar{K}N$ in-medium potential is active, it dominates the attraction toward nucleons. The contribution from the Coulomb attraction is negligibly small.

Transport models describe the evolution of the colliding system up to 40-50 fm/c¹⁰. The ‘final state’ phase space distribution, obtained in calculations, is a snapshot at that point in time. Due to the infinite range of the Coulomb potential, especially the in-plane distribution of charged kaons can be altered by the influence of the Coulomb field on the flight path to the final observation. Particularly in peripheral collisions, the presence of a large amount of charged spectators can affect the experimental final state observables.

Influence of the Coulomb Potential on the Long Range

The long range effect is studied by modifying the phase space distribution, obtained in HSD calculation, with the **SACA**¹¹ approach [PurAic00].

SACA is a clusterisation algorithm in the framework of the Quantum Molecular Dynamics. The main purpose of the algorithm is to study the cluster formation in heavy ion reaction at intermediate energies. One aspect of the algorithm is its ability to simulate the Coulomb influenced trajectory of a particle/cluster up to around 10,000 fm/c. The latter is used in the following for our purpose.

¹⁰IQMD calculations are executed up to $t = 40$ fm/c. HSD calculation grid extends up to $t = 50$ fm/c

¹¹Simulated Annealing Clusterisation Algorithm.

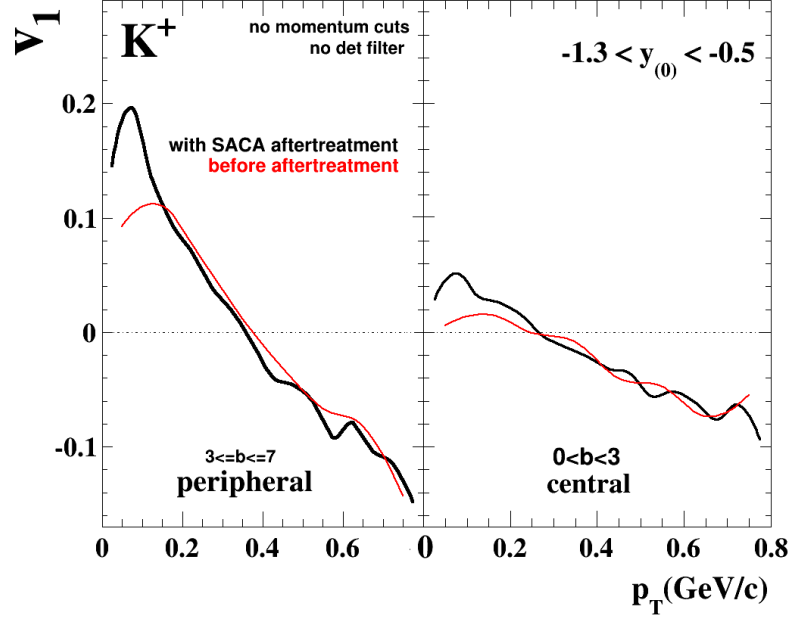


Figure 4.11: Differential directed flow of K^+ mesons obtained within HSD calculations before (red curves) and after (black curves) the simulation of a flight path in the Coulomb field. See text for details. Note: The centrality classes are selected by a sharp cut on the impact parameter distribution.

Fig. 4.11 shows the directed flow observable of K^+ mesons in the differential representation as a function of transverse momentum in a rapidity interval around the target rapidity ($y_0^{tar} = -1$). The events are divided into two centrality classes by restricting the impact parameter to $b < 3$ (right panel) and $b > 3$ (left panel). A significant influence is observed for slow kaons, i.e. $p_t < 0.2$ GeV/c. The largest deviation is caused by the positively charged target remnant, containing the biggest amount of spectators in peripheral collisions (left panel). The observed effect lies beyond the detector acceptance and therefore is not relevant for the description of the experimental data.

In Fig. 4.12 the consequences of the Coulomb-path simulation are depicted for different particle species. Integrated over the full momentum range, no modification of the azimuthal emission pattern remains for K^+ and K^- mesons. The contribution from slow kaons is overshadowed by the faster ones.

The flow of protons (left panel) in the kinematic region of the target is influenced by the spectators. Protons with small momenta inside the target remnant do not exhibit collective motion, but do contribute to the integrated v_1 value. An increment is visible around the target rapidity. By applying the SACA clusterisation algorithm, the target protons are bound into nucleons, i.e. are not classified as protons any longer, and the incremented contribution decreases.

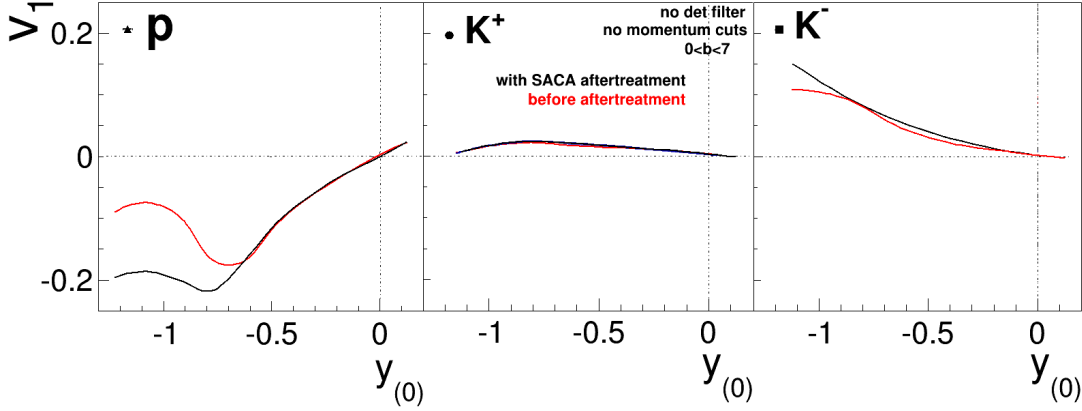


Figure 4.12: HSD predictions of integrated directed flow pattern for protons (left panel), K^+ mesons (middle) and K^- mesons (right panel). The influence of a long flight path in a Coulomb potential, simulated with the SACA algorithm, is shown by the black lines. The results of a ‘regular’ HSD calculation (red lines) provide the reference. The depicted HSD version does not contain any in-medium potentials.

4.4.2 First Fourier Coefficient

The first harmonic coefficient, v_1 , describes the collective deflection of particles in the reaction plane. Collective behaviour was observed to be sensitive to possible in-medium modifications as it is interpreted as an attraction/repulsion between kaons and nucleons¹². The reconstruction method and applied corrections are summarised in Section 4.2. In the following section the first Fourier coefficient of charged kaons is examined for its general trends, momentum dependance and centrality dependence (as far as possible with the statistics of the available data sample).

Fig. 4.13 (upper row) shows the rapidity dependance of the first Fourier coefficient for protons, K^+ mesons and K^- mesons. The v_1 coefficients are integrated over the full transverse momentum range and the complete available centrality range (corresponds to the centrality class (a) in Table 4.3).

Protons (left panel) exhibit a strong collective in plane motion in a preferred direction. Both transport descriptions reproduce the proton directed flow pattern very well. Detailed evaluation of the proton (and heavier baryons) flow patterns from the S325 run-time can be found in [VZDTh]. In the present discussion the protons are shown merely for reference purposes.

K^+ mesons (middle) show a weak collective deflection, opposite with respect to protons – the so-called ‘anti-flow’. The largest in-plane deflection is observed around the target rapidity. Both models agree in predicting a nearly isotropic distribution of K^+ mesons without the influence of a KN -potential (dashed lines). The amount of observed ‘anti-flow’ is reproduced by the IQMD calculation under the assumption of a KN -potential of $U_{KN} = 20$ MeV and slightly overestimated by an analogous HSD

¹²Interpretation in the mean field picture.

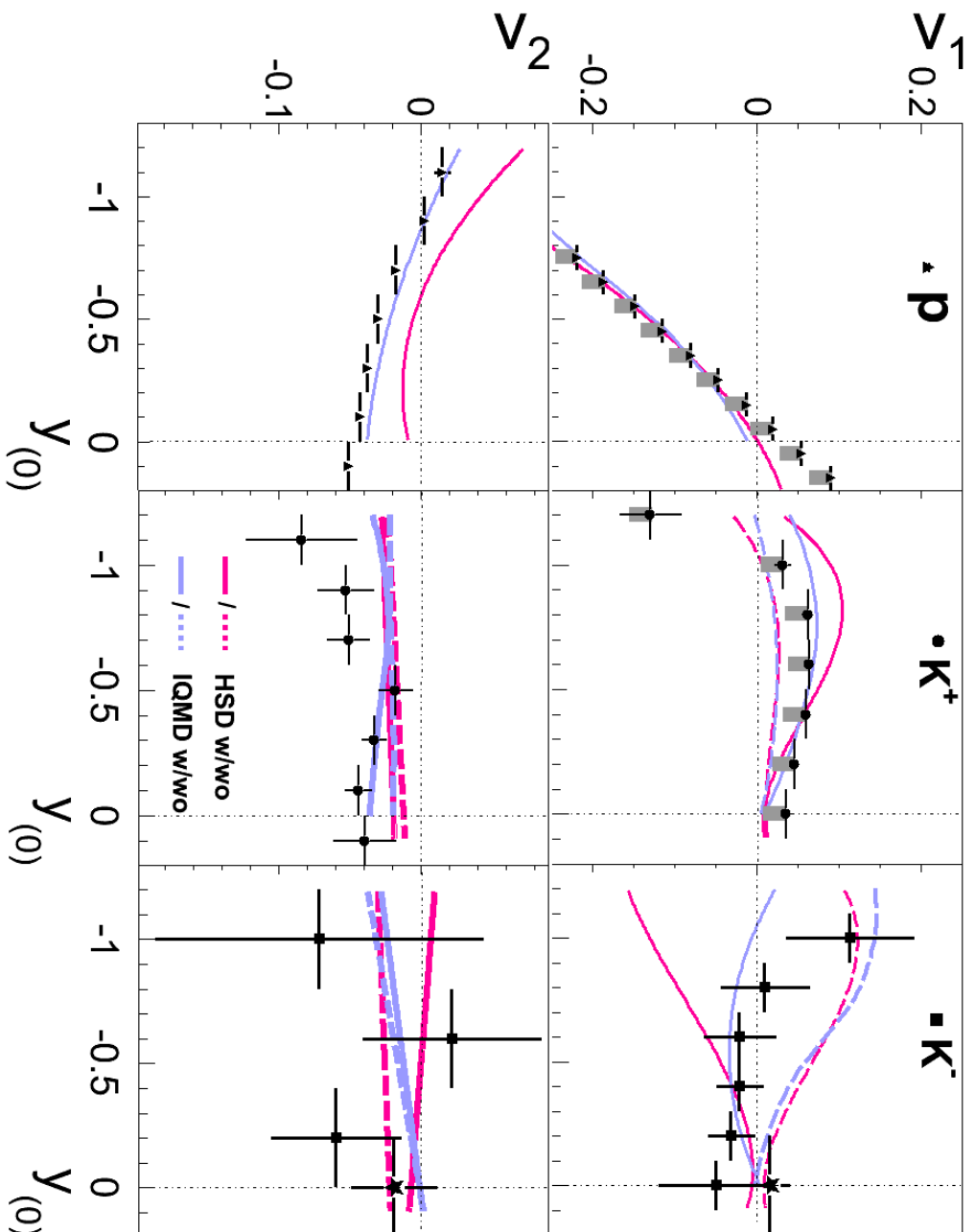


Figure 4.13: First (upper row) and second (lower row) Fourier coefficient as a function of normalised rapidity for protons (left panel) K^+ mesons (middle) and K^- mesons (right panel). The experimental data is compared to the predictions of HSD (magenta) and IQMD (blue) transport calculation with (solid lines) and without (dashed lines) in-medium modifications. The star point in the right panel originates from a subset of runs with improved resolution. The figures are published in [Zim14].

predictions.

The reconstructed emission patterns of K^- mesons (right panel) reveal an isotropic emission, within large statistical uncertainties. Without in-medium potentials both models predict a strong ‘anti-flow’. The observed isotropic flow pattern is best reproduced by the in-medium modified IQMD calculations. HSD calculations, with implemented in-medium potential, predict a collective deflection similar to the one of protons. The data show no indication of such behaviour. The measured K^- flow suggest a slightly lower repulsion than implemented in IQMD. The observed agreement is rather surprising, since in IQMD antikaons are described in a non-legitimate quasi particle approach¹³.

The relatively high number of reconstructed K^+ mesons allow to study their flow pattern in differential way. Available events are divided into two centrality classes, defined in Table 4.3 as (p1) and (c1), and evaluated as a function of transverse momentum in a rapidity interval $-1.3 < y_0 < -0.5$ around the target rapidity $y_0 = -1$, where the largest flow effect is observed. The results are shown in Fig. 4.14.

Directed flow of K^+ mesons exhibits a strong momentum dependence. Production close to threshold energies ensures, that kaons are produced with low momentum. The low- p_t behaviour is dominated by the pressure gradient (larger in peripheral collisions) and the influence of the potential. Kaons gain momentum in scattering processes with predominant protons. Therefore, the collective behaviour of high- p_t kaons is close to the one of protons.

In central collisions the behaviour of K^+ mesons is described by both transport calculations, with employed in-medium potentials. In the peripheral event selection the in-medium modified HSD calculation overestimates the amount of ‘anti-flow’ for the low momentum kaons. IQMD, on the contrary, explains the low momentum behaviour with the presence of the in-medium potential, but does not reproduce the momentum dependence. This representation reveals, that the contribution from low momentum kaons is responsible for the discrepancy of HSD predictions and experimental data in the integrated representation, as shown in Fig. 4.13 (upper row).

Collective motion of K^+ mesons has been investigated in previous measurements of the same system at the same energy by the FOPI collaboration¹⁴. The results are published in [Cro00]. The comparison of the present analysis with the results from the literature is shown in Fig. 4.15. The recent data set was reduced to the centrality class (c2) of Table 4.3, in order to make both data samples comparable. The directed flow patterns of both experiments show a beautiful agreement.

The comparison to HSD calculations in this slightly more central event selection, confirms the statement of HSD being able to reproduce the flow behaviour of K^+ mesons in central collisions.

¹³See Chapter 2 for details.

¹⁴Note that, though same colliding system and same beam energy, the recent experiment was performed with an improved detector setup, and larger triggered cross section.

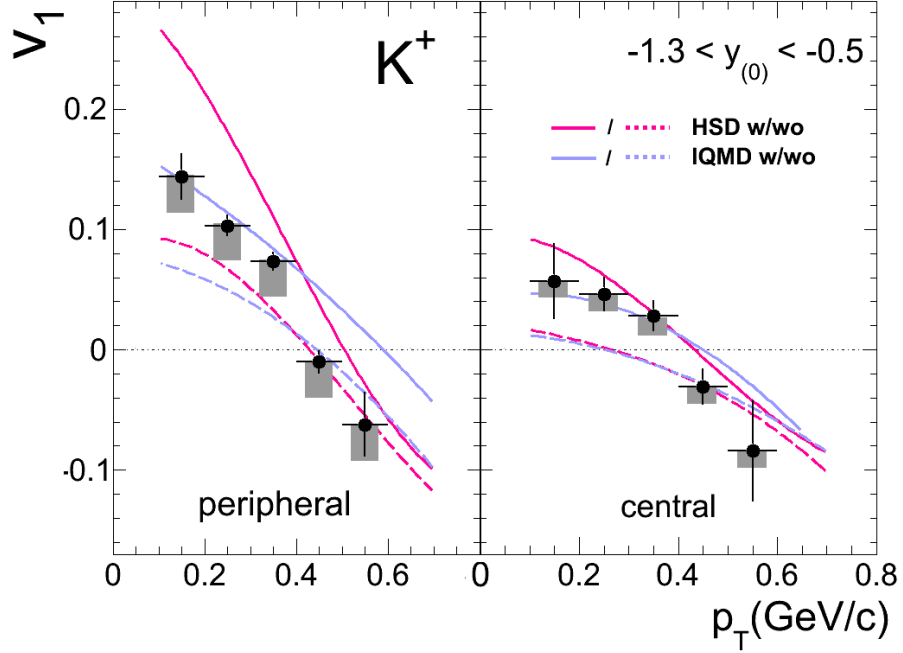


Figure 4.14: Differential representation of the first Fourier coefficient obtained for K^+ mesons in peripheral (left panel) and central (right panel) event classes in comparison to the predictions of HSD and IQMD transport approaches [Zin14]. See text for details.

4.4.3 Second Fourier Coefficient

The second harmonic coefficient, $v_2 = \langle (p_x - p_y)/p_t \rangle$, characterises the collective propagation in all transverse directions by comparing the in-plane and the out-of-plane deflection.

Fig. 4.13 (lower row) shows the momentum and centrality¹⁵ integrated v_2 coefficient of protons, and charged kaons as a function of normalised rapidity.

Protons show a slight out-of-plane emission signature. At mid-rapidity, the only component is the emission perpendicular to the reaction plane. Toward the target rapidity, the out-of-plane component gets superimposed by the increasingly negative in-plane component - v_1 . Similar to v_1 coefficients, the elliptic flow of protons from the considered run-time is investigated extensively in [VZDTh]. The IQMD transport approach describes the proton dynamics successful. The presented HSD prediction reproduce the rapidity dependance, but overestimate the amount of elliptic flow, presumably due to the lack of the clusterisation procedure.

K^+ mesons exhibit a weak squeeze out, indicated by negativ v_2 values at mid-rapidity, and nearly no rapidity dependance. Similar behaviour is observed for a peripheral event selection, see Fig. 4.16. Both models reproduce the data, but do not show any sensitiv to possible in-medium potentials beyond mid-rapidity. At mid-rapidity

¹⁵Centrality class (a) as of Table 4.3.

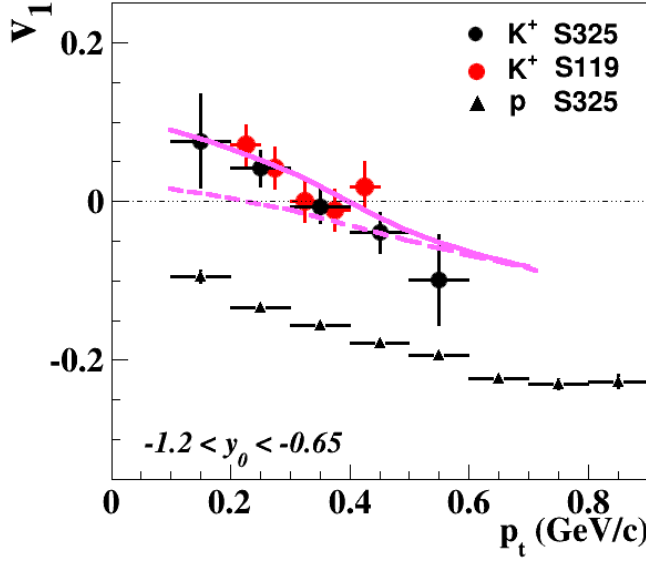


Figure 4.15: In-plane flow of K^+ mesons and protons as a function of transverse momentum within a fix rapidity window. The flow patterns are shown for a central event selection, defined in Table 4.3 as (c2). The experimental data is compared to the predictions of HSD transport calculation with and without the assumption of an in-medium potential. The results of the recent analysis are compared to the measurements published in [Cro00].

the observed squeeze out is explained within IQMD by an additional repulsion, due to the in-medium potential.

Large statistical uncertainties in the K^- elliptic flow pattern do not allow for any conclusions, but the observations support the presumption of an isotropic emission pattern, as deduced from the directed flow pattern. Theoretical modelling is successful in describing the $K^- v_2$ coefficient, however no insight into a possible in-medium modification can be gained.

Azimuthal emission patterns of K^+ and K^- mesons in Ni + Ni collisions at an incident beam energy of 1.9 AGeV were also studied by the KaoS collaboration. The results are published in [Uhl05]. In a peripheral event sample of $3.8 \text{ fm} < b < 6.5 \text{ fm}$ the KaoS collaboration measured v_2 values of $v_2(K^+) = -0.05 \pm 0.03$ and $v_2(K^-) = 0.09 \pm 0.06$. The azimuthal distributions were evaluated at mid-rapidity.

In Fig. 4.16 KaoS data points are compared to the FOPI data. For this purpose the recent data set was reduced to the (p2) centrality sample, as classified in Table 4.3. Additionally the detector acceptance was, as far as possible¹⁶, adapted to the conditions of the KaoS experiment.

The squeeze out signature of K^+ mesons, as seen by the KaoS collaboration, could be confirmed by the current analysis. In case of K^- mesons, the published measurement claims a positive v_2 value, i.e. an in-plane ejection. The results of both experiments are comparable within the statistic inaccuracy, however the FOPI data do not show any

¹⁶A small part of the phase space region that was accessible with KaoS is not accessible with FOPI.

indication of in-plane emission.

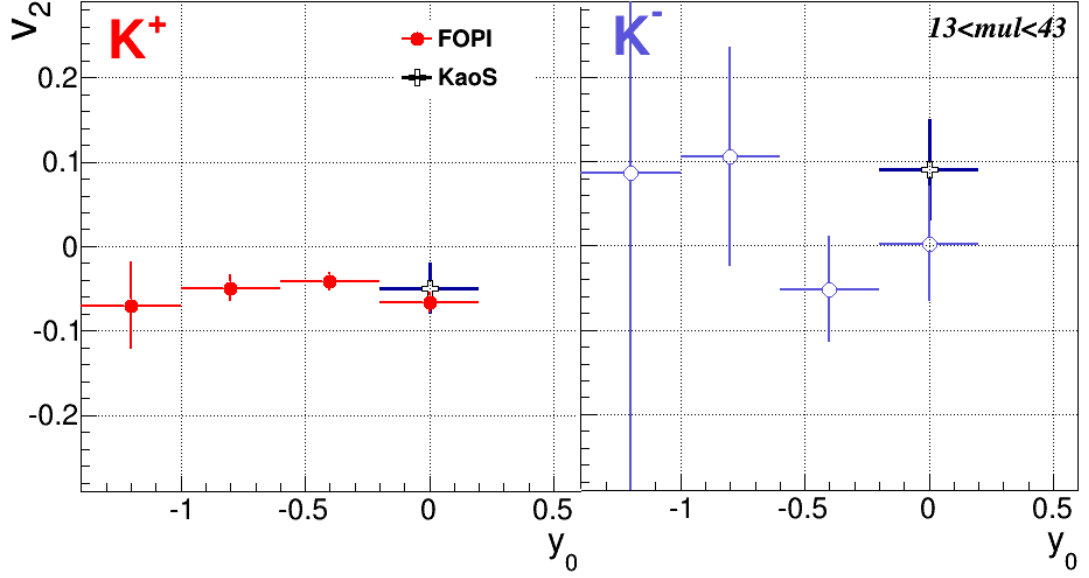


Figure 4.16: Elliptic flow coefficient, v_2 , as a function of rapidity for K^+ mesons (left panel) and K^- mesons (right panel), measured by the FOPI (circular symbols) and the KaoS (cross symbols) collaborations. The coefficients are integrated over the transverse momentum range $0.2 \text{ GeV}/c < p_t < 0.8 \text{ GeV}/c$. The centrality selection corresponds to (p2) from Table 4.3. ‘KaoS’ data points are taken from [Uhl05].

In Fig. 4.17 the elliptic flow patterns are compared to the transport calculations. The dynamic behaviour of both K mesons is reproduced by the models. No discrimination of flow patterns with and without the influence of an in-medium potential is possible with the statistics of the available data sample. Neither HSD nor IQMD predict any in-plane emission of K^- mesons, as suggested by the KaoS observations.

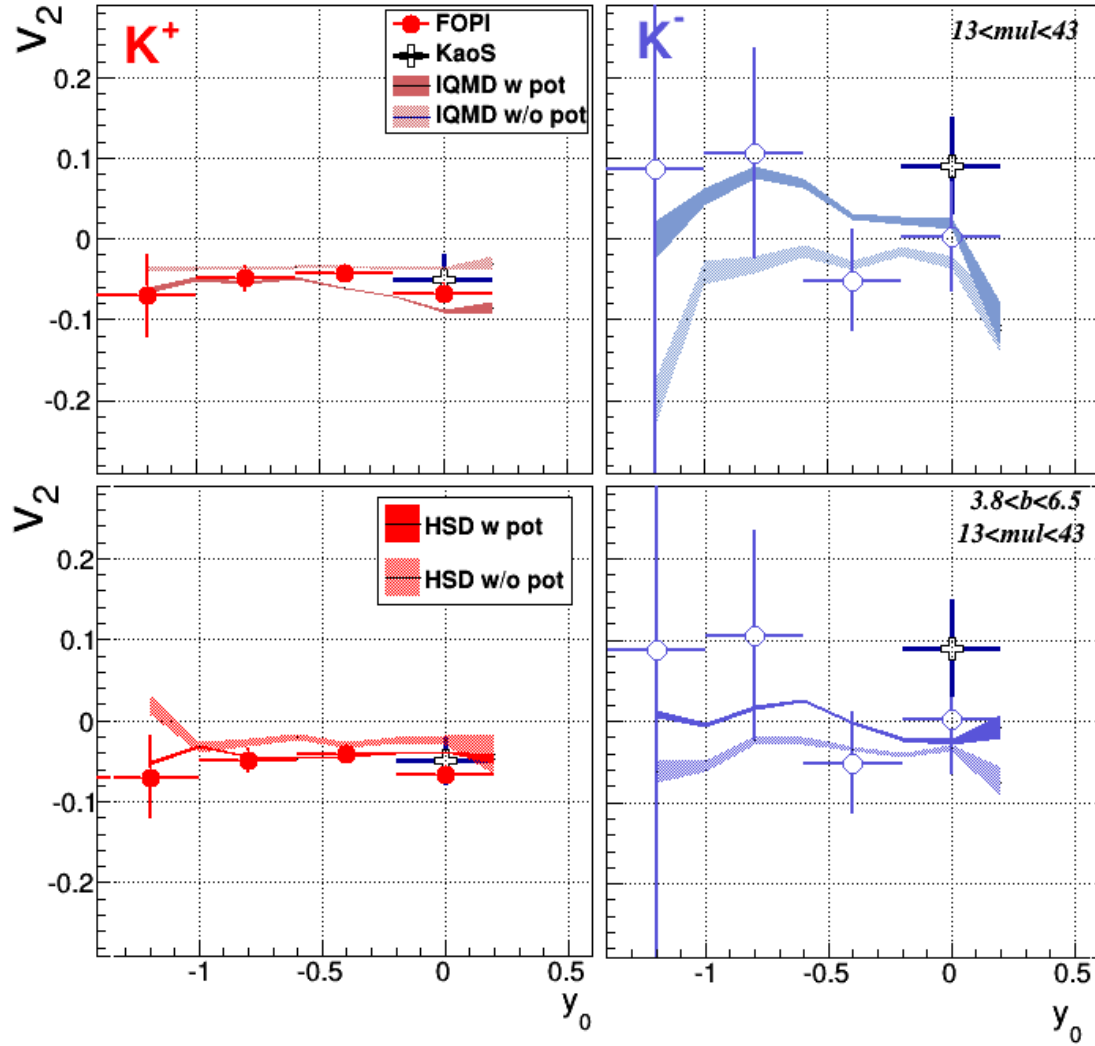


Figure 4.17: v_2 , as a function of normalised rapidity. Data points as in Fig. 4.16. Shaded bands correspond to the results of transport model calculations. The band's width indicates the statistical error of the calculation. 'KaoS' data points are taken from [Uhl05].

Chapter 5

The S339 Experiment

In the course of the ‘S339’ experiment a secondary beam of negatively charged pions with a beam momentum of $p_{\pi^-} = 1.7$ GeV/ c was directed at a light, medium-sized and heavy targets: ^{12}C , ^{63}Cu and ^{208}Pb . Technical details of the experimental conditions can be found in Section 3.5.

This experiment was motivated by an earlier FOPI measurement of K_S^0 mesons produced in pion reactions with a heavy and light targets. The resulted observable, see in Fig. 5.1, showed sensitivity to the in-medium modifications of kaons and could be successfully described within the HSD transport approach.

The ‘S339’ experiment aimed at verifying the previous observations and challenge the theoretical modelling of reactions at higher energy. The new experimental conditions open the possibility to expand the study of the in-medium effects at normal nuclear matter density to further strange particles. The available center of mass energy of $\sqrt{s} = 2.02$ GeV allows, beside the associated production, for the direct production of kaon-antikaon pairs and, therefore, also opens the phase space for the ϕ meson.

Possible production channels and the corresponding threshold momenta of the incident pion in a fix-target scenario are summarised in Table 5.1. The corresponding measured cross sections are listed, as far as available, in Appendix F. The largest cross section of ~ 200 μb is observed, naturally, for the associated production channel: $\pi^- + p \rightarrow \Lambda K^0$. The direct production of K^+K^- pairs is suppressed by an order of magnitude in comparison. At a slightly lower pion incident energy of $p_{\pi^-} = 1.59$ GeV/ c a production cross section of $\sigma_{\pi^- + p \rightarrow n K^+ K^-} = 11 \pm 6$ μb was measured.

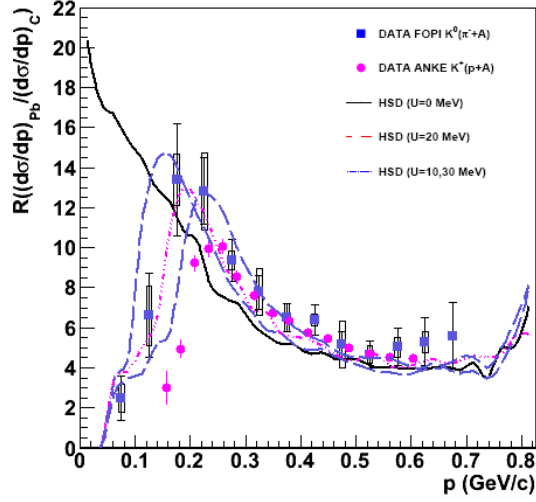
The ϕ meson production, in considered reactions, is associated with a cross section of $\sigma_{\pi^- + p \rightarrow n \phi} = 29 \pm 15$ μb . Note that it is the only production channel under the discussed experimental conditions. Particularly, the production in a $\pi^- + n$ reaction¹ requires more energy in the center of mass, than available.

The mean free path of a pion at $p_{lab} = 1.7$ GeV/ c in ordinary nuclear matter is $\lambda = 1.5$ fm. The pion is likely to undergo reactions with the nucleons on the surface of the target nucleus². A part of the particles, produced in these reactions, propagate through the nucleus and therefore are exposed to the influences of the nuclear matter

¹Only the strong interaction production channels are considered.

²The diameter of the carbon nucleus is $d_C = 5.5$ fm and of a lead nucleus $d_{Pb} = 14.2$ fm

Figure 5.1: Momentum distribution ratio of K_S^0 mesons, measured by FOPI, and K^+ mesons, measured by the ANKE collaboration [Ben09]. The experimental results are compared to the predictions of the HSD transport approach for K_S^0 meson with a various assumptions for the KN in-medium potential.



at normal density - ρ_0 . Comparison of the final state phase space distributions observed in reactions with the light and heavy targets can bear indications of in-medium effects.

The upcoming chapter starts with the overview of the reconstructed charged particles in reactions with different targets. Special emphasis is put on the evaluation of charged kaons and the description of the background contribution around the nominal kaon mass. To prepare the discussion of neutral particles, the reconstruction strategy is introduced and the background description by the so-called mixed-event method is explicated.

The obtained K^+ and K^- signals can be used to reconstruct ϕ meson candidates. The resulting ϕ signals, measured with different targets, are compared. The reconstruction efficiency is estimated within Geant detector simulations.

The spectrum of accessible strange particles is completed by the measurements of the Λ baryon and electrically neutral K_S^0 meson signals. The results of the reconstruction are shown. The challenges and solutions in the background description at low momenta are addressed. Possible effects of the medium are discussed by the diversities in the phase space distributions measured in light and heavy targets.

The chapter is concluded by the comparison of the obtained results among each other and to the predictions of the HSD transport approach.

5.1 Charged Particles in C, Cu und Pb Targets

The general strategy of the charged particle identification with FOPI is discussed in Section 3.3. Fig. 5.2 and Fig. 5.3 illustrate the results of the primary reconstruction.

In Fig. 5.2 the energy loss, as obtained in the CDC sub-detector, is depicted as a function of laboratory momentum and sorted by charge. Hereby no matching between the ToF system and the CDC was required in order to sustain the largest possible number of tracks and especially not to reject low momentum particles. To ensure the track quality anyway, topological conditions are imposed. The maximal distance between the extrapolated track and the primary vertex in the beam direction, z_0 , is restricted to 18

	K^0 production	Threshold $p_{lab}[\text{GeV}/c]$	K^+ production
$\pi^- + p \rightarrow$	ΛK^0	0.89	
	$\Sigma^0 K^0$	1.03	$\Sigma^- K^+$
	$\Lambda K^0 \pi^0$	1.14	$\Lambda K^+ \pi^-$
	$\Sigma^{+0/-} K^0 \pi^{-0/+}$	1.29 ± 0.01	$\Sigma^{0/-} K^+ \pi^{-/0}$
	$\Sigma_{1385}^0 K^0$	1.39	$\Sigma_{1385}^- K^+$
	$\Lambda K^0 2\pi$	1.42	$\Lambda K^+ 2\pi$
	$\Lambda_{1405} K^0$	1.44	
	$p K^0 K^-$	1.49	
	$n 2 K^0$	1.50 ± 0.01	$n K^+ K^-$
	$\Sigma^{+0/-} K^0 2\pi$	1.56 ± 0.02	$\Sigma^{+/-} K^+ 2\pi$
	$2 K^0 (34.2\%) \leftarrow$	$n \phi$	$\rightarrow (48.9\%) K^+ K^-$
		1.56	
	$K^0 \pi^0 \leftarrow$	$\Lambda \mathbf{K}_{890}^{*0}$	$\rightarrow K^+ \pi^-$
		1.68	
	$\Lambda_{1520} K^0$	1.68	
$\pi^- + n \rightarrow$	$\hookrightarrow N \bar{K} (45\%)$		
	$\Lambda K^0 3\pi$	1.71 ± 0.01	$\Lambda K^+ 3\pi$
	$\Lambda_{1405} K^0 \pi^0$	1.73	$\Lambda_{1405} K^+ \pi^-$
	$\Sigma_{1385}^{+/-} \pi^{-/+} K^0$	1.69	$\Sigma_{1385}^{0/-} \pi^{-/0} K^+$
	$\Sigma^- K^0$	1.038	
$\pi^- + d \rightarrow$	$\Sigma^- K^0 \pi^0$	1.293	$\Sigma^- K^+ \pi^-$
	$\Sigma^- K^0 2\pi$	1.587	$\Sigma^- K^+ 2\pi$
	$n K^0 K^-$		
	$\Sigma^- p K^0$	0.89	$\Sigma^- n K^0$

Table 5.1: Production channels of strange particles in π^- -induced reactions with corresponding threshold momentum for the incident pion. The values are taken from [LanBor]. The errors originates from a slight difference between the threshold momenta for the production of K^+ and K^0 mesons. Measured cross sections for the listed reactions are summarised, as far as available, in Appendix F.

cm. In the transverse direction only tracks with maximal deviation of 1.4 cm from the nominal vertex position are accepted. Additionally a track was required to have at least 30 hits in the CDC volume. The latter is necessary to ensure the proper performance of the tracking algorithm. Finally, wide preselection windows are applied around the nominal particles masses, in order to reject the misidentified tracks.

Different panels of the Fig. 5.2 show the obtained correlation for the reaction with different targets. Note that the recorded number of events was similar for the carbon and lead targets and about half as large for the copper target. For details see Section 3.5. In the lead target more heavier fragments are reconstructed than in the lighter one. Furthermore, the contamination of the slow K^+ mesons by slow protons is slightly

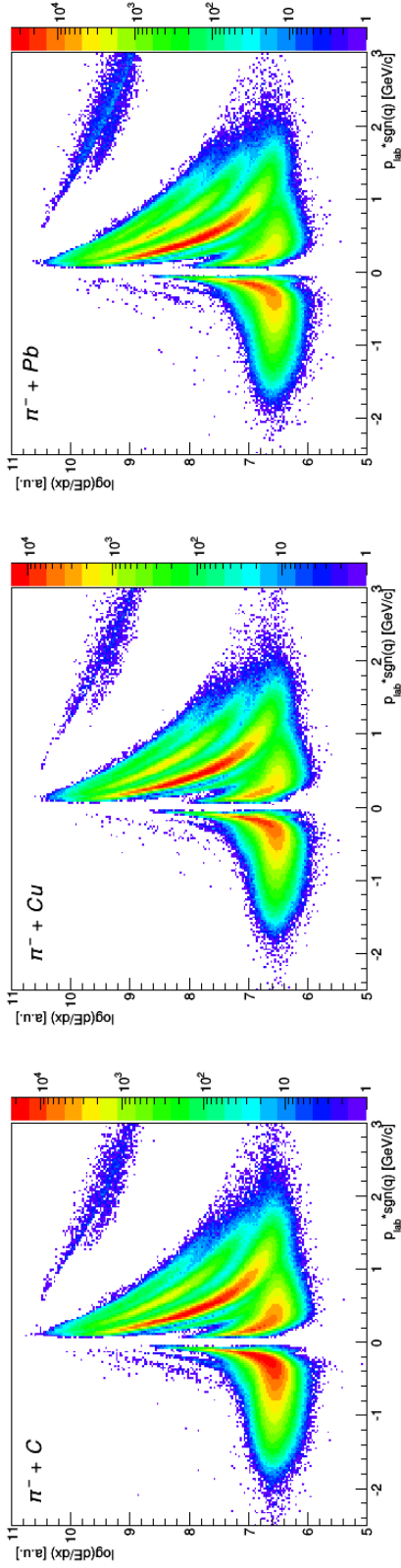


Figure 5.2: Logarithmized energy loss, measured in the CDC, as a function laboratory momentum, sorted by charge. Carbon (left panel), Copper (middle) and Lead (right panel). Here no matching between CDC and the ToF system was required.

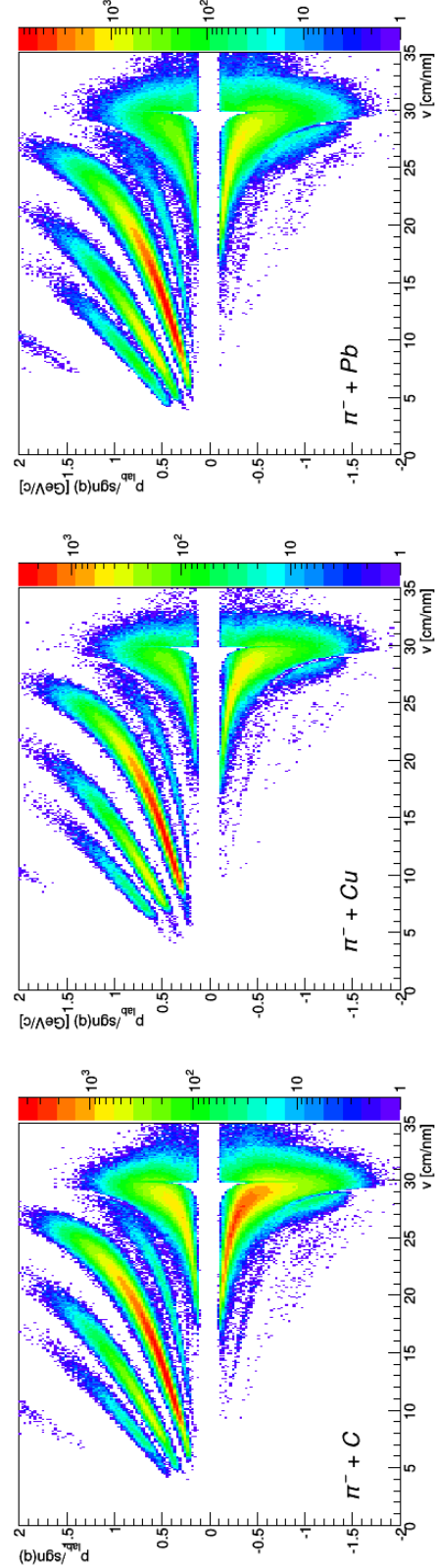


Figure 5.3: Momentum - velocity correlation of the tracks, fulfilling the matching requirement with the BAR + RPC ToF system. See text for details.

larger. Both observations are a consequence of a larger amount of target nucleons. In the light particle segment, the distributions from different targets look very similar.

The identification capability of particles faster than $p_{lab} = 0.1$ GeV/ c can be significantly improved by the supplementary information of the RPC+BAR ToF system. The momentum - velocity correlation for the successfully matched tracks is shown in Fig. 5.3. The matching requirements include a restriction of the maximal azimuthal deviation of the tracks, dph , with $dph_{RPC} = 0.5$ and $dph_{BAR} = 1.5$ and a maximal longitudinal aberration, dz , of $dz_{RPC} = 5$ cm and $dz_{BAR} = 7$ cm. The values for the individual sub-detectors differ due to the dissimilar resolution. Measurement of the velocity faster than the speed of light is an artefact of a finite time resolution of the ToF detector sub-system. The comparison between different targets exhibit the same behaviour as the energy loss - momentum correlation. A distinct identification of K^+ mesons is possible up to $p_{max} = 1.0$ GeV/ c . K^- mesons appear to experience a kinematical limitation. The corresponding p - v branch abates after $p_{max} = 0.5$ GeV/ c . A visibly smaller amount of K^- mesons is reconstructed in the lead target.

The mass spectra of the combined CDC-ToF analysis are depicted in Fig. 5.4. The mass is multiplied by the sign of the electrical charge to separate positively and negatively charged particles. The ‘sharp edges’ are the result of the mentioned mass preselection. The impact of the momentum restrictions for the identification of charged kaons is demonstrated by the comparison of the black and coloured curves. The black histogram includes all the tracks which fulfil the matching requirements. The coloured curves show the mass distributions for particles slower than the imposed momentum restrictions, i.e. $p_{max} = 0.5$ GeV/ c for negatively charged particles and $p_{max} = 1.0$ GeV/ c for the positive ones. The background around the nominal K^- mass is significantly reduced. A clear K^- signal is revealed above the pion tail. In the case of K^+ mesons the restriction does not affect the PID³ capability.

Note that the signal around the negative proton mass is due to misidentified tracks.

5.2 Reconstruction of K^+ and K^- Mesons

Successful matching between the CDC and the ToF system puts restrictions to particles’ momentum, rejecting the highly bent low momentum tracks. The imperfections of the matching efficiency reduce the amount of kaon candidates furthermore. For the analysis of the possible medium influence the slow kaons are of particular interest. In order to maximise the number of kaon candidates and sustain the low momentum contribution the evaluation of the charged kaon signals is performed separately for the matched tracks and the remaining sub-set of tracks. The latter still, however, fulfil the track quality requirements, as discussed above.

For the evaluation of the charged kaon signals, the available kinematic range is divided into momentum intervals. In each momentum bin the mass spectrum is inspected and kaon candidates are defined by a ‘window’ around the nominal kaon mass. The kaon candidates in the matched analysis are clearly distinguishable from other particles. The signals at low momenta, measured in the CDC in the not-matched analysis,

³PID is an acronym for **P**article **I**dentification.

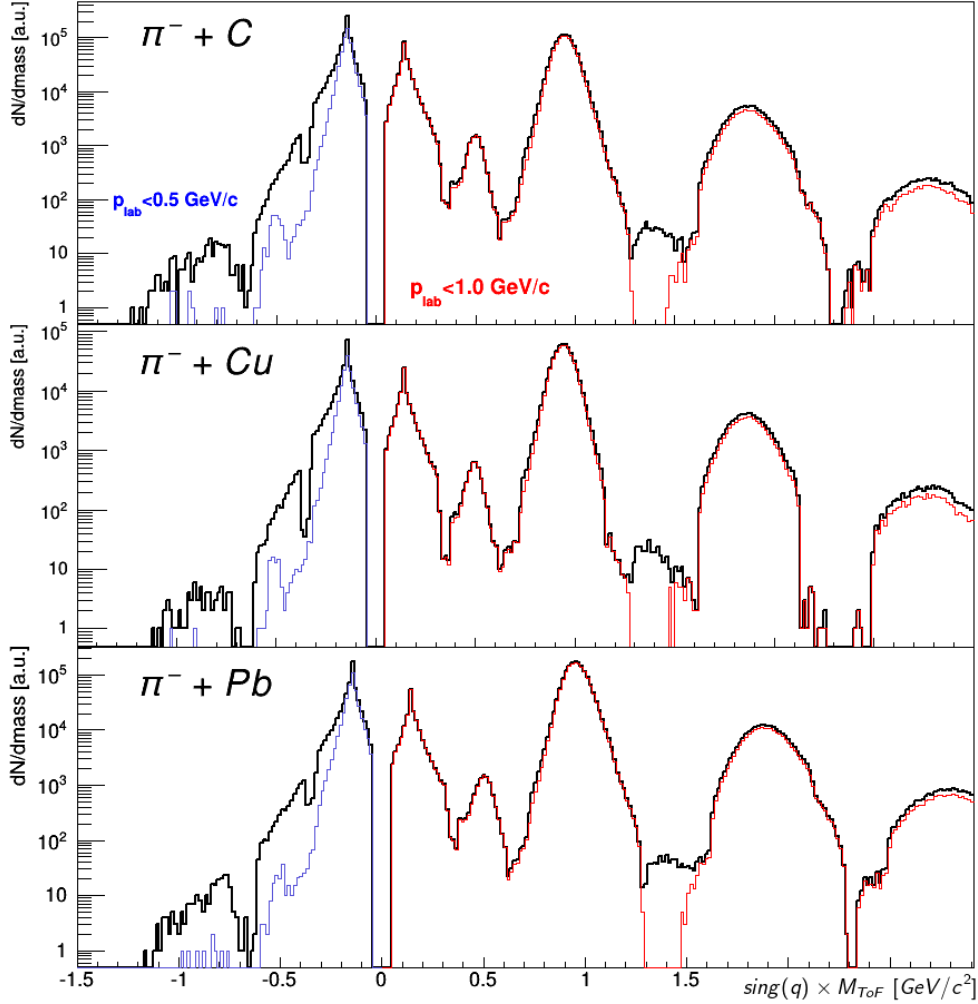


Figure 5.4: Mass distribution measured within the BAR + RPC ToF system and differentiated by charge. Coloured histograms are obtained by imposing restriction to particles' momenta. Note: Wide preselection windows are applied around the nominal particles' mass.

are (partially) superimposed by the background. In the following, the strategy of the background description is discussed in detail.

Fig. 5.5 shows the lowest momentum bins for the K^- identification, evaluated solely in the CDC. The 'window' for the candidate selection is indicated by the vertical, blue lines. The background is estimated by the contribution from the π^- mesons, depicted by the black lines. For the final selection of K^- candidates the background fraction is subtracted.

The background under the K^+ signal has different contributions. As an example, a mass spectrum of positively charged particles with a momentum selection: $p_{lab} = [0.24-0.29]$ GeV/c is shown in Fig. 5.6. The background under the K^+ peak can be

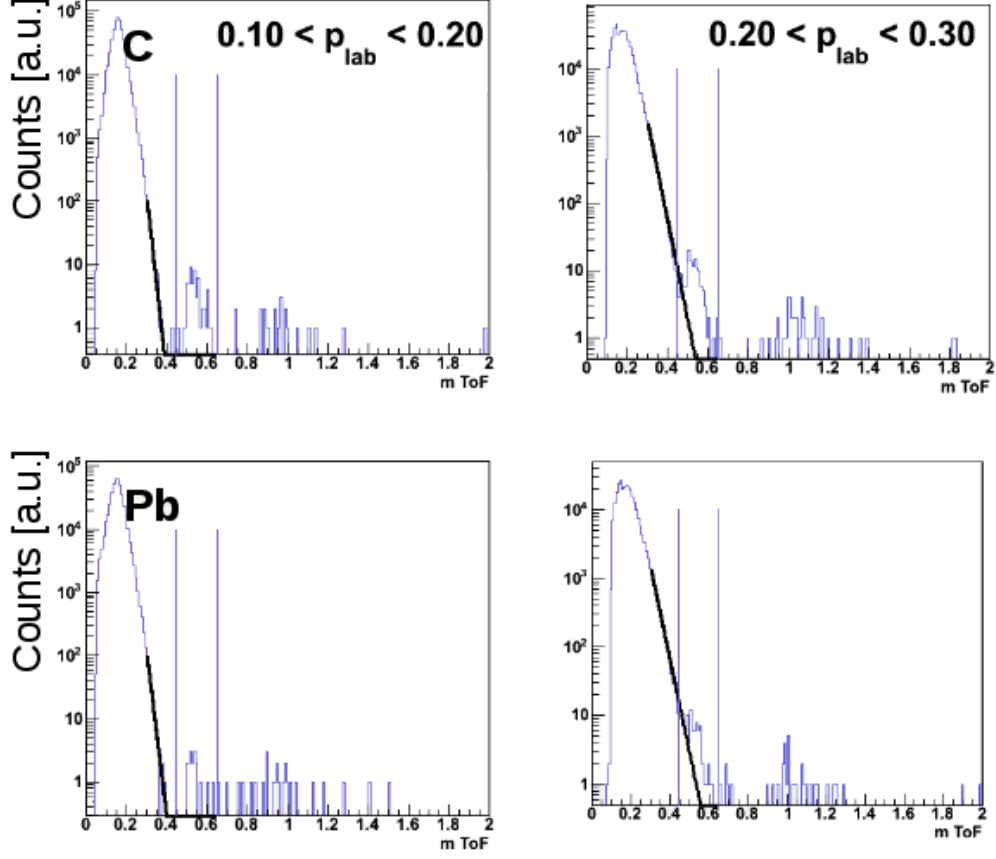


Figure 5.5: Mass distribution of negatively charged particles, measured by the CDC in the two lowest momentum bins: $p_{lab} = [0.1 - 0.2]$ GeV/ c (left column) and $[0.2 - 0.3]$ GeV/ c (right column). The upper row shows the spectra from the carbon target, the lower row from the lead target. K^- mesons candidates are identified within a mass range around the nominal kaon mass, depicted by the vertical lines. The black lines indicated the background contribution from the negatively charged pions. Note: Here no CDC - ToF matching was requested.

interpreted as tails of the pion and protons distributions (left panel), here referred to as ‘best case’. In this scenario, the kaon signal is determined as everything within the mass window (red lines) which is not covered by the extrapolation of the pion and proton distributions (black lines). In the ‘worst case’ scenario (right panel) only the explicit Gaussian-like peak is considered to be the signal and the remaining fraction is classified as background.

Both description methods were compared by the remaining fraction of kaon candidates, in a given momentum bin, between the lead and carbon targets. The ratios stay the same, within statistical uncertainty, for both scenarios. Therefore, the kinematic comparison of the production in differently sized targets remains indifferent to the back-

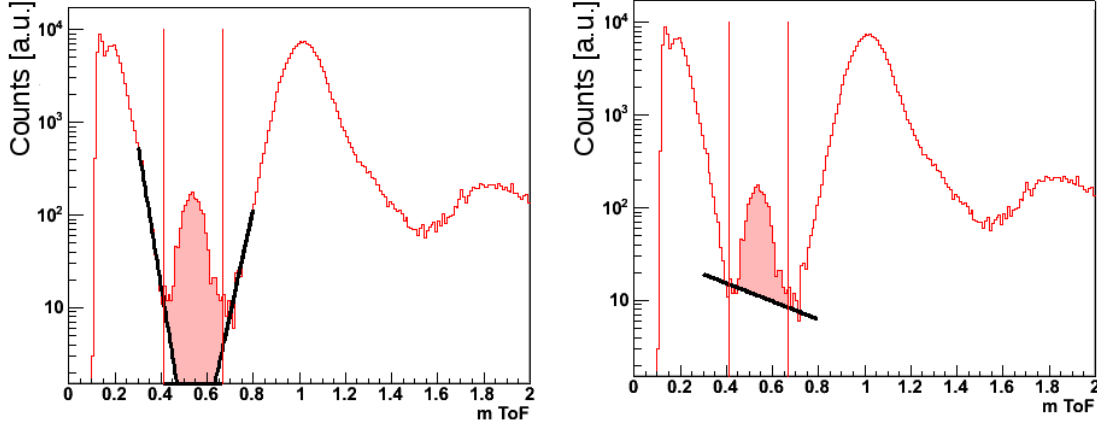


Figure 5.6: Mass spectrum of positively charged particles, reconstructed in the momentum range: $p_{lab} = [0.24-0.29]$ GeV/ c with the CDC sub-detector. No CDC - ToF matching was demanded. Left and right panel demonstrate the different background description methods: The ‘worst case’ (right panel) and the ‘best case’ scenario (left panel). See text for details.

ground description method. In the following analysis the ‘best case’ method is used. The difference of the described background determination methods is small enough to be accounted for by the statistical errors. Mass spectra in all momentum bins of the CDC analysis are compiled in Appendix B.

The total number of kaon candidates (background excluded) is summarised in the Table 5.2. The ‘ S/B ’ characterise the lower limit of the signal-to-background ratio, i.e. the signal fraction in the momentum bin with a highest contamination by the background.

		K^+	K^-
C	p_{max}	1.0 GeV/ c	0.5 GeV/ c
	S/B	> 4.7	> 3.4
	N_K	~ 8700	~ 390
Pb	p_{max}	1.0 GeV/ c	0.5 GeV/ c
	S/B	> 2.55	> 1.44
	N_K	~ 9620	~ 202

Table 5.2: Properties of identified K mesons. p_{max} : maximal momentum for kaon identification; S/B : signal-to-background ratio in the momentum bin with the largest contamination; N_K : Number of identified kaon-candidates (corresponding background is subtracted).

The phase space distribution, obtained by the combined CDC - ToF analysis is shown in Fig. 5.7 for the carbon (upper row) and lead (lower row) targets. K^- candidates are almost exclusively reconstructed in the RPC acceptance ($33^\circ < \theta_{lab} < 58^\circ$). The largest amount of K^+ candidates originate from the RPC sub-detector as well. The

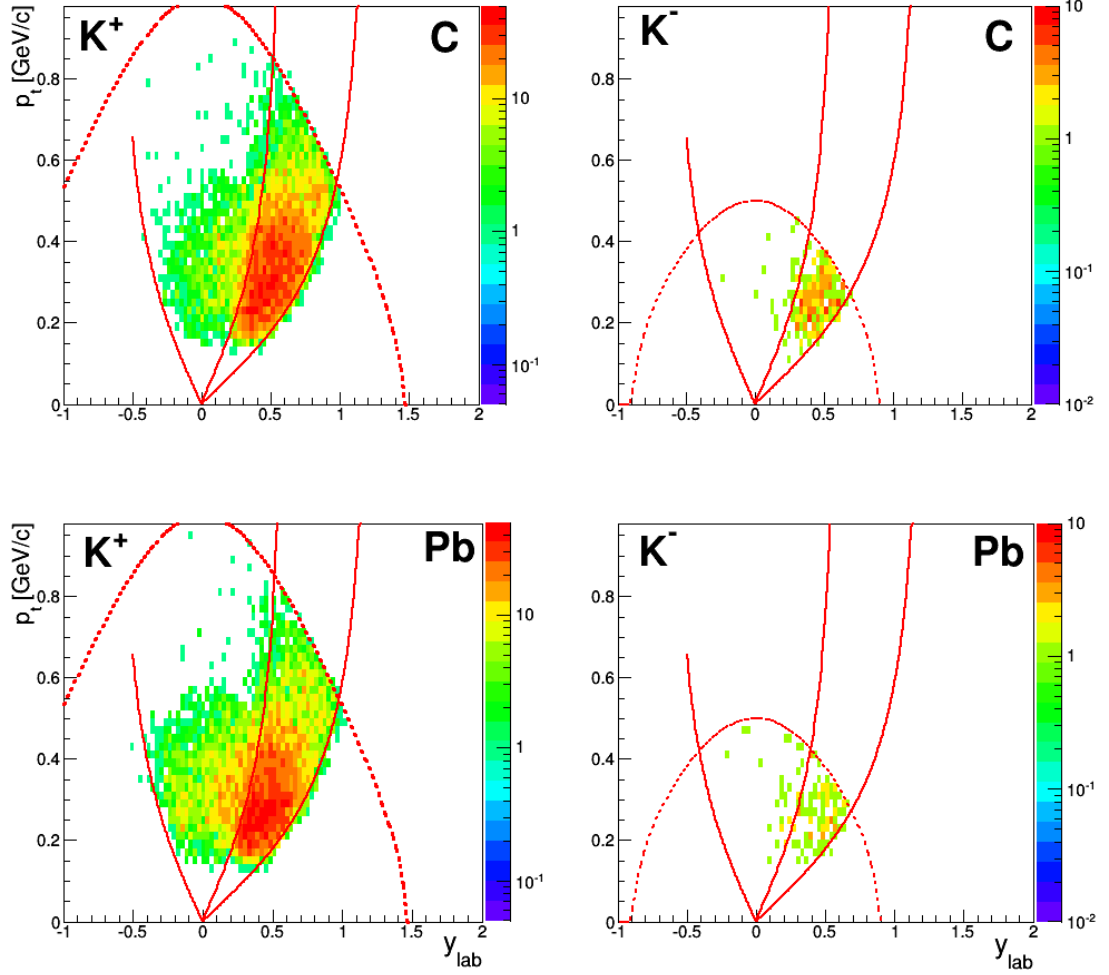


Figure 5.7: Phase space distribution of charged K mesons in terms of transverse momentum, p_t , and the laboratory rapidity. The upper row shows the measurement in $\pi^- + C$ reactions, results in the lower row are obtained in $\pi^- + Pb$ reactions. The solid lines correspond to the geometrical restriction of the detector, i.e. $\theta_{lab} = 33^\circ, 58^\circ, 123^\circ$. The dashed lines denote the upper momentum limit for the kaon identification, i.e. $p_{lab} = 1.0$ GeV/ c for K^+ mesons and $p_{lab} = 0.5$ GeV/ c for K^- mesons.

unambiguous identification is possible up to $p_{lab} = 1.0$ GeV/ c (dashed lines in the left panels). In the BAR sub-detector ($\theta_{lab} > 58^\circ$) nearly no K^+ candidates are observed beyond $p_{lab} \sim 0.5$ GeV/ c .

To compare the phase space distributions quantitatively in both targets, the momentum distributions of kaon candidates identified in reactions with the lead target is divided by the analogous distribution from the carbon target. Both are integrated over

the full rapidity range and normalised to the number of identified events⁴. The resulting ‘ratio’ is shown in Fig. 5.8 for K^+ (left panel) and K^- mesons (right panel).

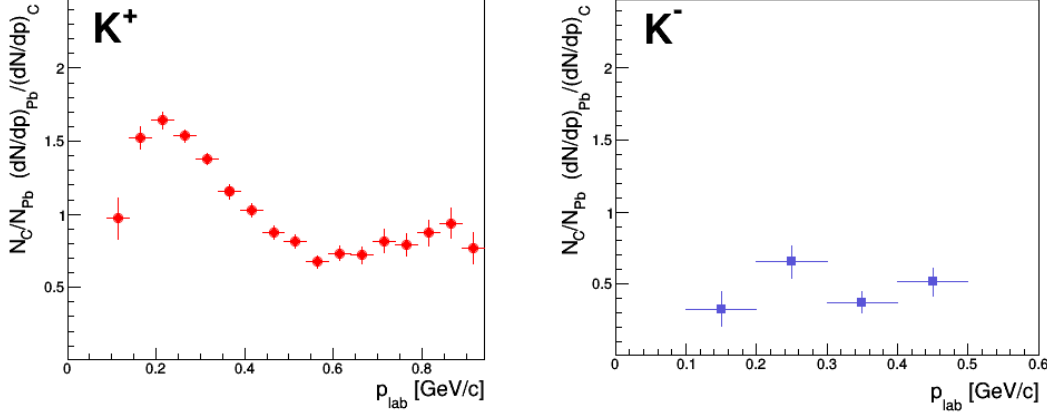


Figure 5.8: Ratio of the momentum distribution of kaons measured in a heavy and light targets. K^+ mesons (left panel) and K^- mesons (right panel). The distributions are normalised to the number of evaluated events from the corresponding target. The error bars reflect the statistical uncertainties.

The momentum ratio of K^+ mesons undergoes a maximum around $p_{lab} = 0.23$ GeV/c and becomes nearly constant for $p_{lab} > 0.5$ GeV/c. This characteristic behaviour can be explained by the influence of the nuclear medium. In the heavy target nucleus the K^+ mesons are repelled in the mean field, created by the large amount of nucleons, due to the strong interaction (see discussion in Chapter 2) and by the protons due to the electro-magnetic repulsion. Through both effects K^+ mesons gain additional momentum and therefore, the momentum distribution is ‘shifted’ to larger momenta, compared to a reference system from the carbon target.

The momentum ratio of K^- mesons is, within statistical uncertainties, constant. A possible interpretation is a large contribution of inelastic processes. The produced K^- mesons are reabsorbed and the candidates observed in the final state are created at the surface of the target nuclei. K^- candidates of that kind are not exposed to the influence of the nuclear medium.

The interpretation of the observed behaviour by comparison to transport model calculations is discussed in the last section of this chapter.

5.3 Reconstruction of Neutral Particles

The FOPI detector system can directly identify only electrically charged particles. Neutral particles are reconstructed through their decay products. In the following analysis three neutral particles are evaluated:

The ϕ meson. It decays after a mean lifetime of $\tau = 1.55 \cdot 10^{-22}$ s ($c\tau \approx 46.5$ fm) mainly

⁴See Section 3.5 for numeric values.

into:

$$\phi(1020) \rightarrow \begin{cases} K^+ K^- & \text{B.R.} = 48.9\% \\ K_S^0 K_L^0 & \text{B.R.} = 34.2\%. \end{cases}$$

The K_S^0 meson. It decays weakly after $\tau = 8.95 \cdot 10^{-11}$ s ($c\tau \approx 2.68$ cm) mainly into two pions:

$$K_S^0 \rightarrow \begin{cases} \pi^+ \pi^- & \text{B.R.} = 69.2\% \\ \pi^0 \pi^0 & \text{B.R.} = 30.7\%, \end{cases}$$

and the Λ baryon, decaying after $\tau = 2.63 \cdot 10^{-10}$ s ($c\tau \approx 7.89$ cm) into:

$$\Lambda \rightarrow \begin{cases} p \pi^- & \text{B.R.} = 63.9\% \\ n \pi^0 & \text{B.R.} = 35.8\%. \end{cases}$$

All values are taken from [PDG].

The listed particles are reconstructed from the channels with only charged decay products in the final state (fortunately these are also the channels with the largest branching ratio (B.R.)). The secondary vertex, i.e. the decay vertex of the neutral particle, is reconstructed from the intersection of the circular paths of the decay products in the transverse plane. Topological requirements are imposed on the intersection condition in the transverse and longitudinal plane. In the transverse plane the maximal deviation of the azimuthal angle is characterised by $\Delta\phi = |\phi_1 - \phi_2|$, and along the beam direction by $\Delta z = |z_1 - z_2|$. The indices ‘1’ and ‘2’ refer to the first and second decay product. Furthermore, restrictions are placed on the transverse distance between the primary and secondary vertices, referred to as r_S and its azimuthal inclination ϕ_S .

In the following the topological conditions, as used for the secondary particles selection in the analysis, are summarised. For definition of the quantities see Section 3.3.

ϕ meson \rightarrow	K^+ meson	K^- meson
	$hmul > 30.$	$hmul > 30.$
	$p_{lab} < 1.0 \text{ GeV}/c$	$p_{lab} < 0.5 \text{ GeV}/c$
	$ m_{CDC} - 0.5 < 0.12$	$ m_{CDC} - 0.5 < 0.12$
	$ m_{ToF} - 0.5 < 0.1$	$ m_{ToF} - 0.5 < 0.11$

Table 5.3: Selection criteria imposed on the charged kaons for the reconstruction of the ϕ meson. The values are motivated by the analysis in the previous section. Note that no secondary vertex is reconstructed due to the short lifetime of the ϕ meson.

5.3.1 Combinatorial Background

Using the conditions, describes above, the invariant mass of the mother particle can be calculated from the kinematic properties of the selected daughter particles. The

K_S^0 meson \rightarrow	π^+ meson	π^- meson
	$hmul > 20.$	$hmul > 20.$
	$0.5 < d_0 < 30. \text{ cm}$	$0.5 < d_0 < 30. \text{ cm}$
	$ m_{CDC} - 0.138 < 0.5$	$ m_{CDC} - 0.138 < 0.5$
Secondary vertex:	$\Delta\phi < 20.^\circ;$	$\Delta z < 30. \text{ cm};$
	$0.5 < r_S < 15. \text{ cm}$	

Table 5.4: Selection criteria, as used for the preselection of K_S^0 candidates. Influence of stricter topological restrictions is investigated in the K_S^0 analysis section.

Λ baryon \rightarrow	π^- meson	proton
	$hmul > 30.$	$hmul > 30.$
	$3. < d_0 < 30. \text{ cm}$	$d_0 > 0. \text{ cm}$
	$p_t > 0.05 \text{ GeV}/c$	$p_t > 0.05 \text{ GeV}/c$
	$ m_{CDC} - 0.138 < 0.5$	$ m_{CDC} - 0.938 < 0.3$
Secondary vertex:	$\Delta\phi < 30.^\circ;$	$\Delta z < 18. \text{ cm};$
	$1. < r_S < 30. \text{ cm}$	

Table 5.5: Reconstruction conditions for the preselection of Λ baryon candidates.

spectrum of invariant masses exhibit an excess around the nominal mass of the mother particle. Usually the signal in the invariant mass spectrum is superimposed by the background (characteristic example is Fig. 5.15), the so-called *combinatorial background*.

There are several methods to describe the combinatorial background. A straight forward approach is to fit the distribution with a polynomial function. For this purpose a clearly pronounced peak is required. Furthermore, no insight into the background contribution in the kinematic quantities (e.g. momentum) of the signal candidates can be retrieved. More sophisticated procedures aim at breaking the correlation of the decay products by e.g. rotating the track of one daughter particle with respect to the primary vertex. The resulting daughter pairs are uncorrelated and therefore purely background. Another method is to combine ‘like-sign pair’, i.e. not a positive and a negative track, but two positive or two negative tracks.

In the present analysis the background distribution is estimated by the so-called *event-mixing method*. Hereby the correlation is broken by choosing the daughter tracks from different events. The signals reconstructed this way can not originate from a single particle decay and therefore is representative for a background signature. The obtained background distribution describes the observed contamination fairly well for events samples with reasonable statistics, as will be demonstrated in the upcoming sections.

5.4 The ϕ mesons

The ϕ meson is a so - called hidden strangeness state, it is composed of a $s\bar{s}$ pair of quarks. The mass distribution exhibits a Bright - Wigner shape, centred around $m_\phi = 1019.5$ MeV/ c^2 , with a decay width in vacuum of $\Gamma = 4.27$ MeV [PDG]. The production is strongly suppressed according to the Okubo - Zweig - Iizuka selection rule. Nevertheless the estimated production rates in the given experiment were calculated to be reasonably high.

In the considered reactions, the ϕ mesons are produced in $\pi^- + p \rightarrow n + \phi$ processes. The threshold pion momentum for this reaction is $p_\pi = 1.56$ GeV/ c . The production close to the threshold energies ensures that the resulting ϕ mesons entrain only little momentum and, therefore, have a decent probability to decay inside the nucleus⁵. Hadronic models predicted an in - medium life time of $\tau < 5$ fm/ c [Kli98]. On one hand this circumstance makes the properties of the ϕ meson sensitiv to the medium. On the other hand, the ϕ meson candidates observed in the final state are influenced by the in - medium behaviour of its decay products, i.e. the K^+ and K^- mesons.

The invariant mass spectra of correlated $K^+ + K^-$ meson signals, under condition as discussed above, are depicted in Fig. 5.9 for the investigated targets. A clear excess at nominal ϕ meson mass is visible in all three measurements. The measured signal is nearly free of background. The blue symbol represent the attempt to estimate the combinatorial background with the event - mixing method.

The amount of reconstructed ϕ meson candidates is summarised in Table 5.6. Hereby the analysis is done separately for each trigger condition in order to facilitate an unambiguous allocation to a triggered cross section. The determination and listing of trigger cross sections can be found in Section 3.5.

Trigger ID	N_ϕ in C - Tar:	N_ϕ in Cu - Tar:	N_ϕ in Pb - Tar:
all	13	5	9
T10	—	—	—
T11	—	—	—
T12	9	2	5
T13	12	5	9
T14	5	—	3
T15	—	—	—

Table 5.6: The amount of reconstructed ϕ meson candidates in every target, sorted by the trigger condition. The trigger ID ‘all’ represent the most complete available data set. Definition on individual trigger IDs can be found in Section 3.5. The values are rounded to integer numbers, therefore the uncertainty is given by $\Delta N_\phi \sim 1$.

The observed number of ϕ mesons is compatible with the production rate estimate in the beam time proposal. Note that the number of events, in order to facilitate

⁵Explicit discussion of vector mesons in nuclear medium can be found in Chapter 2.

the analysis of a ‘transparency ratio’, could not be recorded due to not reaching the anticipated beam intensity and difficulties with the alignment of the pion production target .

The kinematic properties of ϕ candidates are characterised by their localisation in the phase space. Fig. 5.10 depict the transverse momentum - rapidity plane. Nearly all ϕ signals are reconstructed by the RPC sub - detector. It is not surprising, since also nearly all K^- mesons in this experiment are measured by the RPC. See Fig. 5.7. Noteworthy are the transverse momenta of the ϕ candidates. None of the reconstructed mesons is slower than $p_t \sim 400$ MeV/c. It might be an indication of in-medium absorption of slow decay products of the ϕ meson.

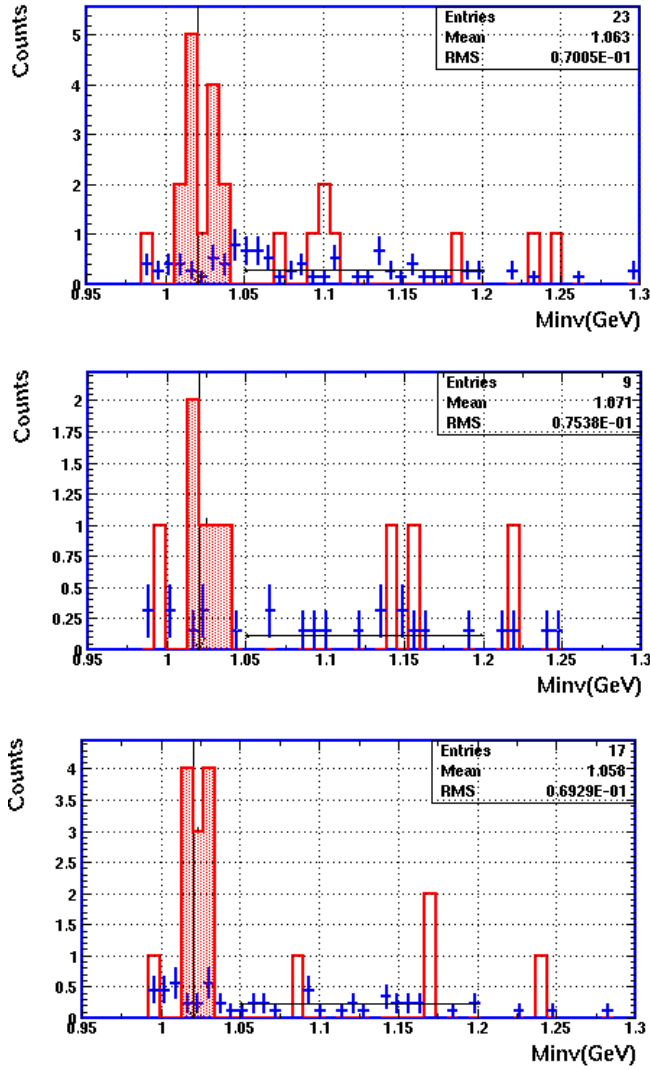


Figure 5.9: Invariant mass distribution of K^+K^- pairs, obtained in C (left panel), Cu (middle) and Pb (right panel) targets. The excess around the nominal ϕ meson mass (red-shaded area) is interpreted as the ϕ signal. Blue symbols represent the mixed-event background. Black horizontal lines denote the alignment region for the background description.

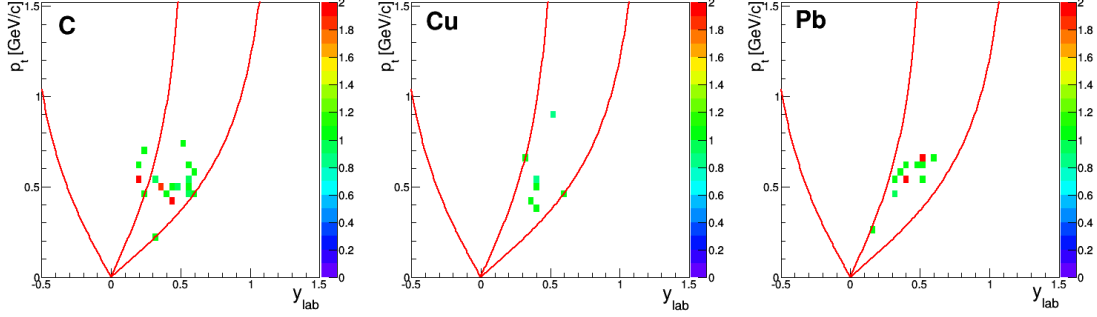


Figure 5.10: Localisation of ϕ meson candidates in the phase space, measured in different targets. Red lines denote the geometrical limitation of the BAR and RPC sub-detectors.

5.4.1 Reconstruction Efficiency

In order to compare the measurements in diverse reactions, i.e. in differently sized targets, the reconstruction efficiency of the FOPI detector needs to be investigated for a possible reaction dependance.

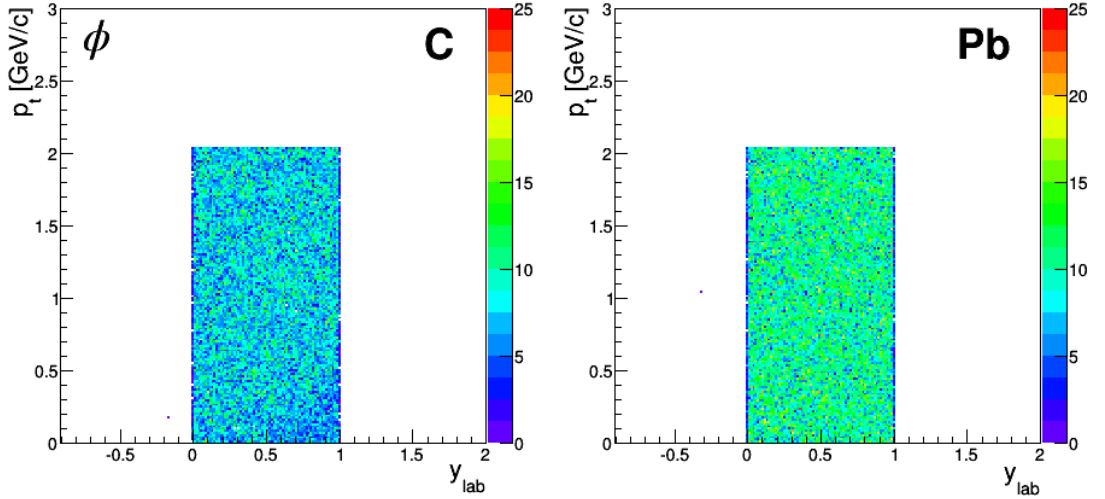


Figure 5.11: The input ϕ meson phase space distribution to the MC simulations of the carbon (left panel) and lead (right panel) targets.

For an accurate efficiency estimation a realistic phase space distribution of ϕ mesons is propagated through a detector simulation. For the simulation of heavy-ion collisions the input ϕ mesons are emitted from the thermal source according to the Boltzmann distribution. In pion-induced reactions, the Boltzmann-like ansatz is probably not valid. A priori, a homogenous $p_t - y_{lab}$ distribution is a good approximation. The obtained mesons are embedded into a IQMD event and demanded to decay into specified

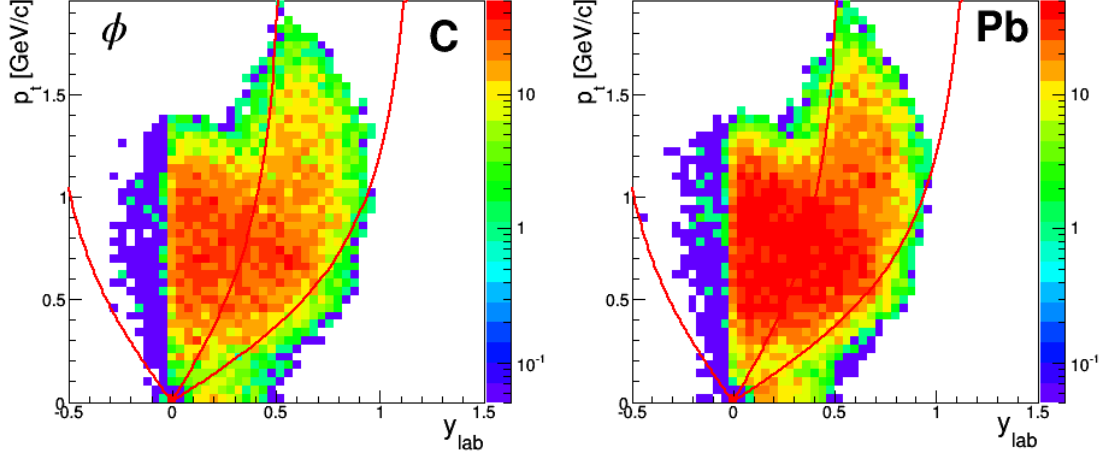


Figure 5.12: Result of the Geant simulations: The final state ϕ meson phase space distribution, reconstructed after the propagation and decay in the simulated detector.

decay channels. The IQMD calculation, on their part, reproduce the dynamic behaviour of nucleons. The produced event sample is propagated through the Monte Carlo (MC) based simulation of the FOPI detector – Geant. The Geant environment reproduces the geometrical configuration of the detector, as well as the material composition, resolution effects and all relevant processes like ionisation, scattering, hadronic interactions and particle decay.

From the resulting data set, the ϕ meson can be reconstructed in the same way as from the experimental data. The comparison of the input ϕ phase space distribution and the corresponding phase space distribution in the final state reveals the effects of the propagation through the detector and the influence of the reconstruction procedure, i.e. the *reconstruction efficiency*.

In order to create a realistic input distribution, the kinematic properties of the simulated and the experimental ϕ mesons have to be adjusted. In the present experiment the number of available ϕ candidates is too low to enable a reasonable adjustment, therefore a different approach was pursued. The input phase space distribution was parameterised as a constantly populated interval in transverse momentum and rapidity. The parametrisation is depicted in Fig. 5.11. After the full detector simulation and reconstruction of ϕ candidates from the K^+K^- correlation under the experimental conditions, the final state distribution of ϕ mesons in Fig. 5.12 is retrieved.

An estimate of the reconstruction efficiency is obtained by comparing the number of initial ϕ mesons (N_{KINE}) to the amount of the reconstructed ones (N_{MC}) in each phase space cell:

$$\varepsilon^{ij} = \frac{N_{MC}^{ij}}{N_{KINE}^{ij}},$$

with $i \in [p_t \text{ MIN}, p_t \text{ MAX}]$ and $j \in [y_{lab} \text{ MIN}, y_{lab} \text{ MAX}]$.

For this purpose the phase space is divided in four rapidity bins and four transverse momentum intervals. The resulting fractions, ε^{ij} , are shown in Fig. 5.13. The obtained efficiency coefficient for the evaluation of the carbon target are symbolised by the black triangles and the corresponding analysis in the lead target, by the red triangles. The reconstruction ability is lowest for the small transverse momenta and becomes more efficient with increasing momentum. The reconstruction efficiency is slightly higher in the lead (ε_{Pb}) than in the carbon target (ε_C).

To compare both reconstruction capabilities quantitatively, the efficiency coefficients are integrated over the full rapidity range and presented as the ratio: $\varepsilon_{Pb}/\varepsilon_C$ in Fig. 5.14. The ratio is independent of momentum and close to unity. For the following analysis it is concluded that the reconstruction efficiency in the lead and carbon targets is nearly the same.

5.4.2 The Transparency Ratio

Possible in-medium effects can be investigated in the so-called attenuation measurements. The typically reconstructed quantity is the nuclear *transparency ratio* T_A :

$$T_A = \frac{\sigma_{\pi^- A \rightarrow \phi X}}{A \sigma_{\pi^- N \rightarrow \phi X}}. \quad (5.1)$$

The ratio compares the ϕ production cross section in a nucleus of the size A per nucleon with the production in reactions with a free nucleon.

In pion induced reactions at the considered energy no ϕ production in reaction $\pi^- + n$ is possible. The relevant quantity for the ϕ meson production is the number of protons in a nucleus. The transparency ratio is modified into T_Z :

$$T_Z = \frac{\sigma_{\pi^- A \rightarrow \phi X}}{Z^\alpha \sigma_{\pi^- p \rightarrow \phi X}} \quad (5.2)$$

Hereby, the elementary cross section is assumed to scale with the powers of the charge number Z . The transparency ratio T_Z is expected to decrease with increasing charge number, partially due to the rescattering of the decay products and partially due to the broadening of the ϕ spectral function in nuclear medium. BUU transport simulations of ϕ cross sections from photo-production predict a $T_A \sim 0.95$ for a carbon sized nucleus and a reduction to $T_A \sim 0.87$ for a heavy target like lead [Mueh06].

The experimentally measured cross section can be calculated from the number of observed ϕ mesons (N_ϕ). The quantity N_ϕ needs to be corrected for the reconstruction efficiency in order to account for the losses through the reconstruction procedure and limited detector acceptance, and for the trigger efficiency to upscale the yield from the selected fraction of events to the totally possible number of reactions. Furthermore, the branching ratio for the evaluated decay channel has to be taken into account.

As discussed above, the available data sample does not allow for a realistic efficiency evaluation, therefore the full production cross section of ϕ mesons can not be reconstructed. Nevertheless, since the estimate of the reconstruction efficiency (ε_{Reco}) in the carbon and lead targets was found to be very similar, the production yields from the

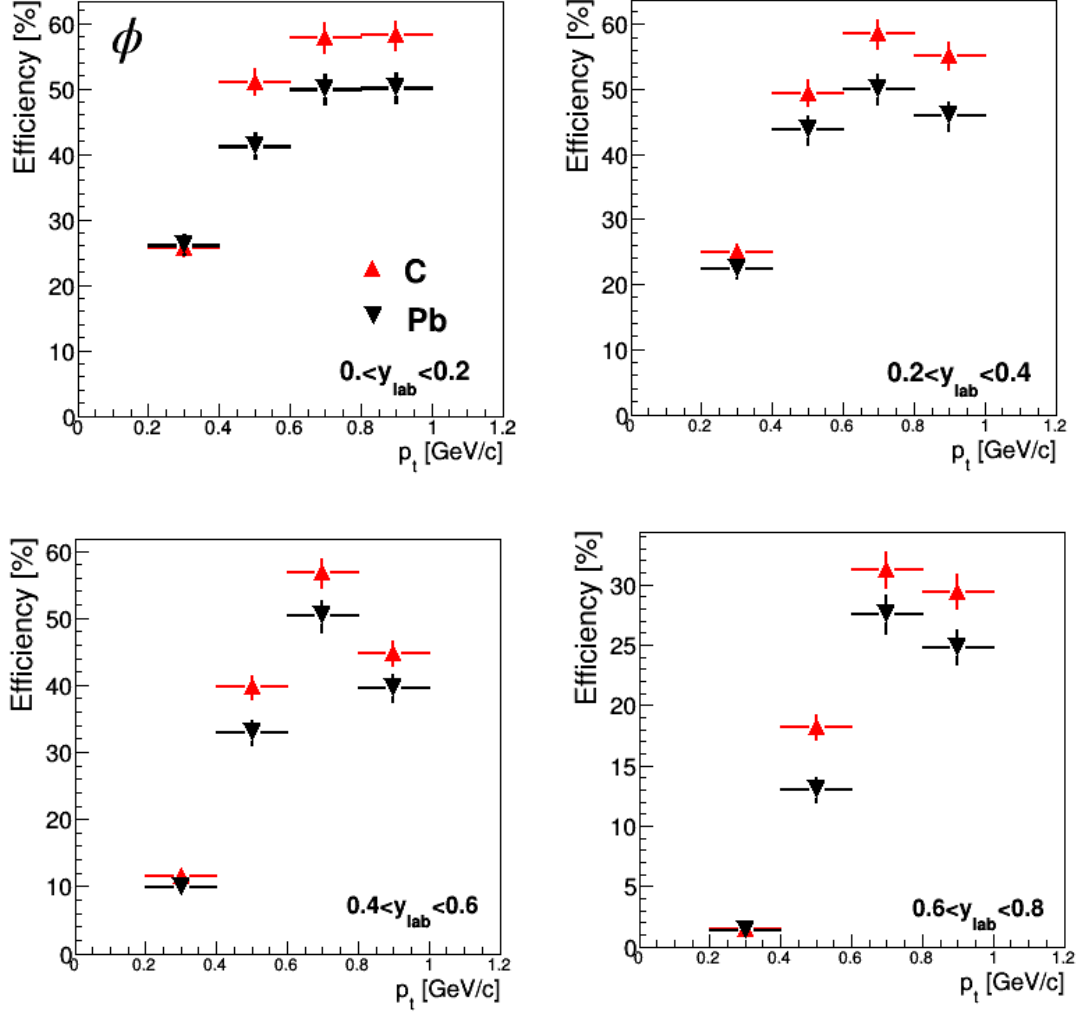


Figure 5.13: Reconstruction efficiency of the ϕ meson in different phase space cells for the carbon and lead targets.

light and heavy targets can be compared to each other. The measured cross section fraction, σ_{ϕ}^{meas} , can be calculated by

$$\sigma_{\phi}^{meas} = \sigma_R \cdot \frac{N_{\phi}}{N_{events}} * \epsilon_{Reco}. \quad (5.3)$$

Inspection of the Table 5.6 reveals that all events, containing a ϕ candidate, fulfil the trigger condition ‘T13’. Therefore, the reaction cross section (σ_R) can be associated with the cross section triggered by the trigger bit ‘T13’⁶.

⁶The triggered cross sections are calculated in Section 3.5.

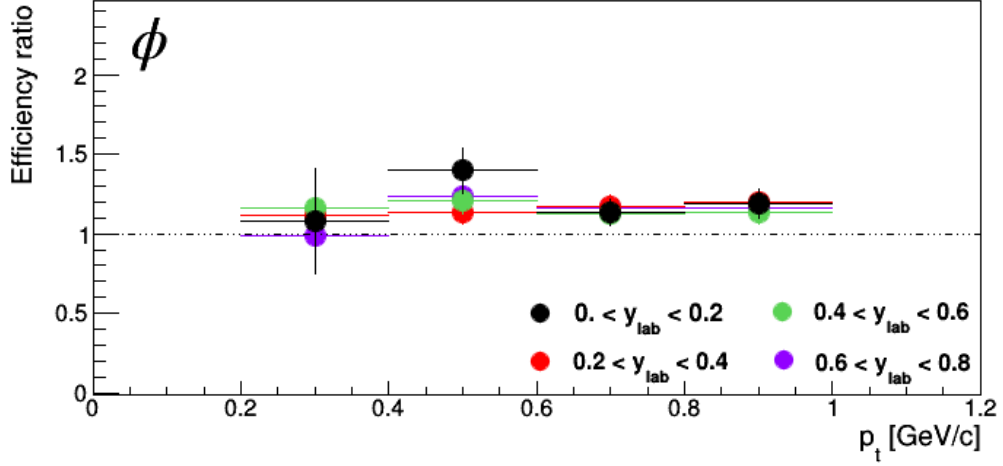


Figure 5.14: Reconstruction efficiency of the ϕ meson as a function of transverse momentum, integrated over the full rapidity range. Depicted is the ratio of the obtained values for lead over the carbon target.

Target	σ_R [mb]	N_{events}	N_ϕ	$\sigma_\phi^{meas}/\varepsilon_{Reco}$ [μb]
C	29.57 ± 1.37	1 166 559	12 ± 1	0.304 ± 0.026
Pb	225.85 ± 10.58	1 266 545	9 ± 1	1.608 ± 0.184

Table 5.7: Relevant quantities for the calculation of the measured cross section. See text for details.

In Table 5.7 the adopted values are summarised. N_{events} denotes the number of events accepted by the trigger logic. Note that the triggered cross sections from Section 3.5 and the number of events are reduced by subtracting the background contribution. The background is caused by non-target events. The contribution is estimated as the fraction of events without a valid vertex position. About 46 % of carbon events and 43 % of reactions with the lead target are rejected for the considered trigger selection.

Assuming equal reconstruction and trigger efficiency for the carbon and lead targets the production cross section measured in lead is about 5.3 times higher than the one in the carbon nucleus. In the hypothesis of Z^α scaling of the production cross section, the observed ratio corresponds to $\alpha \sim 0.63$. The obtained α value supports the assumption of ϕ production on the surface of the nucleus. The production cross section scales with the size of the surface, i.e. $Z^{2/3}$.

5.5 The Λ Baryons

At SIS-18 energies Λ baryons are produced by associated production with kaons. The reaction channel $\pi^- + p \rightarrow \Lambda K^0$ has the smallest threshold energy for strangeness production in pion induced reactions and was observed to have a relatively large reac-

	C - target	Cu - target	Pb - target
Signal	10 716	6 267	13 733
S/B	1.059	1.064	1.239
Sign	74.26	56.84	87.17
Mass [GeV/ c^2]	1.117	1.117	1.117
Width [MeV]	3.65	3.59	3.59

Table 5.8: Properties of reconstructed Λ baryons. The listed quantities are: ‘Signal’ – the Λ signature without background, ‘ S/B ’ – the signal- to- background ratio, ‘Sign’ = $S/\sqrt{S+B}$ – the significance of the Λ signal, ‘Mass’ – the mean value of the gaussian fit and ‘Width’ – the standard deviation of the gaussian fit.

tion cross section of $\sigma = 0.2$ mb. It is the most favoured production mechanism for strangeness close to threshold energies. Investigation of Λ baryon production promotes the understanding of associated strangeness production.

In the following section the reconstruction of Λ candidates in reactions with differently sized targets is examined and compared by the means of kinematic variables. Special emphases is put on the background contribution to the observed spectra. The reconstruction procedure is described in Section 5.3. The selection parameter for the reconstruction of Λ candidates are summarised in Table 5.5.

Fig. 5.15 shows the invariant mass spectra of $p-\pi^-$ pairs, which fulfil the correlation requirements, in the evaluated targets. The red histograms are obtained by the correlation of protons and pions from the same events, i.e. with Λ decay as a possible origin. A clear excess, centred around the nominal Λ baryon mass of $m_\Lambda = 1115.683 \pm 0.006$ MeV/ c^2 is present in the spectra from all targets. The observed mass spectra are afflicted by the background. The non- Λ contribution is estimated by the so- called mixed- event background method. Hereby not correlated $p-\pi^-$ pairs are created by imposing correlation conditions on pions and protons from different events. The obtained distribution is depicted by the blue histograms. In all three targets the mixed- event method reproduced the background distribution fairly well⁷.

The resulting background histogram can be subtracted from the original observation. The diminished invariant mass spectra are shown in the lower row of Fig. 5.15. The excess around the nominal Λ mass is fitted with the gaussian distribution (black curves). In Table 5.8 the parameter characterising the reconstructed Λ signal are listed. The mass region for the ‘signal’ determination is depicted by the red shaded area in Fig. 5.15. The signal- to- background ratio and the significance of the signal are evaluated by comparing the fraction of the red shaded area above and below the background histogram. The ‘Mass’ and ‘Width’ values are obtained from the gaussian fit.

The mean values of the fit in all three targets are reasonably close to the nominal Λ mass. The width of the mass distribution is slightly higher in the carbon measurements than in the remaining two targets. The observed Λ signal is about 30 % higher in the lead target than in the carbon, even though the number of evaluated events is nearly

⁷Note that the further analysis will reveal that this statement is not valid for the full kinematic range.

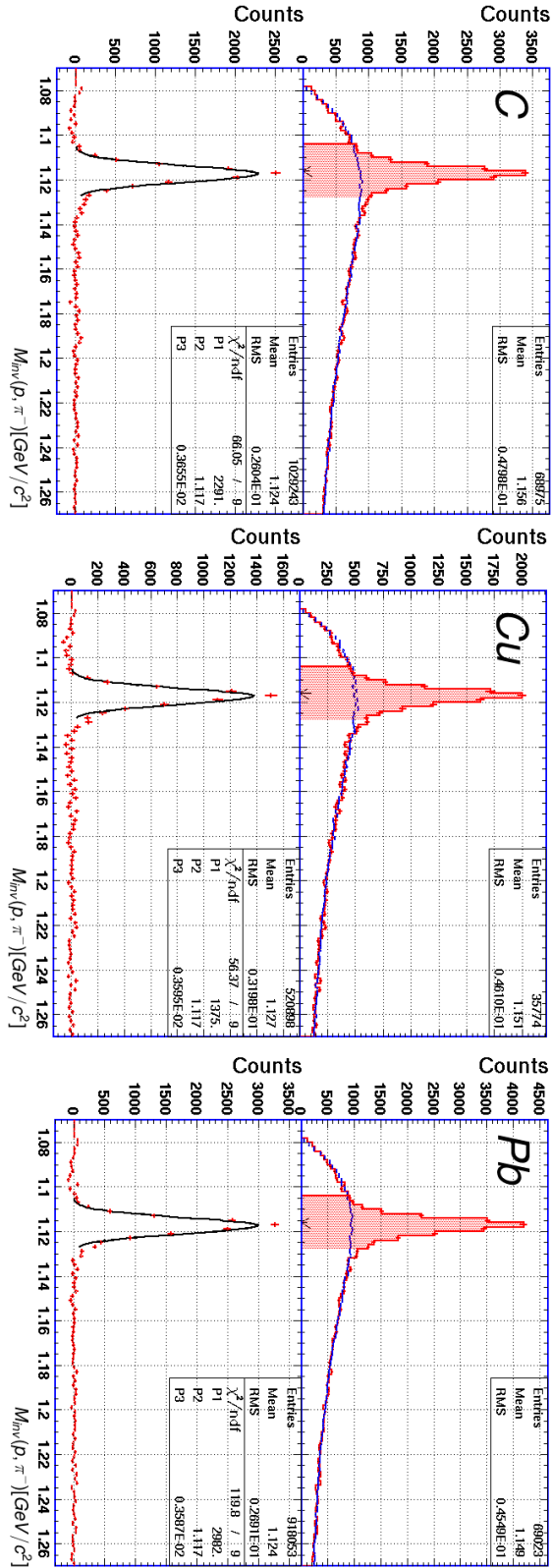


Figure 5.15: Upper row: The invariant mass distribution of correlated $p-\pi^-$ pairs reconstructed from reactions with carbon (left panel), copper (middle) and lead (right panel) targets. Blue histogram represents the combinatorial background, estimated by the mixed-event method. Red-shaded areas define the region of Λ baryon candidates. Lower row: Background-subtracted invariant mass spectrum. The black curves demonstrate the gaussian fit to the mass peak.

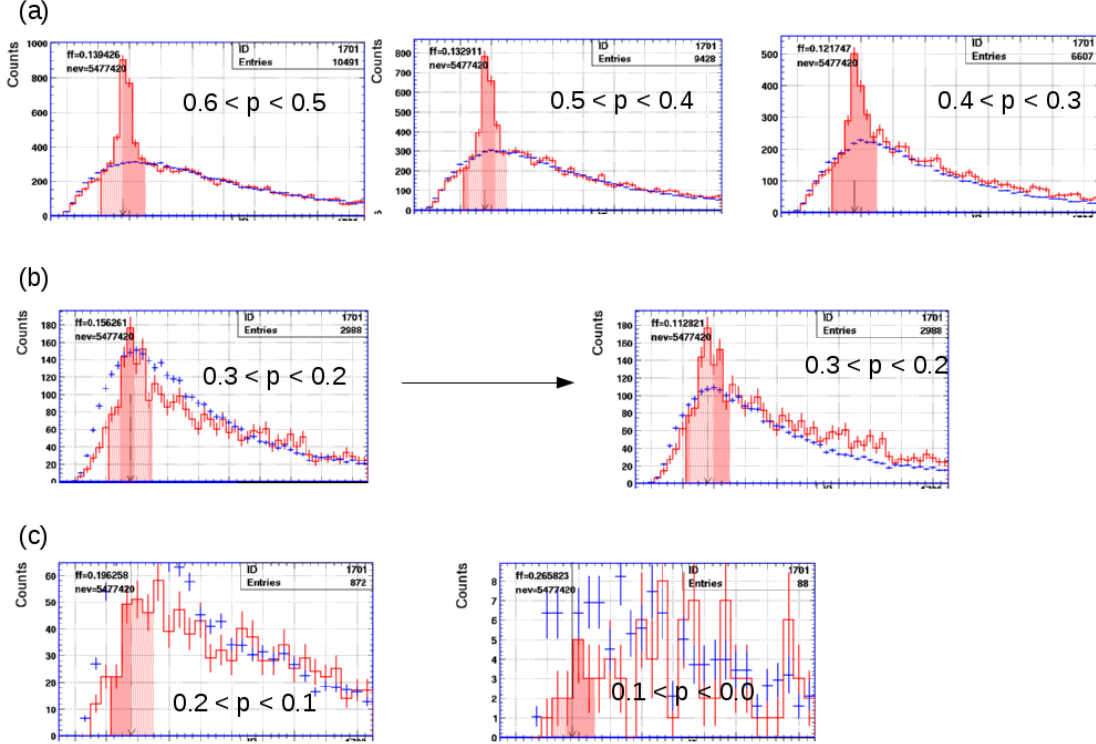


Figure 5.16: Invariant mass distribution of $p-\pi^-$ pairs in carbon target for various momentum selections. ‘ p ’ denotes the laboratory momentum. The unit of numerical values is GeV/c . For details see text.

equal for the both targets.

To examine the background contribution in more detail, the invariant mass spectra are reproduced in narrow momentum bins. In the phase space region with $p_{lab} > 0.3 \text{ GeV}/c$ the background is emulated reasonably well by the mixed event method. Panel (a) of Fig. 5.16 shows three representative examples. In lower momentum bins, e.g. $0.2 < p_{lab} < 0.3 \text{ GeV}/c$ (panel (b)), the general shape of the contamination is recreated, but normalisation adjustment are necessary in order to describe the background distribution. Below $p_{lab} = 0.2 \text{ GeV}/c$, see panel (c) of Fig. 5.16, no Λ candidates can be distinguished from the fluctuation of the background.

The background portions over the full dynamic range of Λ candidates are depicted in Fig. 5.17. The blue histograms portray the kinematic behaviour of Λ candidates reconstructed from all correlated pairs, i.e. it is contaminated by artificially correlated pairs. The red histograms are obtained by mixed event method and, therefore, contain purely background. Black histograms show the background diminished representation. The transverse momentum (left panel) and the laboratory momentum (right panel) distributions are overshadowed by the background in the very low momentum region, as discussed above. The rapidity dependence of the background (middle panel of Fig. 5.17) demonstrates that the backward rapidities are more affected by the contamination. The discussed behaviour is observed in all targets.

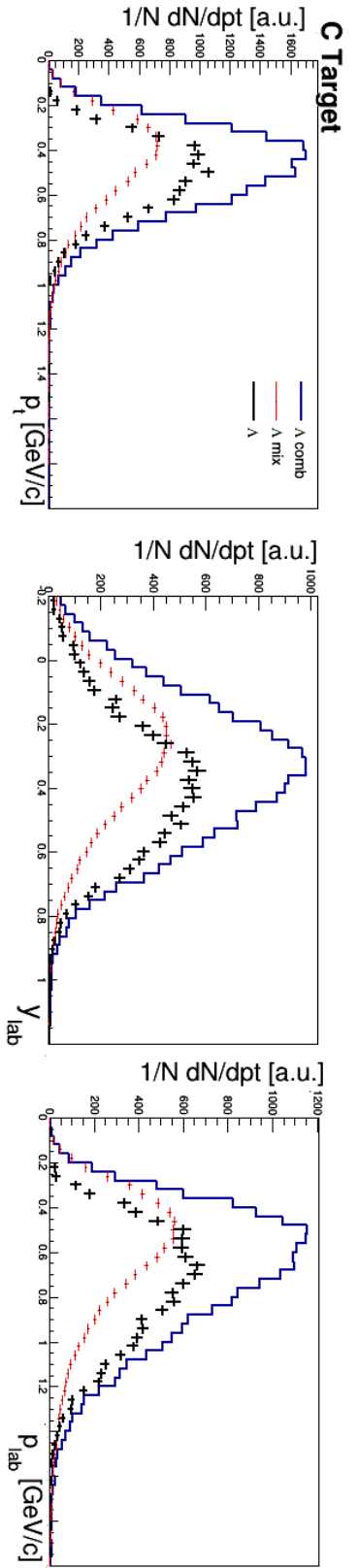


Figure 5.17: Background contribution to the kinematic variables. Blue histograms are obtained from correlated $p-\pi^-$ pairs, red histograms from not correlated $p-\pi^-$ pairs (taken from different events) and the black histograms are the difference between the two distributions.

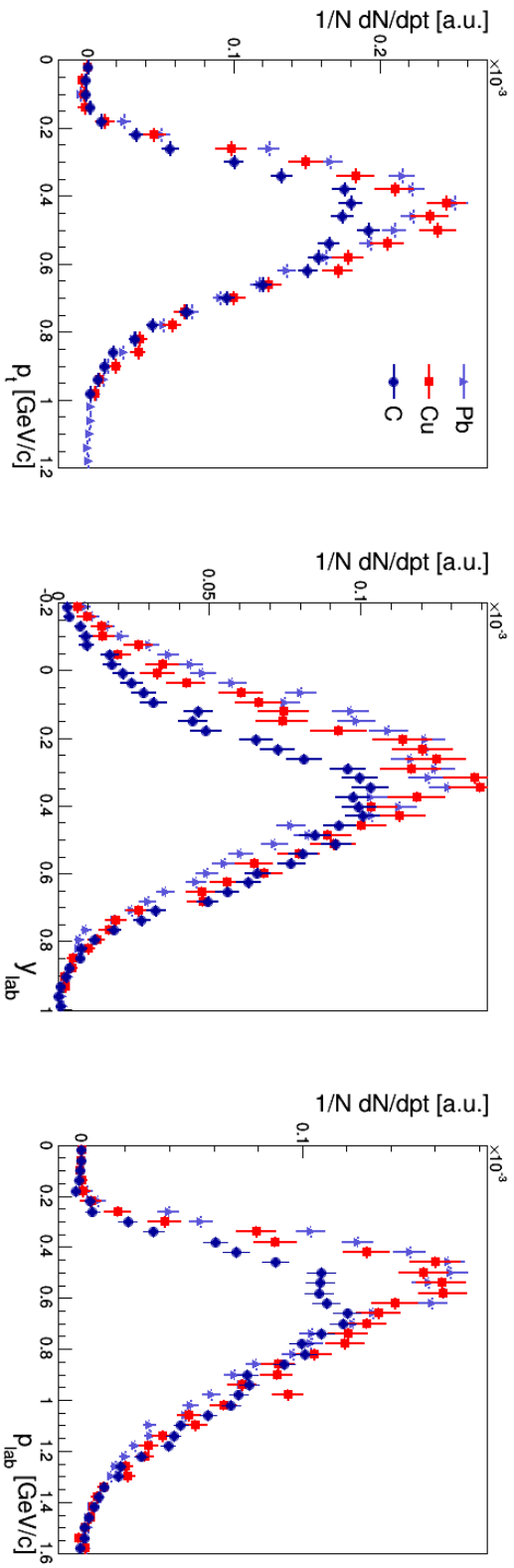


Figure 5.18: Distributions of kinematic variables for the Λ signal: Transverse momentum (left panel), laboratory rapidity (middle) and laboratory momentum (right panel). Measurements in different targets are represented by different symbols.

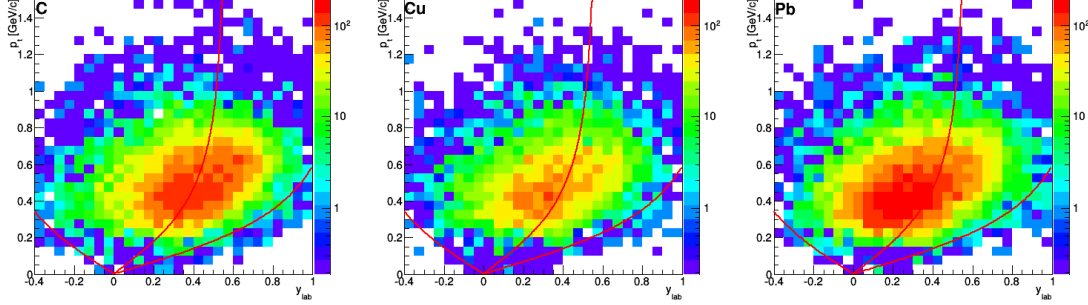


Figure 5.19: Phase space distribution of (background-subtracted) Λ candidates in terms of transverse momentum and rapidity in the laboratory system. Red curves depict the geometrical restriction of the several sub-detectors, i.e. $\Theta_{lab} = 33^\circ, 59^\circ, 126^\circ$.

The phase space distribution of the final Λ candidate selection is depicted in Fig. 5.19 in the plane spanned by the transverse momentum and laboratory rapidity. The red lines, as usual, denote the geometrical limitations of the RPC and BAR sub-detectors. The measurement of Λ candidates beyond the geometrical acceptance is possible if the decay products are detected within the detector acceptance. In contrast to previously discussed charged kaons and the ϕ meson, the phase space distribution is indifferent towards the RPC and BAR acceptance. To reconstruct the decay products of the Λ baryon, i.e. protons and pion the PID capabilities of the CDC are fully sufficient. Therefore, the Λ spectra are not influenced by the different resolution of RPC and BAR sub-detectors.

The kinematic influence of different targets is compared in Fig. 5.18 by the projections of the phase space distribution onto the transverse momentum axis (left panel), the rapidity axis (middle) and integration over the kinematic ellipses into laboratory momentum (right panel). In order to be tantamount, the histograms are normalised to the number of events recorded for the certain target. For ‘fast’ particles (upper half of the momentum and rapidity distributions) the kinematic behaviour is very similar in all three targets. The lower momentum and rapidity region are stronger populated in the heavier systems, i.e. lead and copper, possibly indicating a strong influence of the rescattering processes.

The momentum distributions obtained in carbon and lead targets are compared directly in Fig. 5.20 by constructing a ratio of lead to carbon. For momenta larger than $p_{lab} = 0.65$ GeV/c both distributions are equal, the ratio adapts a constant value. Toward smaller momenta the larger portion of slow Λ candidates manifest itself in the increasing ratio values. A priori, two mechanisms can be responsible for the reduced momentum values in a heavy target. On the one hand, the small mean free path of Λ baryons in nuclear matter promotes elastic and inelastic interaction with nucleons. Larger number of scattering partner in a heavy target causes a stronger population of the low momentum region. On the other hand, Λ baryons are expected to experience an attraction toward nucleons due to strong interaction, resulting in a similar effect

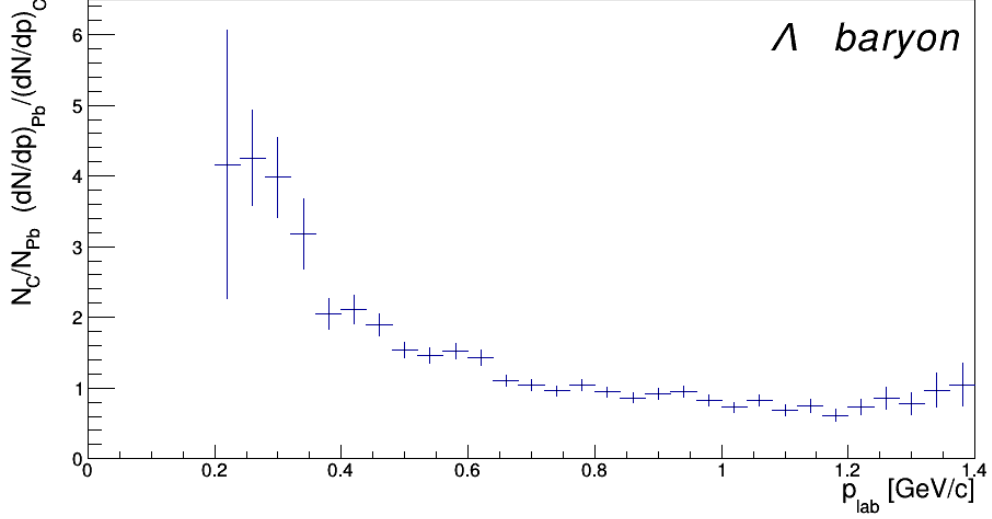


Figure 5.20: Momentum distribution of Λ baryons, obtained in the lead target per event, normalised to the corresponding distribution from the carbon target.

on the momentum distribution. In order to distinguish between the two contributions, realistic transport modelling is necessary. The effect of the strong interaction is mostly pronounced at small momenta. Due to a limited statistics the sensitive region, presumably, could not be reached in the presented analysis.

5.6 The K_S^0 meson

The K_S^0 meson⁸ is a particularly convenient candidate for the study of the KN potential. The mean free path of a slow ($p_{lab} \sim 100$ MeV/c) K^0 meson in normally dense nuclear matter is $\lambda \sim 5.3$ fm. This length is comparable to the diameter of a carbon nucleus and about one third of the lead nucleus' diameter. The K^0 mesons are likely to escape the dense region without suffering collisions of elastic or inelastic nature. Furthermore, due to its neutral electric charge it is not influenced by the electro-magnetic interaction. Its in-medium interaction is restricted solely to the strong interaction.

Under considered experimental conditions K^0 mesons can be produced in associated production with a hyperon or directly with a K^- meson and a proton. In the presented analysis the K^0 candidates are reconstructed from their dominant decay channel - the decay into two charged pions. The identification procedure and the background estimation method are described in Section 5.3. The topological criteria for the preselection of K^0 candidates are listed in Table 5.4.

The invariant mass spectra on $\pi^+ - \pi^-$ pairs, that fulfilling the correlation requirements, are displayed by the red histograms in Fig. 5.21 for the three evaluated targets.

⁸In the following section the notation " K^0 " and " K_S^0 " are used synonymously. The K_L^0 mesons are due to their large decay length of $c\tau = 15.3$ m not measurable with the FOPI spectrometer.

The mass spectra of K^0 mesons are superimposed by a spectrum of pion pairs which do not originate from a K^0 decay. This contribution is estimated by requiring correlation for pions from different events. The obtained background distribution is depicted by the blue histograms. The background contribution is highest in the carbon target data and decreases with increasing target size. In all three target the background is well reproduced by the event-mixing method.

The lower row of the Fig. 5.21 shows the difference of the correlated and uncorrelated distributions. The peak around the nominal kaon mass is fitted with a gaussian distribution. The observed standard deviation of the gaussian fit is ~ 14.2 MeV in all targets.

The kaon signal is determined as the integral over the mass region, specified by the red shaded area in the upper row of Fig. 5.21. Hereby the background contribution is excluded. The amount of signal, observed in the carbon and lead targets under certain trigger conditions⁹, are listed in Table 5.9. The number of identified K^0 candidates reconstructed from carbon and lead targets are very similar. The largest fraction of candidates is measured in the events selected by trigger bit T12. This circumstance will be used in the following analysis to unambiguously define a reaction cross section.

Trigger ID	K^0 signal in C - Tar:	K^0 signal in Pb - Tar:
‘all’	4277	4297
T10	464	337
T11	489	367
T12	2583	2873
T13	2215	2015
T14	1061	1003
T15	1009	1207

Table 5.9: K^0 signal obtained in different targets with a certain trigger selection. The trigger conditions are defined in Section 3.5. The label ‘all’ corresponds to the combination of all trigger bits and, therefore, to the most complete data sample.

5.6.1 Investigation of the Combinatorial Background

The applied topological and kinematic restriction for the daughter particles and the secondary vertex ensure a reasonable preselection of K^0 candidate but can be optimised by evaluating the background contribution to the distributions of the selection quantities (i.e. $hmul$, $d0$, Δz , etc.). A detailed inspection of relevant quantities resulted in optimised selection criteria. The numerical values are summarised in Table 5.10. The corresponding histograms are compiled in Appendix B. Note that the background contribution is qualitatively equal for different targets.

The influence of the more involved selection is demonstrated in Fig. 5.22. The left panel shows the invariant mass distribution, obtained with the preselection choices and

⁹Definition of the trigger conditions can be found in Section 3.5.

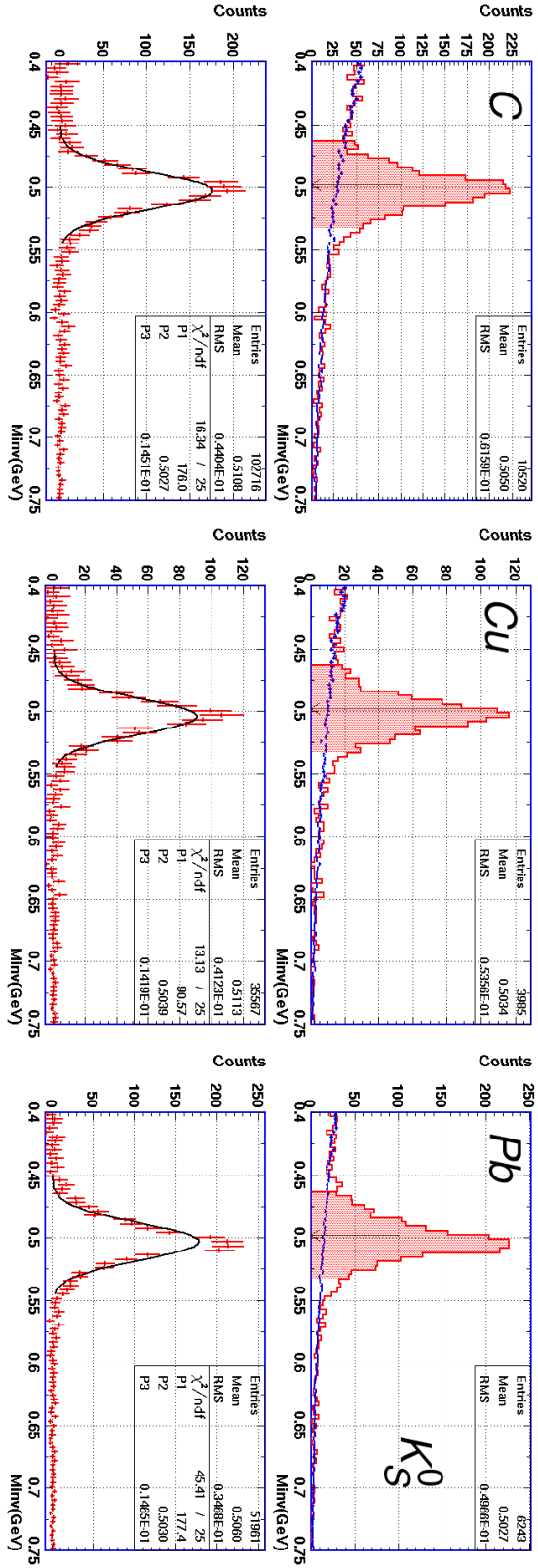


Figure 5.21: Upper row: Invariant mass spectrum of correlated $\pi^+ - \pi^-$ pairs, reconstructed from reactions with the carbon (left panel), copper (middle) and lead (right panel) targets. The combinatorial background is estimated by the event - mixing method. The obtained background distribution is depicted by the blue histogram. Lower row: Background diminished invariant mass spectra. The excess, centred around the nominal kaon mass, is fitted by a gaussian distribution.

the right panel with the optimised one. The background is substantially reduced. A numerical comparison of the K^0 signal expose also a strong reduction of K^0 signal and its significance (i.e. $S\sqrt{S+B}$).

The overall goal of the presented analysis is to compare the dynamic behaviour of K^0 mesons in differently sized targets. Therefore, the relevant impact of the background reduction is the one on the kinematic variables. In Fig. 5.23 the transverse momentum (upper panel), laboratory rapidity (middle) and the laboratory momentum (lower panel) are compared for the original (red symbols) and the optimised (blue symbols) pion pair selection. In order to be directly comparable, the distributions are normalised to the number of K^0 candidates in the respective selection scenario. All three quantities agree within their statistic uncertainties. The discussed background reduction does not affect the dynamic behaviour of the remaining K^0 candidates. To sustain a largest possible number of K^0 candidates only the preselection criteria are applied in the following analysis.

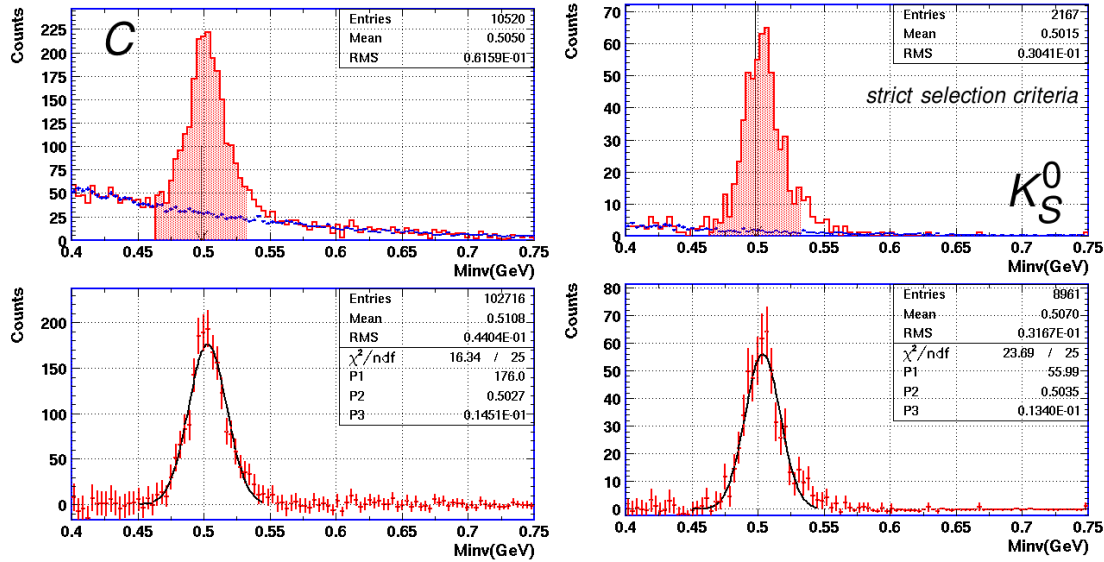


Figure 5.22: Invariant mass distribution of K_S^0 meson candidates with (right panel) and without (left panel) optimised topological selection criteria. Lower row shows the background subtracted mass spectra.

K_S^0 meson \rightarrow	π^+ meson	π^- meson
	$hmul > 35.$	$hmul > 27.$
	$ d_0 > 0.9 \text{ cm}$	$ d_0 > 0.9 \text{ cm}$
	$p_t > 0.08 \text{ GeV}/c$	$p_t > 0.08 \text{ GeV}/c$
	$ z < 25. \text{ cm}$	$ z < 25. \text{ cm}$
Secondary vertex: $-1. < r_S \cdot \sin(\phi_{K^0} - \phi_S) < 0.6;$ $-25. < \Delta z < 20. \text{ cm};$ $r_S > 1. \text{ cm}$		

Table 5.10: Optimised topological restriction for the selection of K_S^0 candidates.

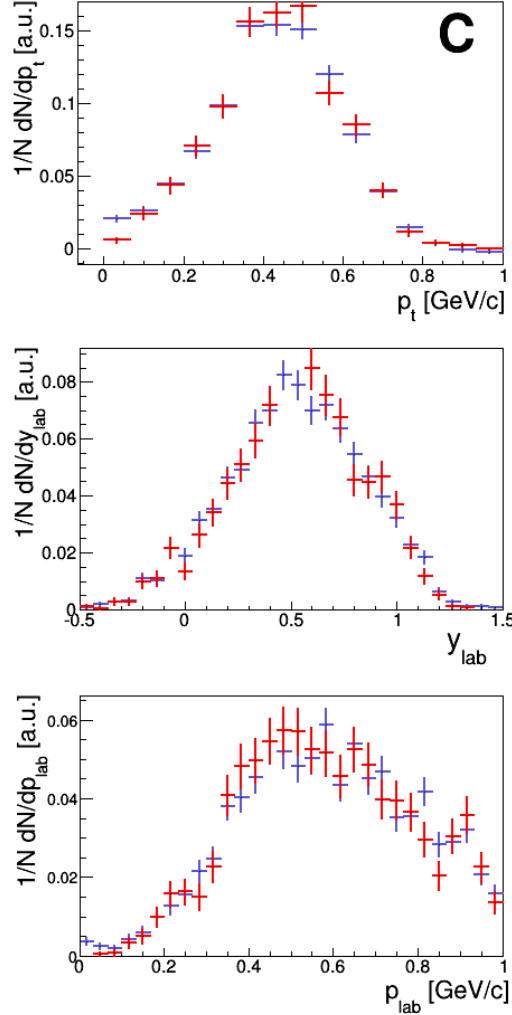


Figure 5.23: Influence of the optimised topological selection criteria on the dynamic variables of K_S^0 meson candidates. Red symbols denote result of the preselection and the blue symbols - the more involved analysis. The spectra are normalised to the respective number of K_S^0 candidates. The histograms are obtained from the carbon target data.

To account for the contamination, the combinatorial background is subtracted bin-wise in every momentum bin. Of particular interest is the low momentum signature of K^0 mesons. In Fig. 5.24 the invariant mass distribution is evaluated in the five lowest momentum bins. Below $p_{lab} \sim 100$ MeV/ c the kaon signal is not distinguishable from the fluctuation of the background. Also a more elaborated background reduction procedure could not reveal a designated signal in this momentum region. Above $p_{lab} \sim 100$ MeV/ c a clearly defined excess is visible close to the nominal kaon mass. The mixed-event background description method does not fully reproduce the observation. In the following analysis the characteristic histograms are adjusted to recreate the background to the best possible extend.

5.6.2 Reconstruction Efficiency Considerations

In order to facilitate a direct comparison of the reconstructed quantities from the carbon and lead target data the differences in reconstruction efficiency have to be investigated.

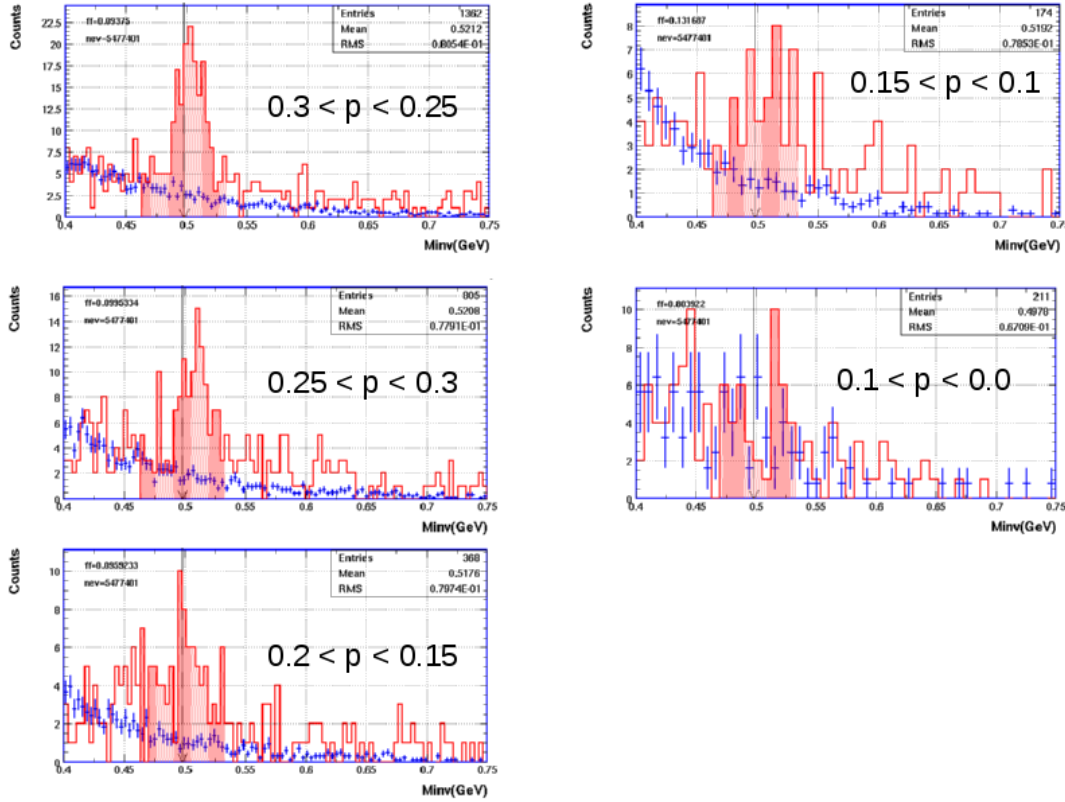


Figure 5.24: Invariant mass distribution of K^0 meson candidates restricted to the labeled momentum selection. The blue histogram demonstrate the corresponding background estimation. ‘p’ denotes the laboratory momentum. Its numerical values are given in GeV/c. The histograms are obtained from the carbon target data.

For the K^0 mesons the same approach is adopted as for the evolution of the reconstruction efficiency of ϕ mesons (Section 5.4). The input phase space distribution of K^0 mesons is parametrised as a flat $p_t - y_{lab}$ formation, embedded into IQMD events and propagated through the detector by the means of the Geant detector simulation. The figures, characterising the procedure, are compiled in Appendix B. The efficiency is evaluated by the comparison of the output and the input phase space distributions in discrete $p_t - y_{lab}$ cells. The resulting efficiency values are depicted in the right panel of Fig. 5.26 as a function of the transverse momentum. The values are integrated over the full rapidity range¹⁰ for the carbon and lead targets. The ‘ratio’ depicts the lead-to-carbon quotient of the both distributions. Reconstruction efficiency in both targets is found to be independent of momentum in a wide momentum range. A slight deviation is observed merely in the lowest momentum bin. Furthermore, the reconstruction in the lead data seems to be twice as efficient as in the carbon data. The ‘factor two’ does not

¹⁰Efficiency in the differential representation can be found in the Appendix B.

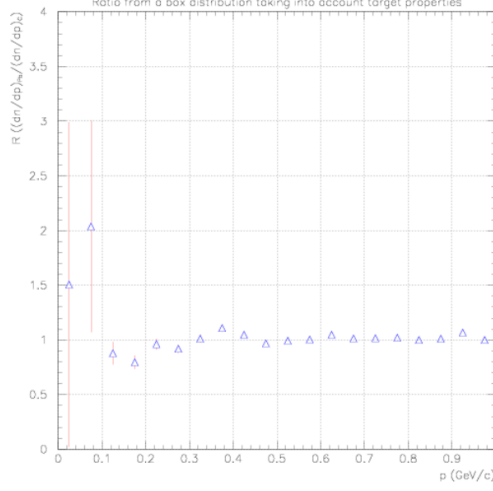


Figure 5.25: Ratio of the reconstruction efficiency of K^0 mesons in lead to the one in carbon as a function of laboratory momentum [LBen].

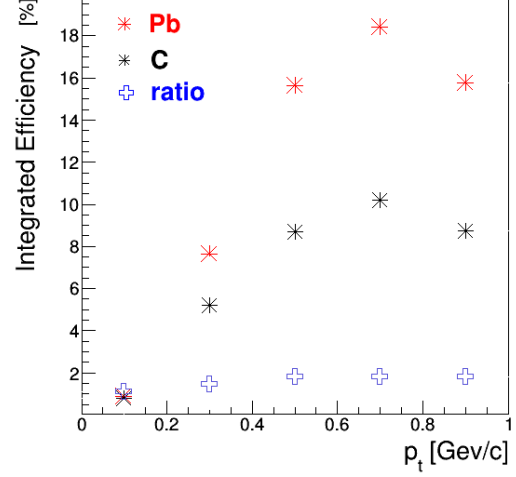


Figure 5.26: Reconstruction efficiency of K^0 mesons in lead and carbon targets, as well as their ratio ($\varepsilon_{Pb}/\varepsilon_C$) as a function of transverse momentum. The statistical error bars are smaller than the symbols.

meet the expectations. The reason is suspected in the not implemented smearing of the vertex distribution due to experimental beam spread.

A similar, however more involved, study was performed for the reconstruction of K^0 mesons from pion induced reactions on a carbon and lead targets at an incident beam momentum of $p_{\pi^-} = 1.15$ GeV/c. The resulting efficiency ratio as a function of momentum is shown in the left panel of Fig. 5.25. The momentum dependance is similar to the present analysis but the relative reconstruction capability in both targets is equal over a large momentum range. Details of the performed simulations can be found in [Ben07]. Based on this analysis, the reconstruction in carbon and lead targets is considered equally efficient and not momentum dependent.

5.6.3 Phase Space Distributions of K_S^0 Mesons from Reactions with Different Targets

Fig. 5.27 depicts the K_S^0 meson candidate in the transverse momentum-rapidity plane. The red curves demonstrate the geometrical restrictions of the RPC and BAR sub-detectors. Since K_S^0 mesons are reconstructed from their decay products, a wide phase space coverage can be reached. A substantial fraction of K_S^0 candidates is reconstructed outside the geometrical detector acceptance. A priori, there is no lower momentum limit for the K^0 reconstruction, as long as the resulting pions are fast enough to reach the CDC. In the present analysis, as discussed above, K_S^0 candidates could be reconstructed

reliably down to $p_{lab} \sim 100 \text{ MeV}/c$.

Already in this representation it is obvious that the bulk of K_S^0 candidates, produced in the lead target, is shifted in rapidity compared to the carbon target. Also the low transverse momentum region appears to be populated differently. The dynamic behaviour in different targets is compared in Fig. 5.28. Distributions of p_t (left panel), y_{lab} (middle) and p_{lab} (right panel) are normalised to the respective number of recorded events for each target. The differences in the kinematic variable are not as strongly pronounced as for the Λ baryon (see discussion in the previous section). Especially the lead-like behaviour of the copper data is not observed. The spectra appear to scale with the target size. For instance, the rapidity distribution from carbon is shifted with respect to the one from lead. The result from the copper data lies in between.

The influence of a KN in-medium potential manifest itself in a repulsive mean field. The repulsion from the nucleons influences the momentum distribution K^0 meson in the final state, by ‘*shifting*’ it to larger values. Assuming the (density dependent) in-medium effects being much smaller in the carbon nucleus than in the lead system, the momentum distributions of K^0 mesons from both targets should be shifted with respect to each other.

The momentum distribution in the heavy lead target and in the light carbon target are compared by the means of their *ratio* in Fig. 5.30. The ratio is defined as:

$$\mathcal{R}(\sigma_{Pb}/\sigma_C) = \frac{dN/dp_{Pb}}{dN/dp_C} \cdot \frac{N_C}{N_{Pb}} \cdot \frac{\sigma_C}{\sigma_{Pb}} \quad .$$

The complex trigger logic of the given experiment does not allow to unambiguously associated a measured cross section to the full experiment. Based on the observation, that a large fraction of K^0 meson are reconstructed from events fulfilling the trigger condition ‘T12’ (see Table 5.9) the evaluation of momentum ratios is restricted to the data sample, selected by the ‘T12’ condition. In order to verify a possible bias by this selection, the obtained momentum ratio per analysed event is compared to an analogous ratio from the full data sample in Fig. 5.29. Both distribution are comparable within statistical uncertainties. It is concluded that limiting the analysis to a particular trigger selection does not influence the physical implications.

Fig. 5.30 shows the *ratio* observable, normalised to the measured cross section. The distribution exhibits a maximum around $p_{lab} \sim 0.3 \text{ GeV}/c$ and adopt a constant value at large momenta. The observed behaviour can only be explained by the presence of a repulsive KN in-medium potential. The magnitude of the repulsion, however, can only be deduced by a comparison to transport model calculations.

5.7 Transport Model Comparison

The HSD transport approach was very successful in describing the K_S^0 in-medium behaviour, observed by the FOPI collaboration in pion induced reaction at $p_{\pi^-} = 1.15 \text{ GeV}/c$. The published results are depicted in Fig. 5.1. The present data sample allows to test the theoretic modelling at a different energy regime and for another strange particle species.

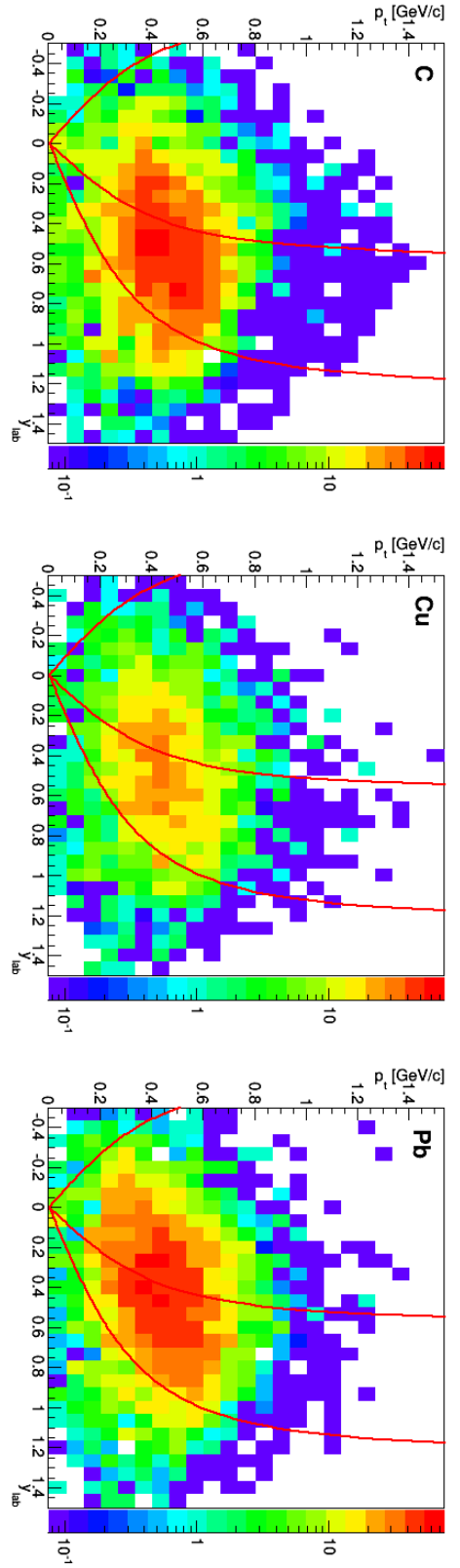


Figure 5.27: Phase space distribution of K^0 meson candidates in terms of the transverse momentum and laboratory rapidity. Red curves show the geometrical restrictions of the RPC and BAR sub-detectors, i.e. $\theta_{lab} = 33^\circ, 59^\circ, 126^\circ$.

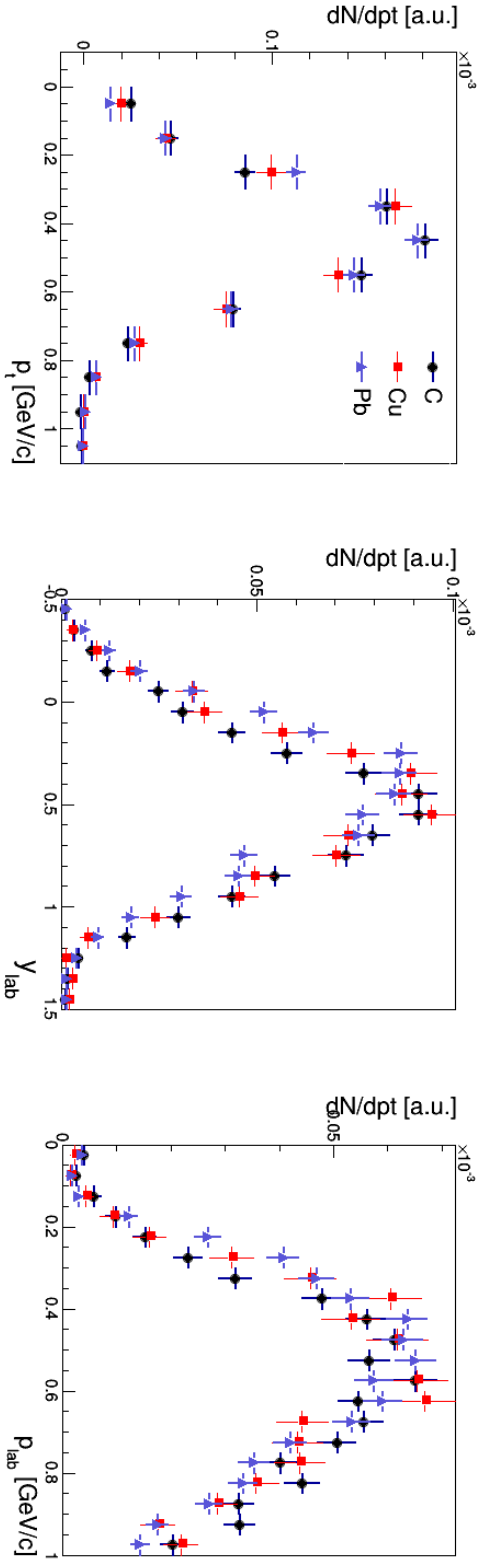


Figure 5.28: Distribution of kinematic variables of K^0 meson candidates, as reconstructed for the reactions in different targets. The spectra are normalised to the respective number of recorded events.

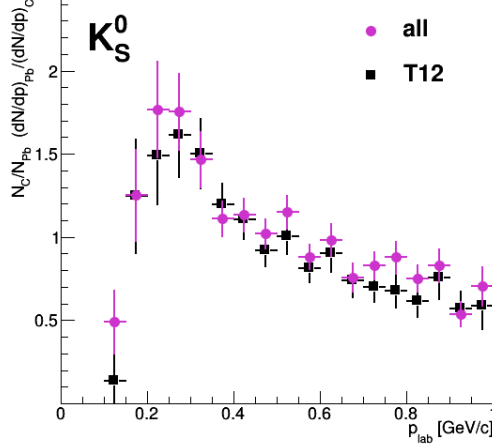


Figure 5.29: Momentum distribution ratio of K^0 meson candidates from the full data sample and from events triggered by the trigger bit T12. See text for details. The error bars are of a statistic nature.

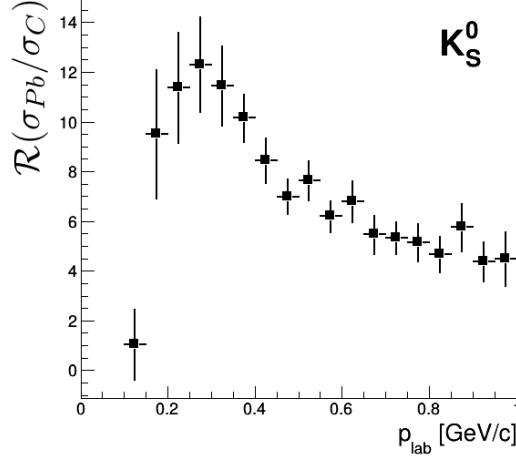


Figure 5.30: Ratio of momentum distributions from lead and carbon targets, normalised to the measured cross section. The error bar are of statistical nature.

In Fig. 5.31 the experimentally determined *ratio* is compared to the prediction of the HSD transport approach. The calculations are filtered for the detector acceptance and normalised to the full geometrical cross section calculated as:

$$\sigma_{HSD}(A)[\text{mb}] = (1.16 \text{ fm} \cdot A^{1/3} + 4 \text{ fm})^2 \cdot 0.1 \cdot \pi.$$

The formula takes into account the peculiarities in the modelling of the incident pion¹¹ and the targets.

Without the assumption of a KN in-medium potential, the model predicts the largest ratio at smallest momenta and a continuous decrease with increasing momentum. The experimental observation favour the other scenario in which the kaons are repelled by the nucleons through the employed KN potential of $U(\rho_0, p = 0) = 20 \pm 5 \text{ MeV}$. The absolute magnitude and the position of the maximum are not reproduced by this calculation.

In Fig. 5.32 the observed *ratios* for K^+ (left panel) and K^- (right panel) mesons are compared to HSD predictions. Due to an additional repulsion by the Coulomb interaction, the *ratio* for the K^+ meson exhibit a similar signature with and without a KN in-medium potential. Nevertheless, the position of the maximum is predicted to be sensitiv to an additional repulsion by the strong interaction. Neither the momentum dependance, nor the magnitude of the experimentally observed *ratio* is close to the predictions.

¹¹The pion is parametrised as a disc with a certain radius.

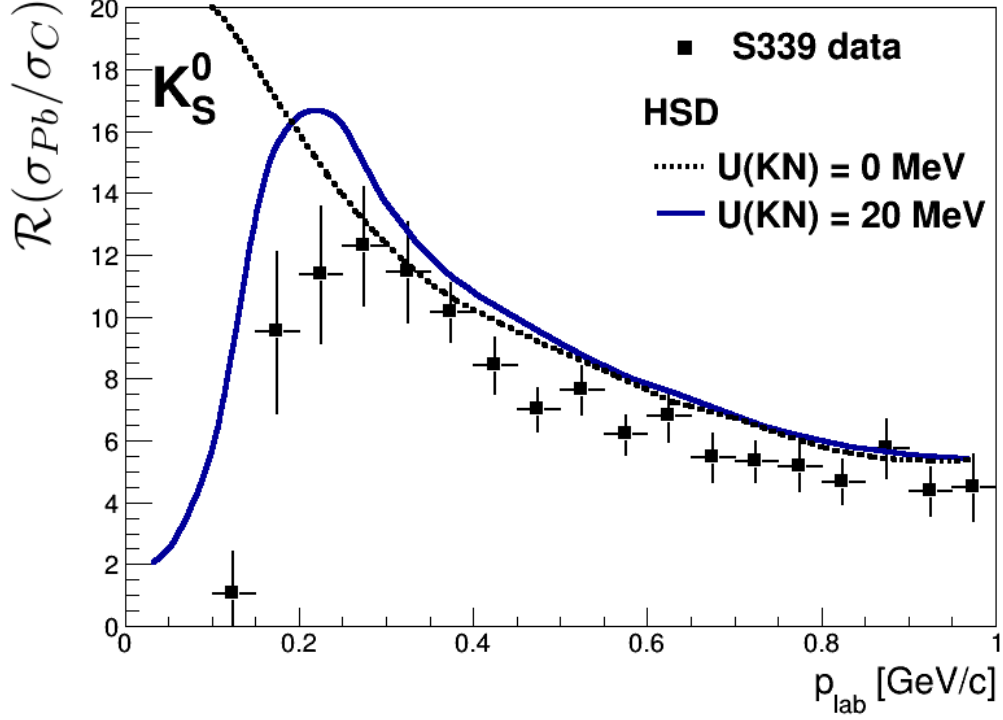


Figure 5.31: The *ratio* observable of K_S^0 mesons in comparison to the predictions of the HSD transport approach with and without the assumption of in-medium modifications. Only statistical errors are shown for the experiment data.

Encouraging for the discussion of a $\bar{K}N$ in-medium potential is the predicted in-medium modification of the *ratio* for K^- mesons. For K^- mesons faster than $p_{lab} \sim 200$ MeV/c in both scenarios a constant *ratio* is predicted. The potential manifest itself in the magnitude of the *ratio*.

At small momenta the data does not show any indication for the predicted rising behaviour. In the remaining momentum part, the data favours the calculations without a $\bar{K}N$ in-medium potential. However, based on the observation for the K^+ meson, it is not a reliable conclusion.

The display of these data aims at motivating the further development of the theoretical modelling.

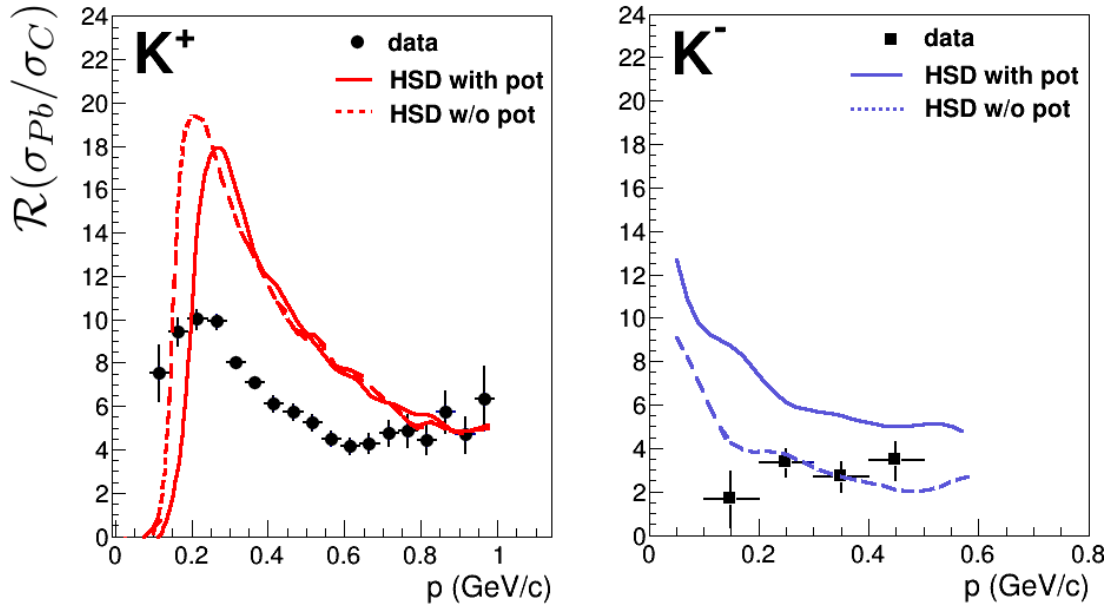


Figure 5.32: The *ratio* observable of K^+ mesons (left panel) and K^- mesons (right panel) in comparison to the predictions of the HSD transport approach with and without the assumption of respective in-medium potentials. The data is normalised to the geometrical cross section. Only statistical errors are shown for the experiment data.

Chapter 6

Conclusion

Strangeness conservation by the strong interaction makes nuclear matter, to a large extend, transparent to strange particles¹ at low energies. Production mechanism in heavy-ion reactions, which enable the strangeness production close or even below the corresponding threshold energy, ensures that the strange particles originate from the dense phase of the collision. Possible alteration of hadrons' mass, production cross section or width in dense and/or hot nuclear matter may bear information about partial restoration of chiral symmetry. Strange particles, like positively charged kaons, have no mechanism to be reabsorbed in heavy ion collisions at SIS-18 energies. Their final state phase space distribution is only influenced by elastic processes and the propagation in mean field potentials. The study of production yield was proposed as a tool for the search of in-medium effects. Spectral functions of kaons and antikaons have been explored extensively by the KaoS collaboration. The conclusion about the fundamental properties of QCD were highly model dependant.

The study of the collective motion provides a further, independent observable for possible in-medium effects. Reconstructed from the azimuthal distribution in the final state, it is sensitiv to the entire time development of the collision. In presented work the collective motion of charged kaons have been studied in Ni+Ni collisions at an incident energy of 1.91 AGeV within the FOPI experiment. The asymmetries of the azimuthal distribution in the final state of kaons and antikaons has been systematically investigated. The centrality, momentum and rapidity dependance have been examined in detail in the experimental data and from the results of transport calculations. The contribution of the Coulomb interaction to the final state observations has been pointed out.

The collective motion of protons is dictated by the pressure gradient in the collision. Positively charged kaons were found to exhibit a collective deflection opposite to that of protons in the plane of the reaction. This phenomenon is referred to as 'antiflow' and could be reproduced by the HSD and IQMD transport calculations under the assumption of a repulsive KN potential. The implemented value of $U(\rho_0, p=0)_{KN} = 20 \pm 5$ MeV is sufficient in the IQMD approach to reproduce the data. HSD, with the same amount of repulsion, overestimates slightly the flow signature in peripheral collisions. In the plane

¹Not claimed for anti-strange particles.

perpendicular to the reaction plane, K^+ mesons show a weak ‘squeeze out’. Also this signature is explained by the presence of an in-medium potential. Beyond mid-rapidity, no sensitivity to the effects of the medium is predicted by the transport calculations.

Negatively charged kaons were found to be emitted isotropically, within large statistic uncertainties though. Both transport calculations agree that the observed patterns can not be explained without the assumption of a $\bar{K}N$ potential. Best agreement is achieved with the IQMD transport approach. The implemented $U(\rho_0, p = 0)_{\bar{K}N} = -50 \pm 5$ MeV slightly overestimates the data. Within the comparison to IQMD a potential of $U_{\bar{K}N} = -40 \pm 10$ MeV would explain the experimental flow pattern. However, this observation of the $\bar{K}N$ potential has to be handled with care. The IQMD model describes antikaons in a quasi particle picture and does not account for the significant influence of the resonant nature of antikaons. The more accurate, coupled channel, approach of HSD also suggest an in-medium $\bar{K}N$ potential, but of a smaller amount.

The results of the current analysis are found to be in agreement with all comparable results from the literature. Part of the analysis has been published in Phys. Rev. C 90, 025210 (2014). The author significantly contributed to the publication.

In the considered heavy-ion collisions the nuclear matter is heated and compressed to ~ 2 -3 times the normal nuclear matter density. The above discussed study is expanded by the investigation of in-medium effects at normal nuclear matter density in pion induced reactions.

Strangeness production is examined in the reactions: $\pi^- + C$, Cu and Pb , with pion incident momentum of $p_{\pi^-} = 1.7$ GeV/c. Motivated by an analogous measurement at lower pion incident momentum ($p_{\pi^-} = 1.15$ GeV/c) the ratio of the momentum distribution of strange particles produced in the heavy target to a respective distribution in a light target is expected to be sensitiv to the effects of the medium. In the present work the strange particles: K^+ , K^- , K_S^0 , ϕ meson and Λ baryon has been reconstructed. Systematik investigation of the background contribution has been performed. Strategies in background reduction and optimised description has been developed. Reconstruction efficiency has been studied by the mean of the Geant simulation.

The obtained results reveal the following observations:

The measured yield of ϕ mesons support the hypothesis of $Z^{2/3}$ scaling of the production cross section. Due to the lack of beam intensity, the total amount of measured ϕ mesons is too low to do the anticipated study of the transparency ratio.

The Λ baryon reconstructed from reactions with a heavy and light targets exhibit different dynamic behaviour. The difference is attributed to scattering processes, since the effects of the medium due to strong interaction are expected outside the reached kinematic acceptance.

Negatively charged kaons from reactions with heavy and light targets have been observed to behave very similarly, suggesting a strong contribution from inelastic scattering.

The K^+ and K_S^0 mesons could be reconstructed down to a relatively small momentum of $p_{lab} \sim 100$ MeV/c. The momentum ratio observable exhibits a typical signature of in-medium repulsion. In the case of K^+ mesons the contribution from the electromag-

netic interaction impede the distinction between the strong and Coulomb interaction. Comparison to the transport calculations demonstrated the necessity for a further development of theoretical modelling.

The present work aims at creating a conceivably complete sample of strange particle observation under different physical conditions. The created convolution may inspire the advancement of theoretical modelling and be used as reference and motivation for further measurements.

“Everything not saved will be lost.”
- Nintendo ‘quit screen’ icon

Appendix A

Journal Publication on Charged Kaon Flow

Azimuthal emission patterns of K^+ and of K^- mesons in Ni + Ni collisions near the strangeness production threshold

V. Zinyuk,^{1,*} T. I. Kang,^{2,3,†} Y. Leifels,² N. Herrmann,¹ B. Hong,³ R. Averbeck,² A. Andronic,² V. Barret,⁴ Z. Basrak,⁵ N. Bastid,⁴ M. L. Benabderrahmane,¹ M. Berger,^{6,7} P. Buehler,⁸ M. Cargnelli,⁸ R. Čaplar,⁵ I. Carevic,⁹ P. Crochet,⁴ I. Deppner,¹ P. Dupieux,⁴ M. Dželalija,⁹ L. Fabbietti,^{6,7} Z. Fodor,¹⁰ P. Gasik,¹¹ I. Gašparić,⁵ Y. Grishkin,¹² O. N. Hartmann,² K. D. Hildenbrand,² J. Kecskemeti,¹⁰ Y. J. Kim,² M. Kirejczyk,¹¹ M. Kiš,^{2,5} P. Koczon,² R. Kotte,¹³ A. Lebedev,¹² A. Le Fèvre,² J. L. Liu,^{1,14} X. Lopez,⁴ V. Manko,¹⁵ J. Marton,⁸ T. Matulewicz,¹¹ R. Münzer,^{6,7} M. Petrovici,¹⁶ K. Piasecki,¹¹ F. Rami,¹⁷ A. Reischl,¹ W. Reisdorf,² M. S. Ryu,³ P. Schmidt,⁸ A. Schütttauf,² Z. Seres,¹⁰ B. Sikora,¹¹ K. S. Sim,³ V. Simion,¹⁶ K. Siwek-Wilczyńska,¹¹ V. Smolyankin,¹² K. Suzuki,⁸ Z. Tyminski,¹¹ P. Wagner,¹⁷ E. Widmann,⁸ K. Wiśniewski,^{1,11} Z. G. Xiao,¹⁸ I. Yushmanov,¹⁵ Y. Zhang,^{1,19} A. Zhilin,¹² and J. Zmeskal⁸

(FOPI Collaboration)

¹Physikalisches Institut der Universität Heidelberg, Heidelberg, Germany

²GSI Helmholtzzentrum für Schwerionenforschung GmbH, Darmstadt, Germany

³Korea University, Seoul, Korea

⁴Laboratoire de Physique Corpusculaire, IN2P3/CNRS, and Université Blaise Pascal, Clermont-Ferrand, France

⁵Ruđer Bošković Institute, Zagreb, Croatia

⁶Excellence Cluster Universe, Technische Universität München, Garching, Germany

⁷E12, Physik Department, Technische Universität München, Garching, Germany

⁸Stefan-Meyer-Institut für subatomare Physik, Österreichische Akademie der Wissenschaften, Wien, Austria

⁹University of Split, Split, Croatia

¹⁰Wigner RCP, RMKI, Budapest, Hungary

¹¹Institute of Experimental Physics, Faculty of Physics, University of Warsaw, Warsaw, Poland

¹²Institute for Theoretical and Experimental Physics, Moscow, Russia

¹³Institut für Strahlenphysik, Helmholtz-Zentrum Dresden-Rossendorf, Dresden, Germany

¹⁴Harbin Institute of Technology, Harbin, China

¹⁵Kurchatov Institute, Moscow, Russia

¹⁶Institute for Nuclear Physics and Engineering, Bucharest, Romania

¹⁷Institut Pluridisciplinaire Hubert Curien and Université de Strasbourg, Strasbourg, France

¹⁸Department of Physics, Tsinghua University, Beijing 100084, China

¹⁹Institute of Modern Physics, Chinese Academy of Sciences, Lanzhou, China

E. Bratkovskaya^{1,2} and C. Hartnack³

¹Frankfurt Institute for Advanced Studies, Frankfurt am Main, Germany

²Institute for Theoretical Physics, Johann Wolfgang Goethe Universität, Frankfurt am Main, Germany

³SUBATECH, UMR 6457, Ecole des Mines de Nantes - IN2P3/CNRS - Université de Nantes, Nantes, France

(Received 8 March 2013; revised manuscript received 28 April 2014; published 25 August 2014)

Azimuthal emission patterns of K^\pm mesons have been measured in Ni + Ni collisions with the FOPI spectrometer at a beam kinetic energy of 1.91 A GeV. The transverse momentum p_T integrated directed and elliptic flow of K^+ and K^- mesons as well as the centrality dependence of p_T - differential directed flow of K^+ mesons are compared to the predictions of hadron string dynamics and isospin quantum molecular dynamics transport models. The data exhibits different propagation patterns of K^+ and K^- mesons in the compressed and heated nuclear medium and favor the existence of a kaon-nucleon in-medium potential, repulsive for K^+ mesons and attractive for K^- mesons.

DOI: [10.1103/PhysRevC.90.025210](https://doi.org/10.1103/PhysRevC.90.025210)

PACS number(s): 25.75.Dw, 25.75.Ld, 13.75.Jz, 24.10.-i

I. INTRODUCTION

Relativistic heavy-ion collisions at bombarding energies of 1–2 A GeV provide the unique possibility to study nuclear matter at high temperatures, around 100 MeV, and baryon densities about 2–3 times the normal nuclear matter density

(ρ_0) [1,2]. Under these conditions, the properties of hadrons may be altered as a result of various nontrivial in-medium effects like the partial restoration of the spontaneously broken chiral symmetry, the modified baryon-meson couplings, and the nuclear potential. Whether and how hadronic properties, such as masses, widths, and dispersion relations are modified in the hot and dense nuclear medium is a topic of great current interest. In particular, strange mesons produced around the production threshold energies in nucleon-nucleon collisions are considered to be sensitive to in-medium modifications.

*v.zinyuk@gsi.de

†t.i.kang@gsi.de

TABLE I. Charged kaon acceptance in terms of laboratory momentum and polar angle are shown with corresponding signal-to-background-ratios (S/B) (see text for details).

ToF	θ_{lab} (deg)	K^+		K^-	
		p_{lab} (GeV/c)	S/B	p_{lab} (GeV/c)	S/B
MMRPC	[30, 55]	[0.13, 0.9]	>22	[0.13, 0.7]	>8
PSB	[55, 110]	[0.13, 0.55]	>10	[0.13, 0.45]	>4

Various theoretical approaches agree qualitatively predicting slightly repulsive KN and strongly attractive $\bar{K}N$ potentials [3]. The depth of the $\bar{K}N$ potential at finite densities is, however, not well constrained by currently available data and is a matter of an active theoretical dispute [4]. If the K^-N potential is sufficiently deep, this might have exciting consequences for the stability of neutron stars [5] or for the existence of deeply bound K^- states [6].

Heavy-ion experiments, with the capability to identify kaons and antikaons, have been performed with the KaoS, FOPI, and HADES detector systems at the heavy-ion synchrotron (SIS) of GSI, aiming at measuring the in-medium properties. A significantly enhanced yield of K^- mesons relative to that of K^+ [7,8], an increase of the K^-/K^+ ratio at low kinetic energy of kaons [8,9], and different freeze-out conditions of K^+ and K^- mesons were observed [10], the latter at least partially explained by the production of ϕ mesons [11]. After the suggestion that the KN potential should manifest itself in the collective motion of kaons, referred to as flow [12], a lot of effort was invested to deduce the strength of the kaon potential by measuring the kaon flow in heavy-ion collisions [13–16]. Experimental difficulties due to the small production rate of K^- mesons in comparison to K^+ in the SIS energy regime restrict the measurements. Currently available flow results for K^- mesons are not sufficient to draw conclusions on the existence and strength of the $\bar{K}N$ in-medium potential.

In this article, we report on the simultaneous measurements of K^+ and K^- mesons with a large acceptance spectrometer at an incident beam energy of 1.91 A GeV that is close to the various strangeness production threshold energies. The data are compared to state-of-the-art transport calculations with and without the assumption of an in-medium potential. In particular, we show the azimuthal anisotropy of K^- mesons in a wide range of rapidity and the centrality dependence of p_T differential flow of K^+ mesons.

II. DATA ACCUMULATION AND ANALYSIS

The experiment was performed with the FOPI spectrometer, an azimuthally symmetric apparatus comprising several subdetectors [17]. Recently a high-resolution highly granular time-of-flight (ToF) barrel based on multistrip multigap resistive plate counters (MMRPCs) [18] was added to the FOPI apparatus improving significantly the kaon identification capability. Charged kaons are identified based on the ToF information from MMRPC and plastic scintillator barrel (PSB), combined with the momentum information from the central drift chamber (CDC, $27^\circ < \theta_{\text{lab}} < 113^\circ$), see Table I.

The acceptance range of the detector for K^\pm is shown in the top panel of Fig. 1 in terms of normalized transverse mo-

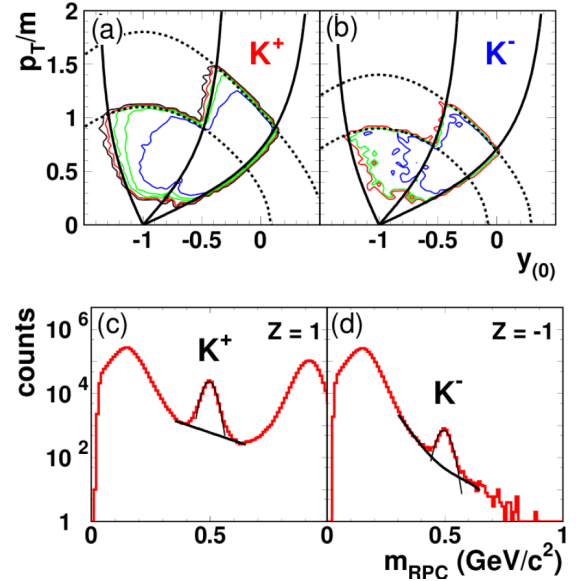


FIG. 1. (Color online) Top: Measured yield of K^+ and K^- mesons: p_T/m_K as a function of $y_{(0)}$. The contour levels correspond to logarithmically increasing intensity. The solid curves denote the geometrical limits of the detector acceptance ($\theta_{\text{lab}} = 30^\circ, 55^\circ$, and 110°). The dashed curves corresponds to $p_{\text{lab}} = 0.55$ and 0.9 GeV/c for K^+ (left) and $p_{\text{lab}} = 0.45$ and 0.7 GeV/c for K^- (right). Bottom: The mass spectra from MMRPC for $Z = 1$ and -1 . The solid lines represent Gaussian fit functions for the signal and exponential functions for the background (see text for details).

mentum, p_T/m , and normalized rapidity, $y_{(0)} = y_{\text{lab}}/y_{\text{cm}} - 1$, defined to be $+1$ (-1) at projectile (target) rapidity. About 69×10^6 events were recorded, triggering on the most central 60% of the total geometrical cross section ($\sigma_{\text{trig}} = 1.6$ b). In total, 233 300 K^+ and 5200 K^- mesons were identified within 2σ around the fitted signal peaks from ToF mass spectra (as visualized for the MMRPC in Fig. 1, bottom). In order to account for the contamination from pions and protons as well as misidentified tracks the background distribution was estimated in a worst-case scenario, i.e., as linear background connecting the minima around the fitted signal peaks in the mass spectra. Following these definitions for signal and background the signal-to-background-ratios (S/B), as listed in Table I, were estimated. The events were sorted into different centrality intervals by imposing conditions on the baryon multiplicity (Mul), shown in Table II. The baryon multiplicity contains all charged particles from the plastic wall ($6.5^\circ < \theta_{\text{lab}} < 23^\circ$) and p , d , t , ^3He , and ^4He from the

TABLE II. Definition of event classes: (a) total, (p) peripheral, and (c) central events. The corresponding cross section σ , mean impact parameter $\langle b \rangle$, the r.m.s. of b distribution: Δb and the reaction plane correction factors f_1 for v_1 and f_2 for v_2 are listed.

	Mul	σ (b)	$\langle b \rangle \pm \Delta b$ (fm)	f_1	f_2
(a)	[20,90]	1.09 ± 0.10	3.90 ± 1.41	1.5 ± 0.1	3.0 ± 0.1
(p)	[20,48]	0.79 ± 0.05	4.54 ± 0.95	1.5 ± 0.1	3.0 ± 0.1
(c)	[49,90]	0.30 ± 0.05	2.11 ± 0.80	1.6 ± 0.1	3.1 ± 0.2

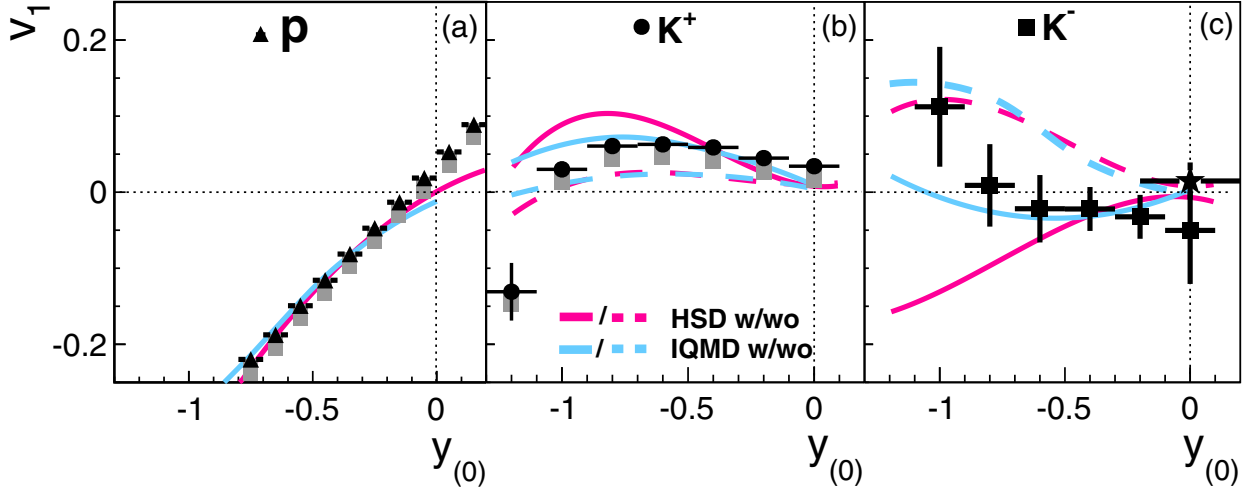


FIG. 2. (Color online) Rapidity dependence of v_1 for protons (a), K^+ (b) and K^- mesons (c), in comparison to HSD and IQMD with (w) and without (wo) in-medium potential. Error bars (boxes) denote statistical (systematic) uncertainties. The star symbols for K^- mesons at mid-rapidity in (c) are from the high statistics data in the range $p < 1.0$ GeV/c with $S/B > 5$.

CDC. The reaction plane was reconstructed eventwise by the transverse momentum method [19] including all particles except identified pions and kaons within the CDC and plastic wall acceptance outside the midrapidity interval $|y_{(0)}| < 0.3$. The particle of interest was excluded in order to avoid autocorrelations.

The phenomenon of collective flow [20] can be quantitatively described in terms of anisotropies of the azimuthal emission pattern, expressed by a Fourier series:

$$\frac{dN}{d\phi} \propto [1 + 2v_1 \cos(\phi) + 2v_2 \cos(2\phi) + \dots], \quad (1)$$

where ϕ is the azimuthal angle of the outgoing particle with respect to the reaction plane [21]. The first-order Fourier coefficient v_1 describes the collective sideward deflection of particles in the reaction plane, called directed flow. The second-order Fourier coefficient v_2 describes the emission

pattern in versus out of the reaction plane, referred to as elliptic flow [15,22]. The Fourier coefficients are corrected for the accuracy of the reaction plane determination according to the Ollitrault method [23]. The mean correction values, f_1 and f_2 (given in Table II) are calculated separately for each evaluated centrality (multiplicity) interval. The correction values f_n are applied to the measured v_n values according to the event's multiplicity. Possible resolution effects due to wide centrality bins, as discussed in [24], were investigated and found to be negligible for the present analysis. Note that the most peripheral events ($Mul < 20$) were rejected to assure a minimal accuracy of the reaction plane determination.

III. RESULTS

The experimental data on v_1 and v_2 of K^\pm for the total event sample (a) (see Table II) are presented as function of $y_{(0)}$ in Figs. 2 and 3. v_1 is by definition antisymmetric with respect

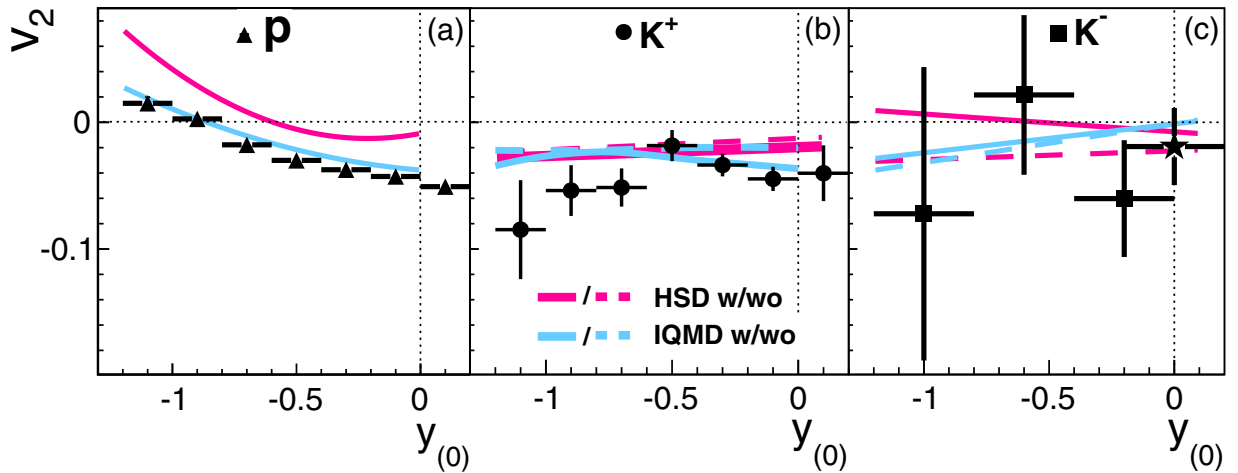


FIG. 3. (Color online) Rapidity dependence of v_2 for protons (a), K^+ (b) and K^- mesons (c), in comparison to HSD and IQMD transport model predictions. Lines and symbols as in Fig. 2.

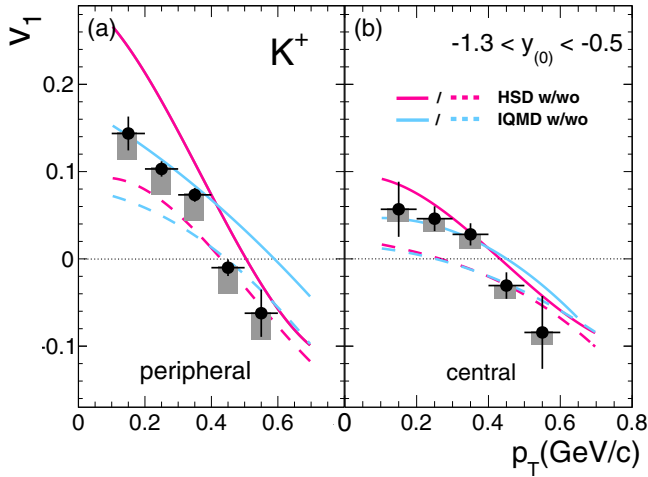


FIG. 4. (Color online) Transverse momentum (p_T) dependence of v_1 distributions for K^+ mesons in peripheral (a) and central (b) collisions in comparison to HSD and IQMD predictions with (solid lines) and without (dashed lines) in-medium potentials.

to midrapidity, therefore it should vanish at midrapidity for a symmetric collision system. However, we observe, like in other FOPI data [15,25], a deviation from zero. Systematic investigation of v_1 at midrapidity ($y_0 = 0$) showed a dependence on centrality, particle type and system size suggesting a correlation with track density. When reconstructing the reaction plane with the best possible accuracy (i.e., largest polar angle range $6.5^\circ < \theta_{\text{lab}} < 113^\circ$) the v_1 at midrapidity was found to be independent of transverse momentum in the system Ni + Ni at 2 AGeV. The origin of the v_1 shift was investigated by means of Monte Carlo study using the GEANT3 package [26]. Within the Monte Carlo framework the FOPI apparatus is described including the resolution in energy deposition and spatial position, front-end electronic processing, hit reconstruction, hit tracking and track matching between the sub-detectors. The output of GEANT was analyzed in the same way as the experimental data. As observed in the data, the v_1 shift at midrapidity was found to depend on centrality and particle type, and to be independent of transverse momentum. However, the magnitude of the shift is underestimated by the simulation, and hence the Monte Carlo data can not be used to correct the experimental values quantitatively. We adopt a conservative approach and attribute the full shift at midrapidity as systematic uncertainty (boxes in Figs. 2 and 4). Since the local track density seen by the CDC only depends on the azimuthal angle and not on the polar angle we assume the systematic uncertainty to be rapidity independent.

The v_1 values of K^- are compatible with zero within the statistical sensitivity of the data (Fig. 2). In order to reduce the statistical error, Fig. 2 also contains a K^- data point with an upper momentum limit of 1.0 GeV/c (star symbol) from subset of runs with improved resolution.

Near target rapidity K^+ mesons show a collective in-plane deflection in the direction opposed to that of protons (Fig. 2). This pattern is called antiflow and is in agreement with previous FOPI measurement [15]. Additionally the K^+

mesons are observed to collectively move out-of-plane (Fig. 3) as indicated by the negative v_2 values. In case of K^- mesons [Figs. 2(c) and 3(c)], both v_1 and v_2 are compatible with zero within the statistical sensitivity of the data, i.e., an isotropic emission pattern is observed.

The KaoS collaboration has measured v_2 coefficients of K^\pm to be $v_2(K^+) = -0.05 \pm 0.03$ and $v_2(K^-) = -0.09 \pm 0.06$ at midrapidity for the same collision system at the same beam energy, however, with a different detector acceptance and collision centrality ($3.8 < b_{\text{geo}} < 6.5$ fm) [16]. The v_2 values from our data, reduced to the same centrality range and acceptance, are compatible with the KaoS results, but do not show any indication for in-plane emission of K^- mesons.

In order to link the flow measurements to the K^\pm properties in the nuclear medium, a comparison to the predictions of transport model calculations is necessary. For this analysis we utilize the hadron string dynamics (HSD) model [27] and isospin quantum molecular dynamics (IQMD) [28] offering a state-of-the-art description of kaon dynamics [4]. The models employ different in-medium scenarios for the modification of strange particle properties in the dense and hot medium: in HSD the chiral perturbation theory [29] for kaons and a coupled channel G -matrix approach [30] for antikaons are implemented. In IQMD transport approach the relativistic mean-field model for kaons and antikaons based on a chiral SU(3) model is used [31].

The centrality selection imposed on the data is realized by weighting the events with an impact parameter dependent function. This function is obtained by evaluating the influence of a multiplicity selection on the impact parameter distribution within the IQMD model which describes the multiplicity distribution – after cluster formation – reasonably well. Earlier data on flow of K^+ mesons [15] and the K_s^0 spectra in pion induced reactions [32] were successfully described by HSD with a repulsive KN potential of 20 ± 5 MeV for particles at rest ($p = 0$), at normal nuclear matter density and a linear dependence on baryon density. Employing this parametrization for the K^+N potential in both HSD and IQMD, and a similar, but attractive one with $U_{K^-N}(\rho = \rho_0, p = 0) = -45$ MeV in IQMD and a G -matrix formalism corresponding to $U_{K^-N}(\rho = \rho_0, p = 0) = -50$ MeV in HSD for the K^-N potential the model predictions depicted by the full lines in Figs. 2 and 3 are obtained. The phase space distributions obtained from the transport calculations are filtered for the detector acceptance. The flow observables are calculated using the true reaction plane. Typical statistical uncertainties in the calculations are of the order $\Delta v_1 \approx 0.005$ and $\Delta v_2 \approx 0.01$. The effect of the in-medium potentials is visible in the difference to the model calculations without in-medium potential (dashed lines) that still include $K^\pm N$ rescattering and absorption processes for K^- mesons.

Inspection of Fig. 2 reveals that according to the transport models the largest sensitivity to the presence of in-medium potentials is achieved with the side flow observable, v_1 , near target rapidity. Without any in-medium modifications the K^+ mesons should be emitted nearly isotropic, i.e., v_1 and v_2 values are close to zero. The presence of a repulsive K^+N potential manifests itself by pushing the K^+ mesons away from the protons, thus generating the antiflow signature

of K^+ mesons. The magnitude of the antiproton flow is correctly described by IQMD transport approach with the assumption of a K^+N potential of 20 ± 5 MeV, while HSD predicts the antiproton flow effect but quantitatively overestimates the magnitude of the experimentally observed antiproton flow. For K^- mesons the interpretation is different: because of the strong absorption due to strangeness exchange reactions with baryons, an antiproton flow signature is expected without the presence of a potential (Fig. 2). This is clearly disfavored by the data. Assuming an additional attraction of K^- toward protons, due to strong interaction, the IQMD transport model predicts an almost isotropic emission pattern, as it is observed in the data. HSD predicts a strong flow signature in the near target region, though. Following both model predictions the data indicate the presence of an attractive K^-N potential. Following the IQMD approach, the depth of the potential can be constrained to $U_{K^-N}(\rho = \rho_0, p = 0) = -40 \pm 10$ MeV.

The second harmonic v_2 of K^+ mesons (Fig. 3) shows a squeeze-out signature at mid-rapidity that is explained within the IQMD model by the presence of an in-medium potential. The HSD model predicts a weak squeeze-out effect, deviating by about $2 \Delta v_2$ from the data. Within the statistical sensitivity of the data this observable does not show any sensitivity to the potential away from midrapidity.

In the near target rapidity region the experimental v_2 is underestimated by both model calculations. However, the deviation is at the limit of the statistical significance. Note that also the v_2 values of protons (Fig. 3) are not reproduced by HSD. In the case of K^- elliptic flow, experimental uncertainties are too large to draw any conclusion about the K^-N potential.

To probe the consistency of the transport model description of the current data, shown in Fig. 2, we present in Fig. 4 the differential dependence of v_1 on the transverse momentum p_T for K^+ mesons near target rapidity ($-1.3 < y_{(0)} < -0.5$) for the two centrality classes (p) and (c) defined in Table II. Within the acceptance the in-plane asymmetry changes from positive to negative values with increasing transverse momenta, while the theoretically predicted drop to zero at small transverse momenta is experimentally not accessible.

In the central event sample the data are compatible with both, HSD and IQMD, calculations employing the in-medium potential described above, in agreement to previously published FOPI results [15]. The IQMD calculations reproduce the transverse momentum dependence and the strength of the v_1 coefficient for low transverse momenta ($p_T < 0.4$ GeV/c). This quality of IQMD is also observed for the peripheral event sample, where the data show a slightly stronger p_T dependence as compared to the central case. Within HSD the transverse momentum dependence is strongly overpredicted leading to very large asymmetries at small p_T that are excluded by the data.

The influence of the Coulomb interaction was studied within the HSD transport model by comparing the flow patterns of K_S^0 and K^+ mesons. Both members of the isospin doublet show a similar p_T dependence of v_1 , but in case of K^+ mesons the predicted antiproton flow is up to 12% higher at low transverse momenta. This difference is attributed to

the additional repulsion due to electromagnetic interaction between K^+ mesons and protons in the near target region. The long-range influence of the Coulomb attraction/repulsion between kaons and nucleons of the projectile and target remnants was investigated with the SACA clusterization algorithm [33], which simulates the propagation of particles in the Coulomb field up to flight times of ~ 10000 fm/c. Statistically significant influence was found only for the very small momenta, beneath the detector acceptance. We conclude that most of the asymmetry is caused by the strong interaction and that v_1 can constrain the depth of the KN potential.

IV. CONCLUSIONS

We have measured the azimuthal emission patterns of K^\pm mesons in heavy-ion collisions near the strangeness production threshold energies. In case of K^+ mesons a weak in-plane antiproton flow with respect to protons and a slight squeeze out are observed. For K^- mesons, within large statistic uncertainties, isotropic emission pattern is observed. Despite the large uncertainties, the comparison to two independent predictions of HSD and IQMD without potential especially of the first Fourier coefficient implies the existence of a weakly attractive K^-N in-medium potential. Furthermore, the IQMD transport approach, which is able to reproduce the dynamics of nucleons and K^+ mesons, suggests a K^-N in-medium potential of $U_{K^-N} = -40 \pm 10$ MeV.

The theoretical modeling of the in-medium potentials, or more generally of the in-medium interactions, is reasonably well achieved within the IQMD transport approach as is demonstrated by the detailed comparison of the differential flow pattern of the K^+ mesons. Within HSD, the general dynamics of nucleons and K^+ mesons is reproduced as well, however the quantitative description of the flow pattern in some regions of the phase space is not accurately achieved yet. The observed dependencies and sensitivities point to the feasibility to extract the strength of the in-medium potentials from a quantitative description of a complete set of flow data. More systematic data and theoretical efforts are clearly necessary to reach this important goal.

ACKNOWLEDGMENTS

This work was supported by German BMBF Contract No. 05P12VHFC7, the Korea Science and Engineering Foundation (KOSEF) under Grant No. F01-2006- 000-10035-0, by German BMBF Contract No. 05P12RFFCQ, by the Polish Ministry of Science and Higher Education (DFG/34/2007), the agreement between GSI and IN2P3/CEA, the HIC for FAIR, the Hungarian OTKA Grant No. 71989, by NSFC (Project No. 11079025), by DAAD (PPP D/03/44611), by DFG (Projekt 446-KOR-113/76/04) and by the EU, 7th Framework Program, Integrated Infrastructure: Strongly Interacting Matter (Hadron Physics), Contract No. RII3-CT-2004-506078.

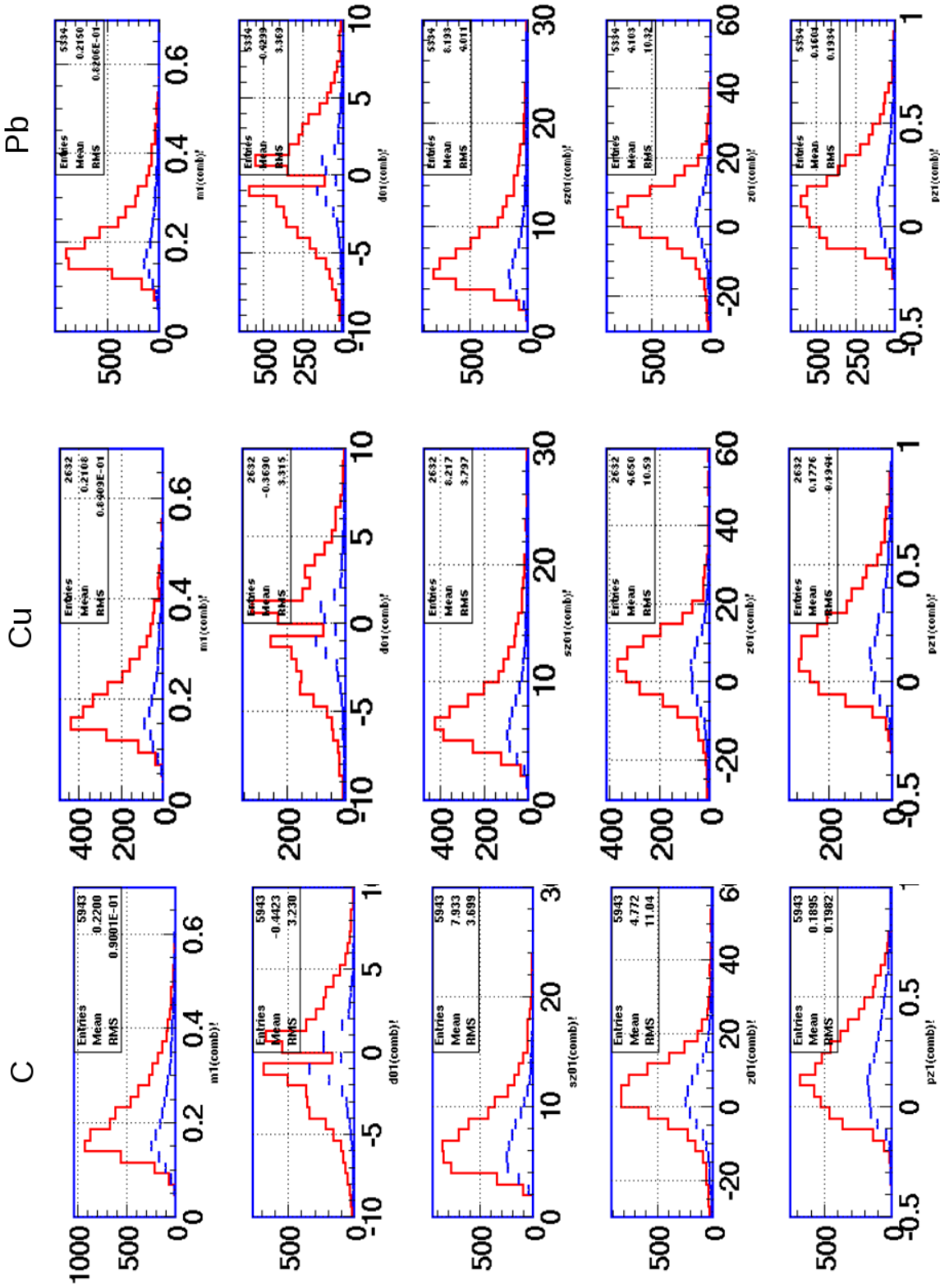
- [1] C. Fuchs, *Prog. Part. Nucl. Phys.* **56**, 1 (2006).
- [2] B. Hong *et al.*, *Phys. Rev. C* **57**, 244 (1998).
- [3] D. B. Kaplan and A. E. Nelson, *Phys. Lett. B* **175**, 57 (1986); G. E. Brown and M. Rho, *Phys. Rev. Lett.* **66**, 2720 (1991); G. Q. Li and C. M. Ko, *Phys. Lett. B* **338**, 118 (1994); M. Lutz, *ibid.* **426**, 12 (1998); *Nucl. Phys. A* **574**, 755 (1994); T. Waas, N. Kaiser, and W. Weise, *Phys. Lett. B* **379**, 34 (1996); **365**, 12 (1996).
- [4] C. Hartnack *et al.*, *Phys. Rep.* **510**, 119 (2012), and references therein.
- [5] J. M. Lattimer and M. Prakash, *Phys. Rep.* **442**, 109 (2007); J. Lattimer and M. Prakash, *W. Weise, Prog. Part. Nucl. Phys.* **67**, 299 (2012).
- [6] Y. Akaishi and T. Yamazaki, *Phys. Rev. C* **65**, 044005 (2002).
- [7] D. Best *et al.*, *Nucl. Phys. A* **625**, 307 (1997).
- [8] F. Laue *et al.*, *Phys. Rev. Lett.* **82**, 1640 (1999).
- [9] K. Wisniewski *et al.*, *Eur. Phys. J. A* **9**, 515 (2000).
- [10] A. Förster *et al.*, *Phys. Rev. C* **75**, 024906 (2007).
- [11] G. Agakishiev *et al.* (HADES Collaboration), *Phys. Rev. C* **80**, 025209 (2009); M. Lorenz *et al.*, *PoS BORMIO* **2010**, 038 (2010).
- [12] G. Q. Li, C. M. Ko, and Bao-An Li, *Phys. Rev. Lett.* **74**, 235 (1995).
- [13] J. Ritman *et al.*, *Z. Phys. A* **352**, 355 (1995).
- [14] Y. Shin *et al.*, *Phys. Rev. Lett.* **81**, 1576 (1998).
- [15] P. Crochet *et al.*, *Phys. Lett. B* **486**, 6 (2000).
- [16] F. Uhlig *et al.*, *Phys. Rev. Lett.* **95**, 012301 (2005).
- [17] A. Gobbi *et al.*, *Nucl. Instr. Meth. A* **324**, 156 (1993); J. Ritman *et al.*, *Nucl. Phys. B, Proc., Suppl.* **44**, 708 (1995).
- [18] M. Kiš *et al.*, *Nucl. Instr. and Meth. A* **646**, 27 (2011).
- [19] P. Danielewicz and G. Odyniec, *Phys. Lett. B* **157**, 146 (1985).
- [20] N. Herrmann *et al.*, *Ann. Rev. Nucl. Part. Sci.* **49**, 581 (1999); W. Reisdorf and H. G. Ritter *et al.*, *ibid.* **47**, 663 (1997).
- [21] S. Voloshin and Y. Zhang, *Z. Phys. C* **70**, 665 (1996).
- [22] A. Andronic *et al.*, *Phys. Lett. B* **612**, 173 (2005).
- [23] Jean-Yves Ollitrault, *Nucl. Phys. A* **638**, 195c (1998).
- [24] H. Masui and A. Schmah, *arXiv:1212.3650* [nucl-ex].
- [25] W. Reisdorf *et al.*, *Nucl. Phys. A* **876**, 1 (2012).
- [26] R. Brun *et al.*, GEANT 3.21, Detector Description and Simulation Tool, <http://consult.cern.ch/writeup/geant/>, 1993.
- [27] W. Cassing *et al.*, *Phys. Rep.* **308**, 65 (1999).
- [28] C. Hartnack *et al.*, *Eur. Phys. J. A* **1**, 151 (1998).
- [29] A. Mishra *et al.*, *Phys. Rev. C* **70**, 044904 (2004).
- [30] W. Cassing, L. Tolos *et al.*, *Nucl. Phys. A* **727**, 59 (2003).
- [31] J. Schaffner-Bielich, I. N. Mishustin, and J. Bondarf, *Nucl. Phys. A* **625**, 325 (1997).
- [32] M. L. Benabderrahmane *et al.*, *Phys. Rev. Lett.* **102**, 182501 (2009).
- [33] R. K. Puri and J. Aichelin, *J. Comput. Phys.* **162**, 245 (2000).

Appendix B

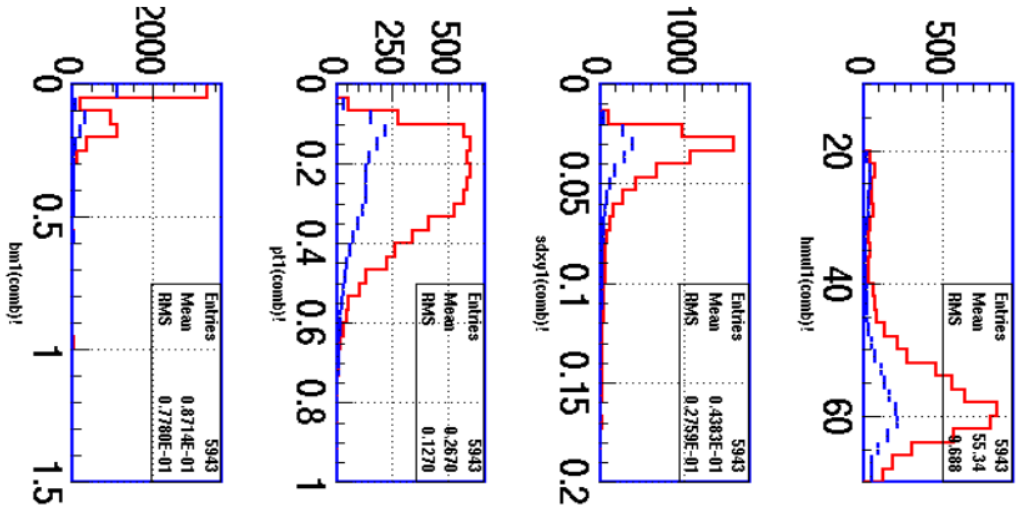
Supplementary Graphics

B.1 Neutral Kaons in S339 Experiment

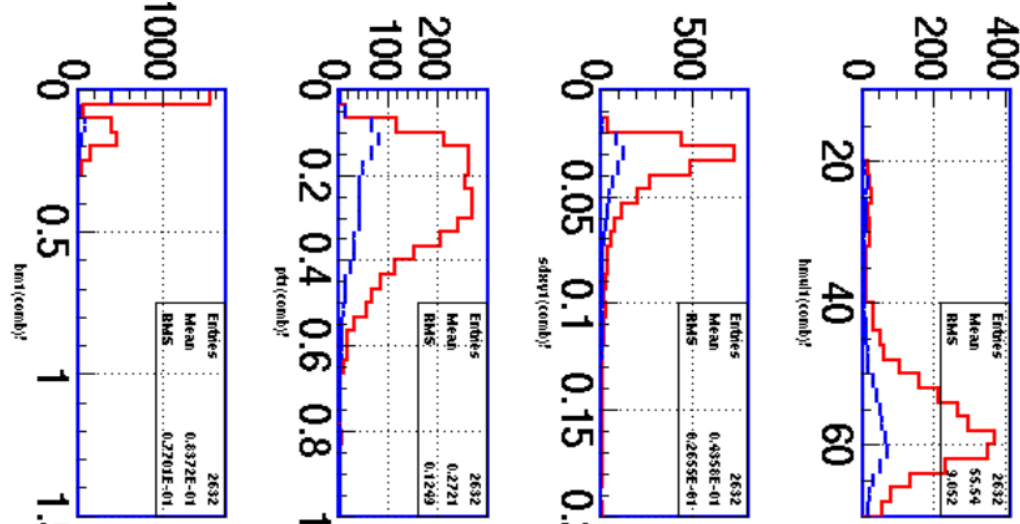
The following plots are used to choose the optimised selection criteria for K_S^0 reconstruction. The red histograms show the signature of correlated pion pairs, the blue histograms denote the combinatorial background (deduced by mixed-event method). The quantities are discussed in Section 5.6.1.



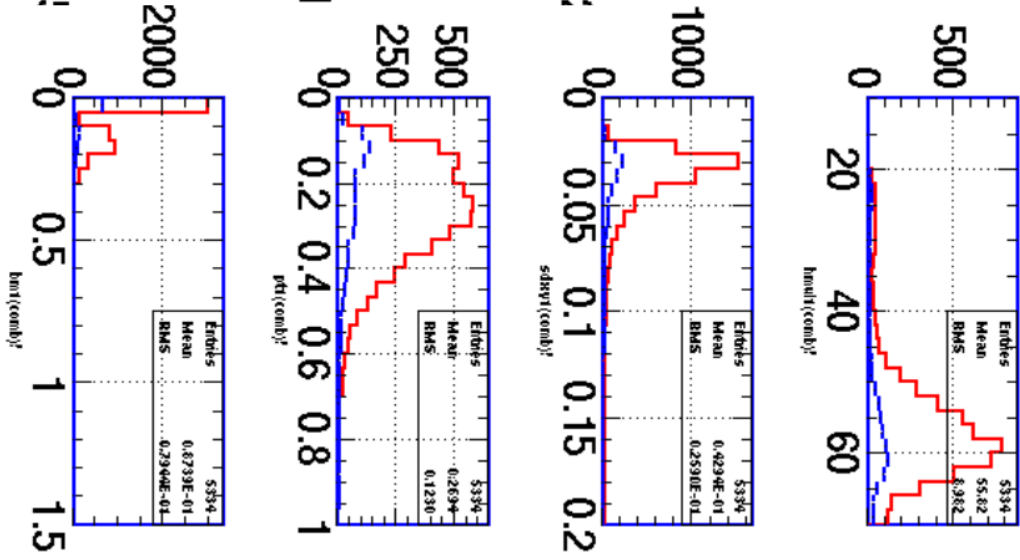
C

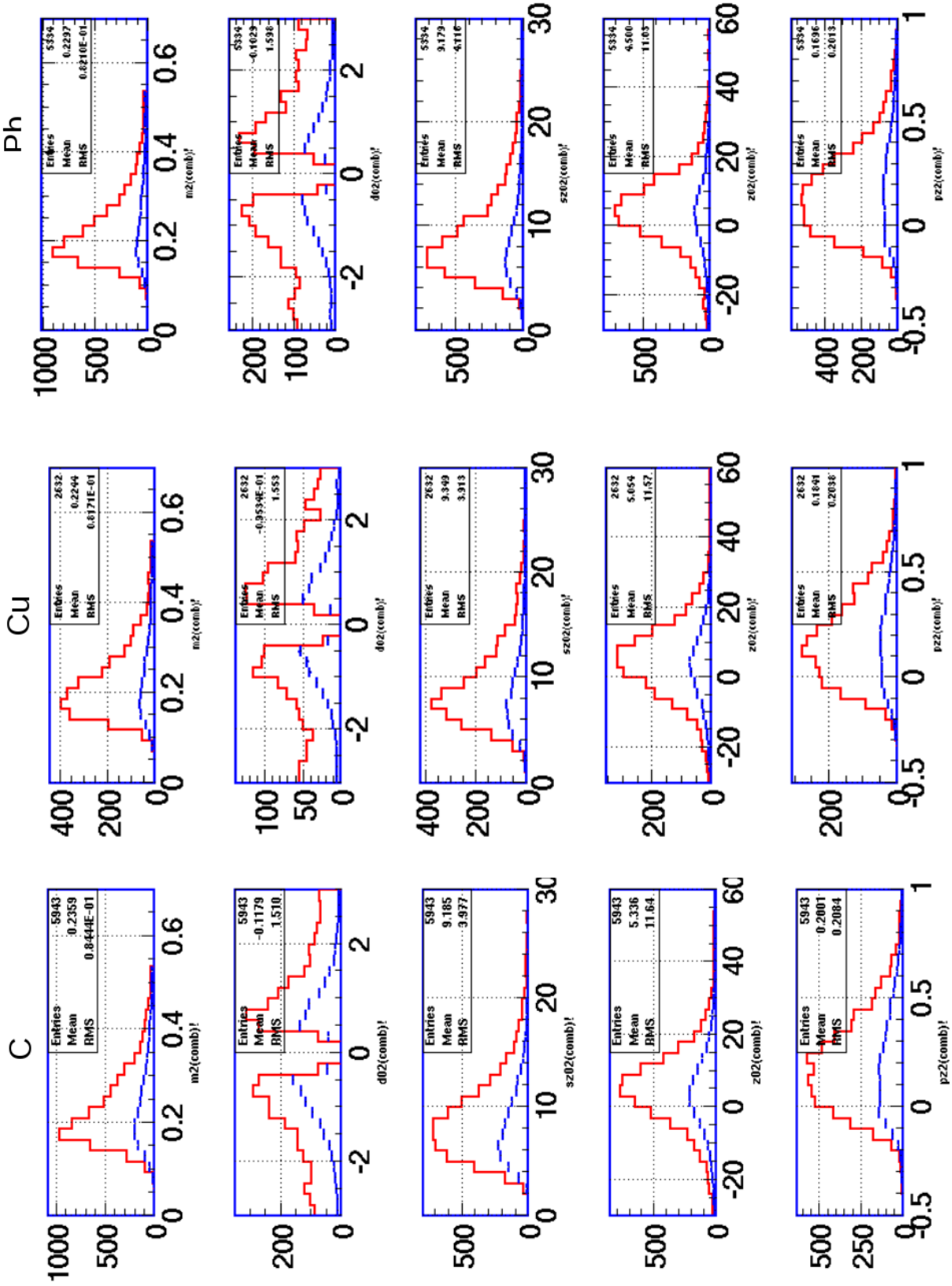


Cu

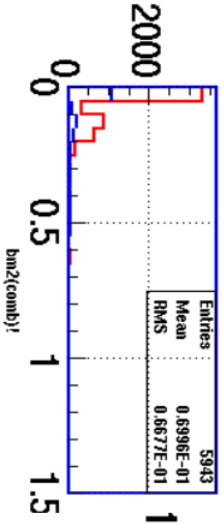
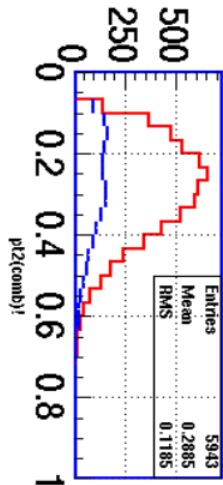
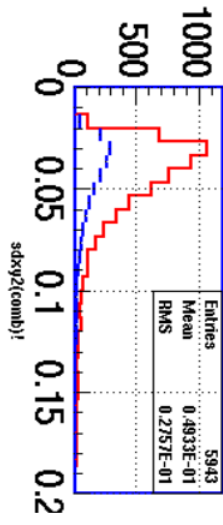
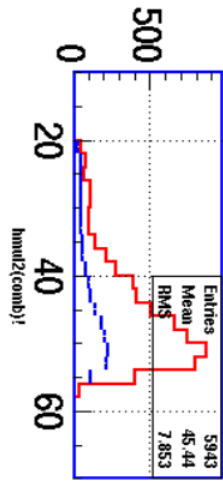


Pb

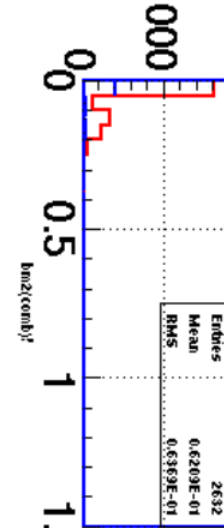
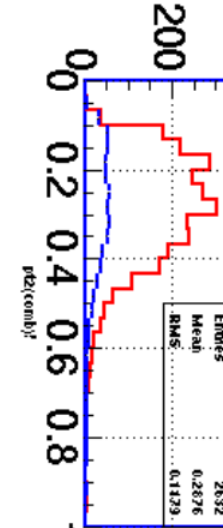
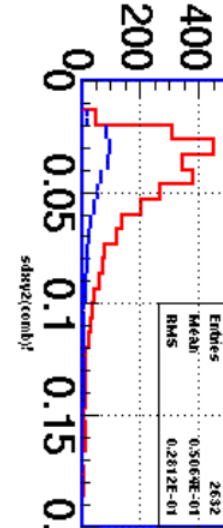
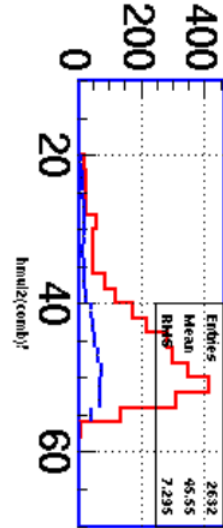




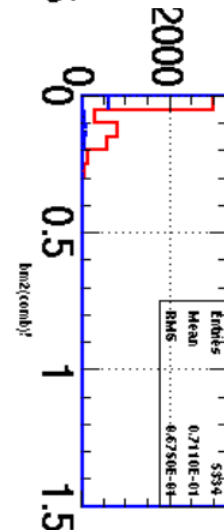
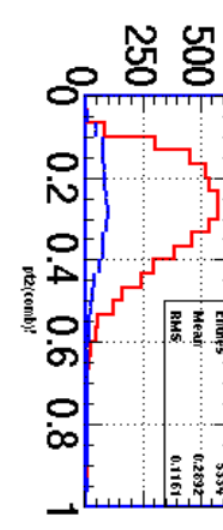
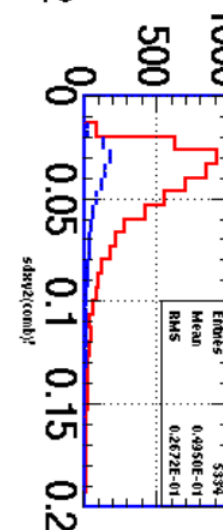
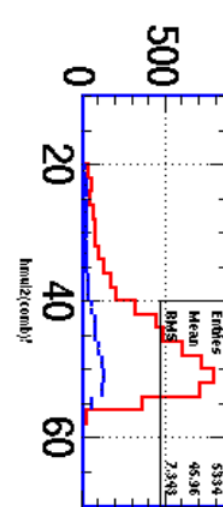
C

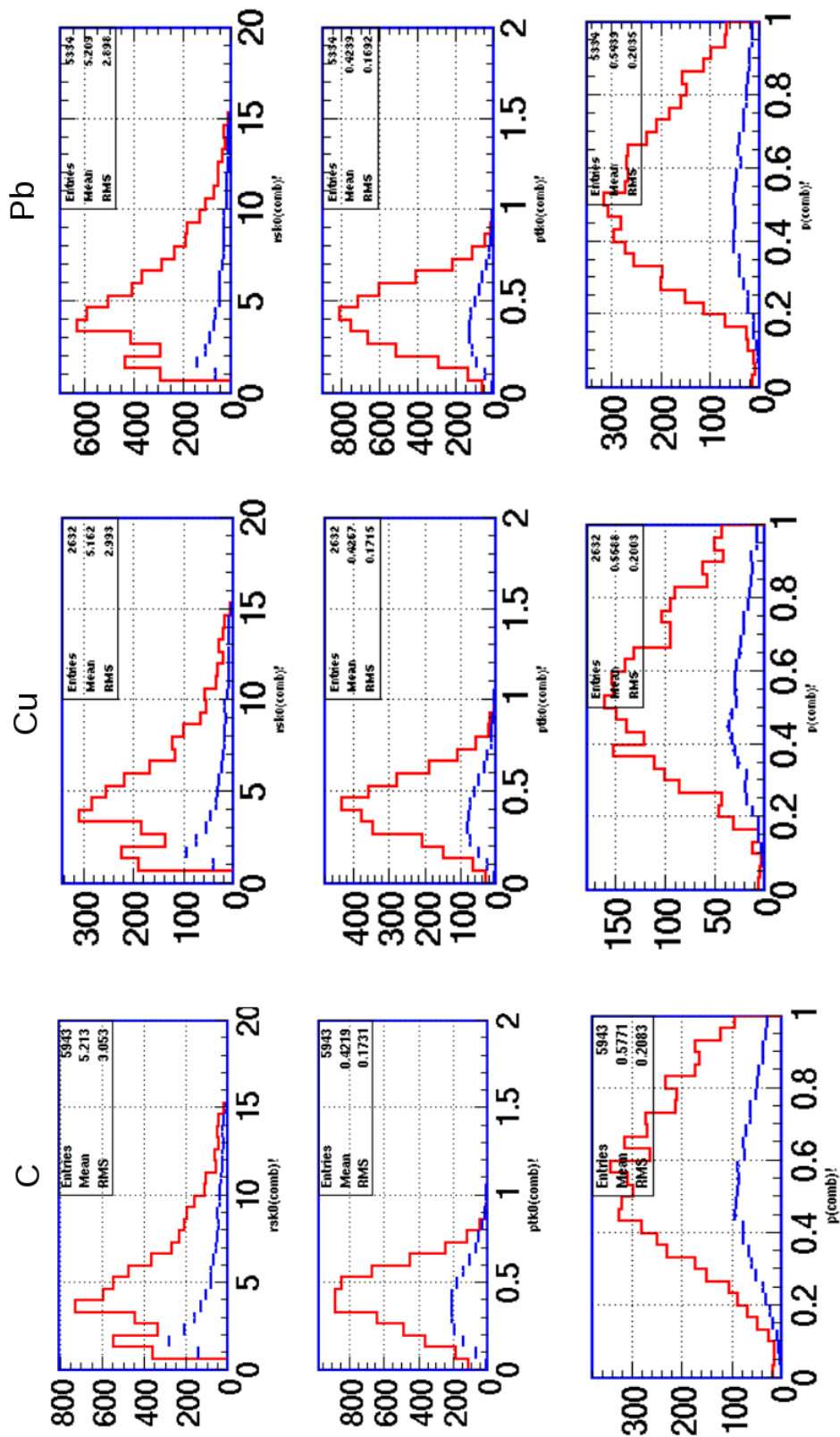


Cu

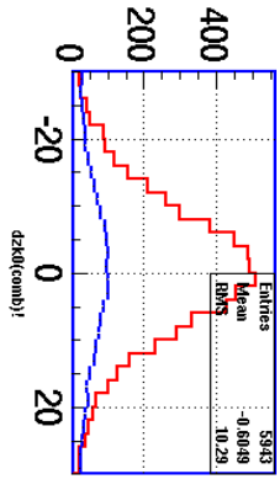
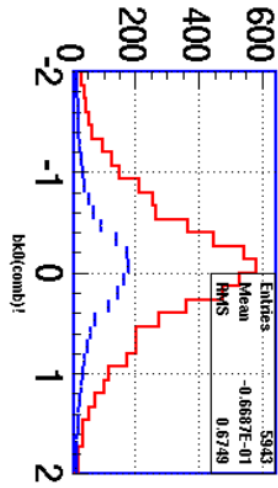


Pb

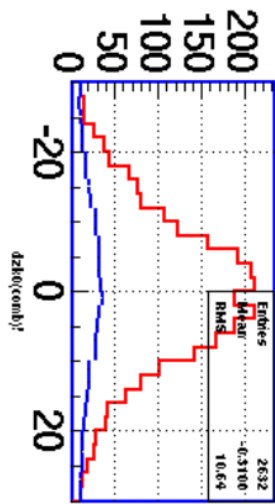
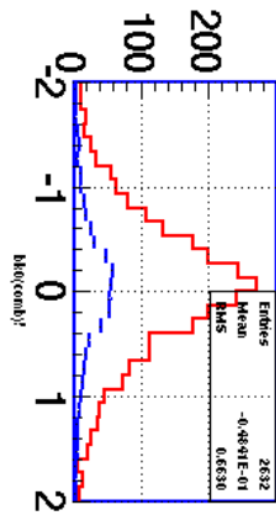




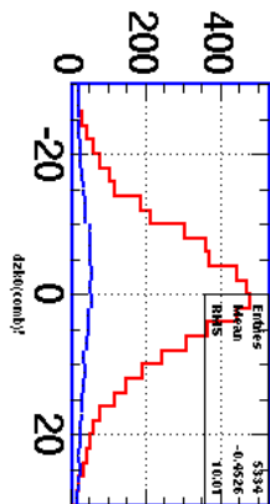
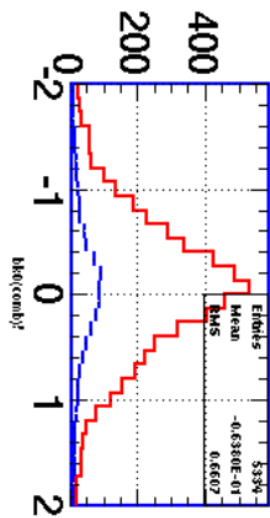
C



Cu



Pb



B.1.1 Reconstruction Efficiency of K_S^0 Mesons

The following diagrams are supplementary for the discussion in Section 5.6.2.

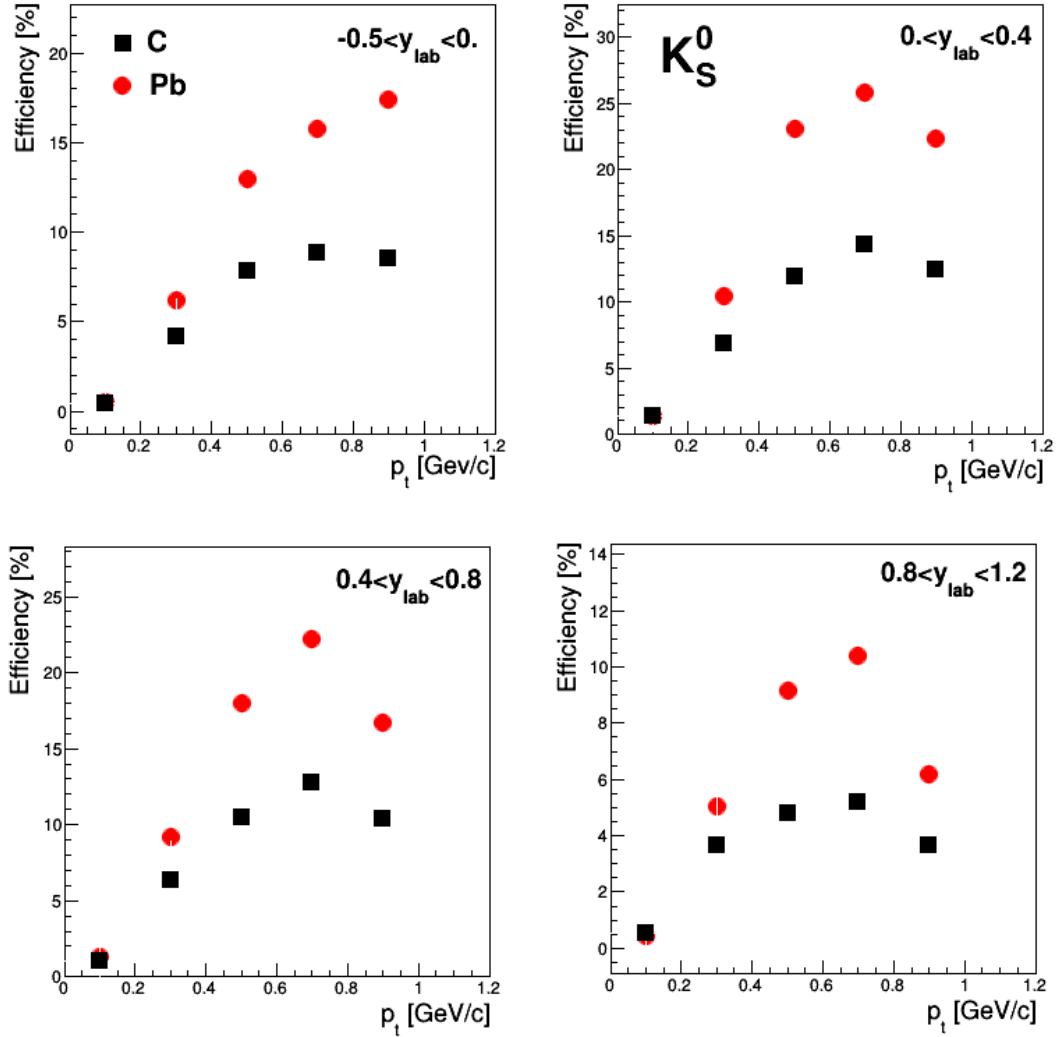


Figure B.1: Reconstruction efficiency of K_S^0 meson in carbon and lead target in various phase space cells.

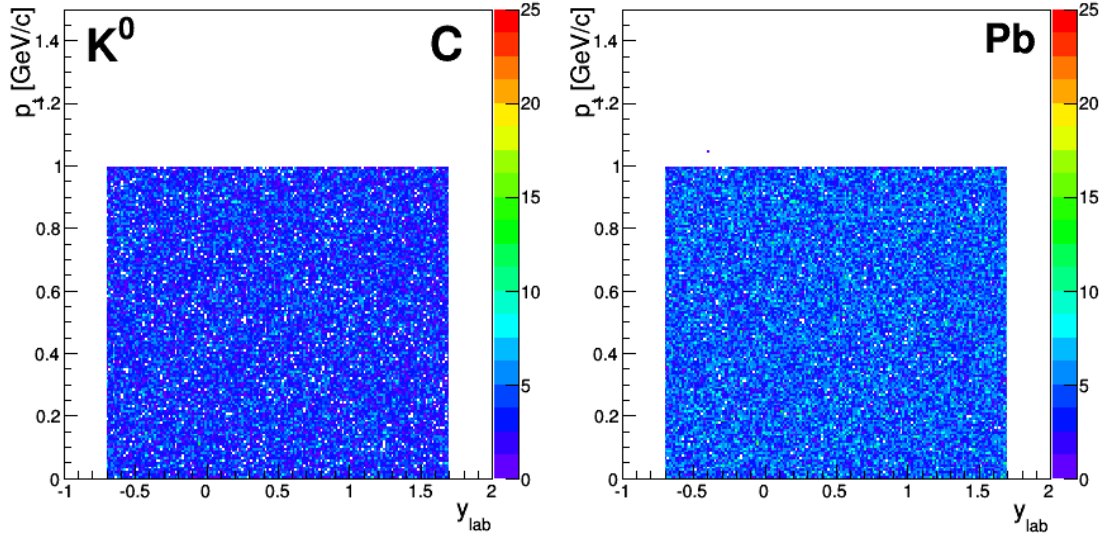


Figure B.2: Parametrisation of the phase space distribution of K^0 meson, which served as the input to the Geant simulation.

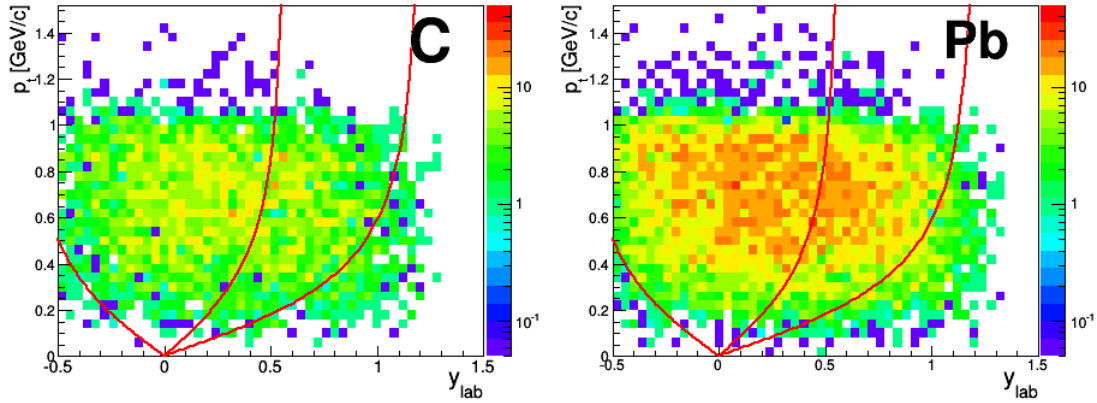


Figure B.3: The phase space distribution of K^0 meson after the propagation through the detector by the Geant simulation.

B.2 Identification of K^+ mesons in S339 Experiment

Mass spectra of positively charged particles, reconstructed in the CDC with a certain momentum selection.

Red vertical lines denote the mass identification region of K^+ mesons candidates. The black lines demonstrate the background estimate.

The quantity ‘p’ denotes the laboratory momentum. The dimension of its numerical values is GeV/c. The identification of K^+ mesons in S339 experiment is discussed in Chapter 5.

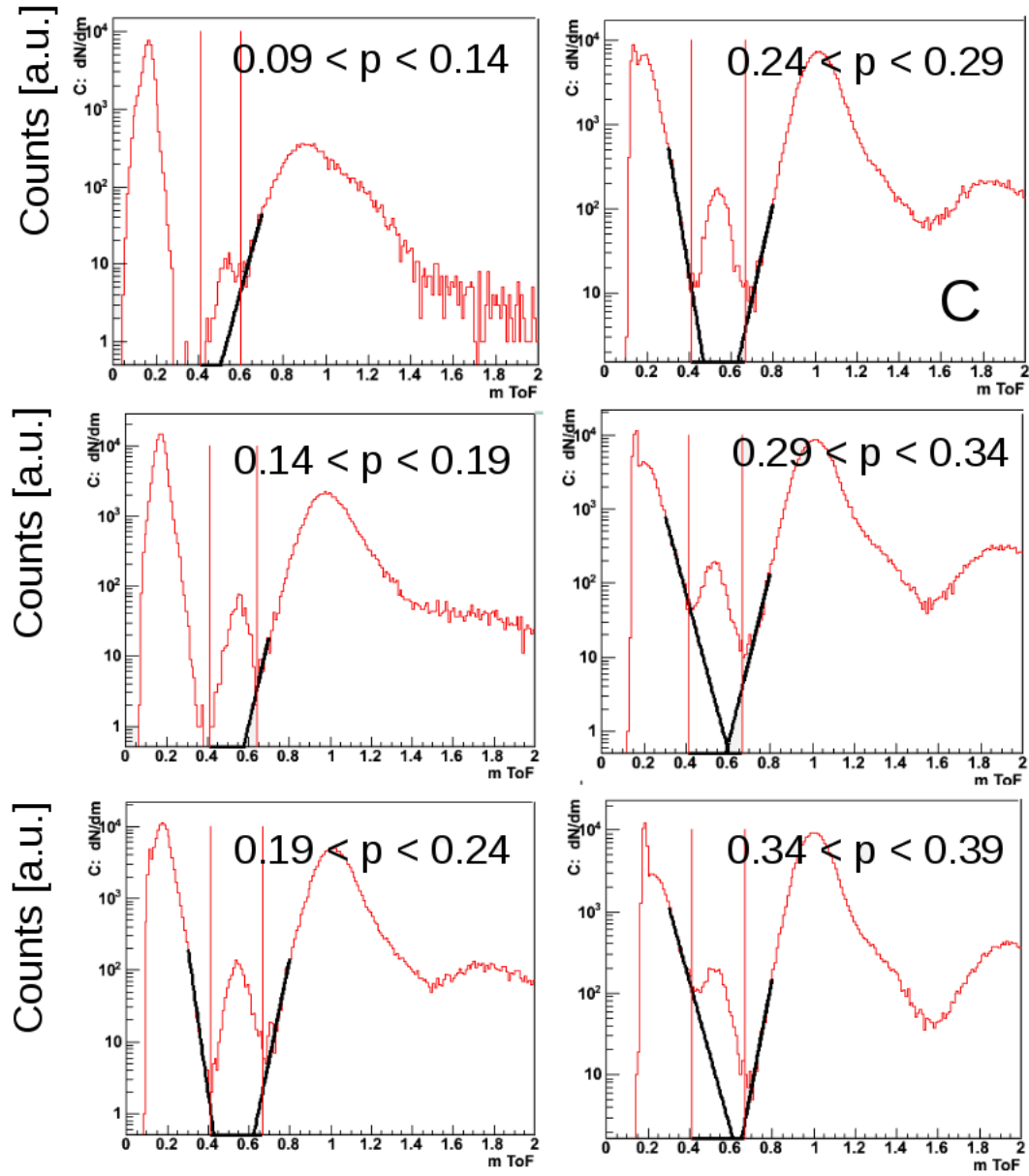


Figure B.4: Carbon target.

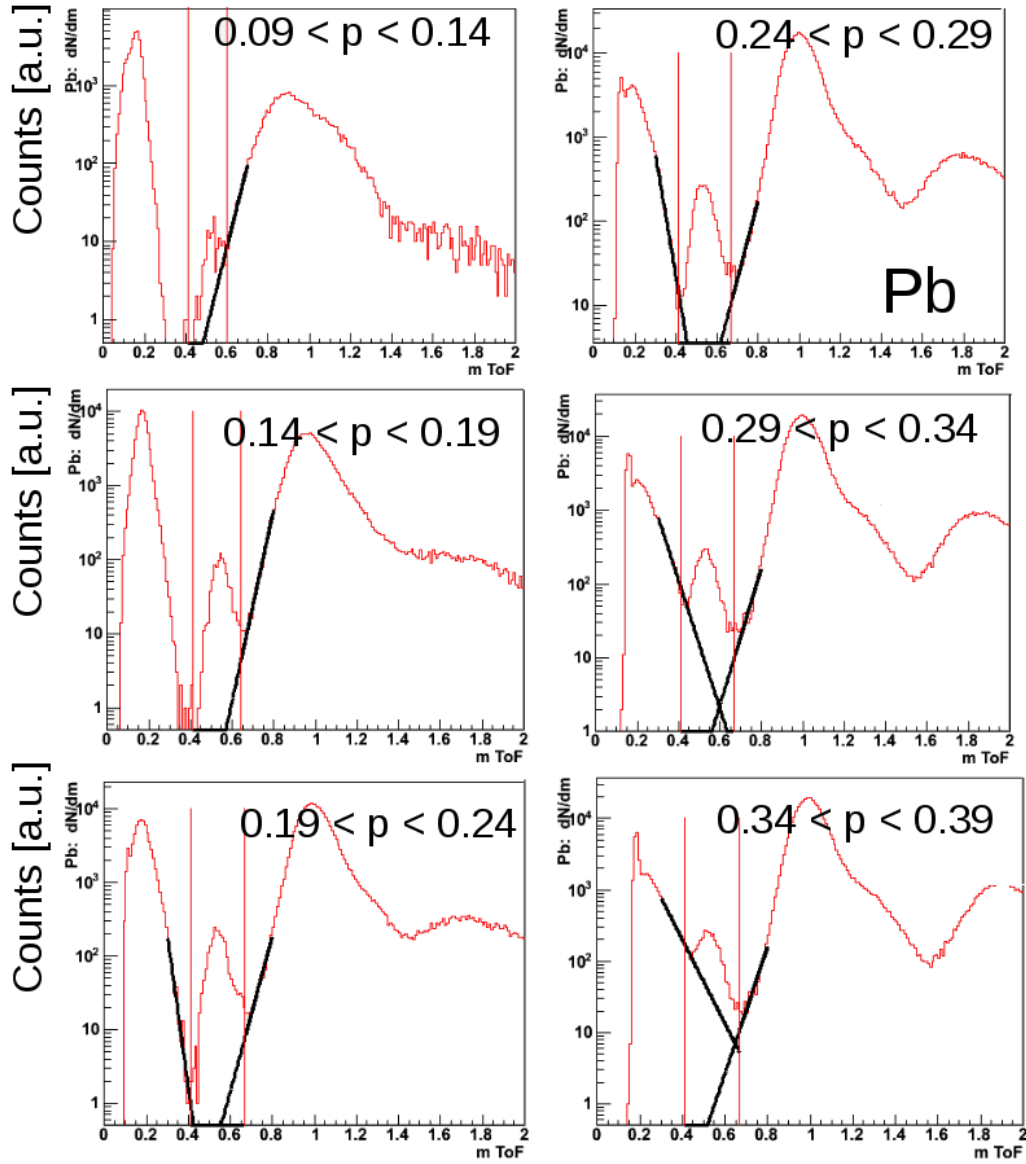


Figure B.5: Lead target.

Appendix C

Centrality Selection in IQMD

Following parameters and definitions were used to reconstruct the Baryon multiplicity within IQMD calculation.

- **Baryon Multiplicity(BarMul):**
PLAWA Multiplicity($z \leq 13$) + CDC-Baryon Multiplicity (p, d, t, ^3He , α).
- **PLAWA Multiplicity:** all charged particles with $z \leq 13$.
- **CDC-Baryon Multiplicity:** p, d, t, ^3He , α .
- **Geometry cuts:** CDC: 27° - 112° , BAR: 55° - 110° , PLAWA: 6° - 27° ;
- **Trigger:** PLAWA Multiplicity > 3 ; at least one charged hit (i.e. $\pi^+/-$, p, d, t or α) in BAR
- Kinethic energies and momenta to reach the corresponding part of the detector:

	CDC		BAR		PLAWA	
	E_{kin} [GeV]	p_{min} $= \sqrt{E_{kin} * 2 * m}$	E_{kin} [GeV]	p_{min} [GeV]	E_{kin} [GeV]	p_{min} [GeV]
$\pi^\pm(0.139)$	—	—	0.038	0.1	0.023	0.08
$p(0.983)$	0.01	0.14	0.03	0.23	0.023	0.21
$d(1.876)$	0.01	0.2	0.035	0.36	0.023	0.29
$t(2.808)$	0.02	0.33	0.036	0.45	0.023	0.36
$^3\text{He}(2.8)$	0.02	0.33	—	—	0.047	0.51
$\alpha(3.72)$	0.02	0.38	—	—	0.047	0.59

Appendix D

Kinematic Variables

A convenient choice of kinematic variables in the analysis of heavy-ion reactions is the one facilitating a simple change of the reference frame. Following quantities have been employed in for the analysis presented in this work. The formula are derived from [PDG].

Rapidity:

The velocity $\beta_z = v_z/c$ along the beam direction of a particle with a total energy of E and a longitudinal momentum component p_z can be described by the rapidity y :

$$y = \tanh^{-1}(\beta_z) = \frac{1}{2} \ln \frac{E + p_z}{E - p_z}. \quad (\text{D.1})$$

The advantage of this representation is the additive behaviour under the Lorentz transformation. The transformation from the measurement in the laboratory reference (y_{lab}) into a corresponding quantity in the center-of-mass reference frame (y') is given by:

$$y' = y - \frac{1}{2} \ln \left(\frac{1 + \beta_{CM}}{1 - \beta_{CM}} \right) = y - y_{cm}. \quad (\text{D.2})$$

Assuming that the relativ velocity between the center-of-mass system and laboratory is β_{cm} .

In the peresnted analysis the scaled rapidity is used in order to simplify the comparision for different beam energies. The scaled rapidity y_0 is defined as:

$$y_0 = \frac{y - y_{cm}}{y_{cm}} = \frac{y}{y_{cm}} - 1. \quad (\text{D.3})$$

In this representation, the target-, mid- and projectile-rapidity correspond to -1, 0 and +1, in a mass symmetric collision system.

The center-of-mass rapidity y_{cm} is calculated from the beam energy E_{Beam} by:

$$y_{cm} = 0.5 \cdot \ln \left(\frac{1 + \beta_{cm}}{1 - \beta_{cm}} \right) \quad \text{with} \quad \beta_{cm} = \sqrt{1 - 1/\gamma_{cm}} \quad (\text{D.4})$$

$$\gamma_{cm} = \frac{E_{lab} + m_2}{E_{cm}} = \dots = \sqrt{\frac{E_{Beam}}{2m_u} + 1} \quad , \quad (\text{D.5})$$

with $E_{cm} = (m_1^2 + m_2^2 + 2E_{lab}m_2)^{1/2}$,

and $E_{lab} = E_{Beam} + m_u$,

and $m_1=m_2=m_u$: the atomic mass.

At $E_{Beam} = 1.91$ AGeV the center-of-mass rapidity amounts to $y_{cm} = 0.89021$.

Transverse momentum:

The transverse momentum p_t is invariant under the Lorentz transformation along the beam direction:

$$p_t = \sqrt{p_x^2 + p_y^2} = \beta_t \gamma m_0 = \frac{\beta_t}{\sqrt{1 - \beta^2}} m_0. \quad (D.6)$$

The transverse momentum can be expressed as a function of rapidity and longitudinal angle or rapidity and total momentum:

$$p_t(y, p, m) = \frac{\sqrt{p^2 - m^2 \sinh^2 y_{lab}}}{\cosh y_{lab}}. \quad (D.7)$$

$$p_t(y, \Theta, m) = \frac{m \sinh(y_{lab}) \tan(\Theta)}{\sqrt{1 - \sinh^2(y_{lab}) \tan^2(\Theta)}}. \quad (D.8)$$

Solving this equation for the longitudinal angle Θ yields the parameterisation of the geometrical acceptance in the phase space diagrams:

$$\Theta = \arctan \frac{p_t}{\sqrt{m^2 + p_t^2} \cdot \sinh y_{lab}}. \quad (D.9)$$

Appendix E

Supplimentary Information of the Targets of the S339 Beam Time

Element	Thickness [mm]	Mass [g/cm ²]	Isotope	Content %	Aver.at.nr Position w.r.t. std.
C	10	1.87	12	98.9	12.01 -4 mm
			13	1.1	
Al	6	1.56	27	100.	27.00 -2 mm
Cu	5	4.41	63	69.2	63.62 -1.5 mm
			65	30.8	
Sn	4	2.83	120	32.4	118.78
			118	24.3	
			116	14.7	
			119	8.6	
			117	7.7	
			124	5.6	
			122	4.6	
			112	1.0	
			114	.7	
			115	.4	
Pb	5	5.76	208	52.4	207.24 -1.5 mm
			206	24.1	
			207	22.1	
			204	1.4	

Appendix F

Strangeness Production Cross Sections in Pion-Induced Reactions

$\pi^- + p \rightarrow$	Threshold $p_{lab}[\text{GeV}/c]$	σ @ 1.7GeV/c
ΛK^0	0.89	0.199 ± 0.012 0.174 ± 0.014
$\Sigma^0 K^0$	1.03	0.110 ± 0.014 0.121 ± 0.01
$\Sigma^- K^+$	1.035	0.153 ± 0.009 0.19 ± 0.012
$\Lambda K^0 \pi^0$	1.14	0.123 ± 0.02 0.104 ± 0.08
$\Lambda K^+ \pi^-$	1.14	0.076 ± 0.055
$\Sigma^+ K^0 \pi^-$	1.29	0.193 ± 0.003 0.010 ± 0.0012
$\Sigma^0 K^0 \pi^0$	1.28	0.034 ± 0.011^1
$\Sigma^- K^0 \pi^+$	1.305	0.0251 ± 0.0022 0.052 ± 0.006
$\Sigma^- K^+ \pi^0$	1.29	0.0138 ± 0.0014
$\Sigma^0 K^+ \pi^-$	1.29	0.0111 ± 0.003 0.0191 ± 0.0019
$\Lambda K^0 2\pi$	1.42	0.0017 ± 0.0012
$p K^0 K^-$	1.49	0.0118 ± 0.0053 0.0029 ± 0.0009
$n 2 K^0$	1.507	0.029 ± 0.011 0.0129 ± 0.005
$n K^+ K^-$	1.495	0.011 ± 0.006^1
$n \phi$	1.559	0.029 ± 0.015

Table F.1: Production cross section for strange particles in pion induced reaction. The values are taken from [LanBor]. Different values for the same channel originate from different measurements. Cross section units: $10^{-27} \text{ cm}^2 = \text{mb}$.

¹Measured at $p_{\pi^-} = 1.59 \text{ GeV}/c$.

Bibliography

- [Aich91] J. Aichelin, Phys. Rep. **202** (1991) 233.
- [Aka02] Y. Akaishi, T. Yamazaki, Phys. Rev. C **65**, 04405 (2002).
- [Bare97 a] E877, J. Barette *et al.*, Phys. Rev. C **56**, (1997) 3254, nucl-ex/977002.
- [Bare97 b] E877, J. Barette *et al.*, Phys. Rev. C **55**, (1997) 1420.
- [Baz11] M. Bazzi *et al.*, Phys. Lett. B **704**, (2011) 113-117.
- [Ben09] M.L. Benabderrahmane *et al.*, Phys. Rev. Lett. **102**, 182501 (2009).
- [Ben07] M.L. Benabderrahmane Ph.D. thesis, University of Heidelberg (2007).
- [Bat97] C.J. Batty, E. Friedmann, A. Gal, Nucl. Rep. **287** (1997) 385.
- [Blä93] B. Blättel, V. Koch and U. Mosel, Rept. Prog. Phys., **56** (1993) 1-62.
- [Bor02] B. Borasoy, R. Lewis, P.P. Ouimet, Phys. Rev. D **65** (2002) 114023.
- [Bor99] B. Borasoy, Eur. Phys. J. C **8** (1999) 121.
- [Bro96 I] G.E. Brown, M. Rho, Phys. Rep. **269** (1996) 333.
- [Bro96 II] G.E. Brown, M. Rho, Nuclear Phys. A **596** (1996) 503.
- [Böhmer Ph.D.] F.V.Böhmer, Ph.D. thesis, Technische University München (2015).
- [Brat97] E. Bratkovskaya, W. Cassing, U. Mosel, Nucl. Phys. A **622** (1997) 653.
- [Cas97] W. Cassing and E. Bratkovskaya, U. Mosel, S. Teis and A. Sibirtsev, Nucl. Phys. A **614** (1997) 415.
- [Cas99] W. Cassing and E. Bratkovskaya, Phys. Rep. **308** (1999) 65.
- [Cas03] W. Cassing, L. Tolos *et al.*, Nucl. Phys. A **727**, 59 (2003).
- [Cro00] P. Crochet *et al.*, Phys. Lett. B **486** (2000) 6-12.
- [Dan01] P. Danielewicz *et al.*, nucl-th/0112006 (2001).
- [DanOd85] P. Danielewicz and G. Odyniec, Phys. Lett. B **157** (1985) 146.

- [Dem10] P. B. Demorest, T. Pennucci, S. M. Ransom, M. S. E. Roberts, J. W. T. Hessels *Nature* **467**, 1081–1083 (2010).
- [Don96] S.J. Dong, J.F. Lagae, K.F. Liu, *Phys. Rev. D* **54** (1996) 5496.
- [Fin01] Ch. Finck, Seminar presented at INPL, LPC, CSNSM, Subatech, France, 2001.
- [Fuc06] C. Fuchs, *Prog. Part. Nucl. Phys.* **56** (2006) 1-103.
- [Gel68] M. Gell-Mann, R. Oakes, B. Renner, *Phys. Rev.* **175** (1968) 2195.
- [Gob93] A. Gobbi *et al.*, *Nucl. Instrum. Methods A* **324** (1993) 156-176.
- [Gol97] Ye.S. Golubeva, L.A. Kondratyuk, W. Cassing, *Nucl. Phys. A* **625** (1997) 832-854.
- [Har12] M. Hartmann, *et al.*, *Phys. Rev. C* **85** (2012) 935206.
- [Hart98] C. Hartnack and J. Aichelin, *J. Phys. G* **28** (2002) 1649-1656.
- [Hart95] C. Hartnack, nucl-th/0507002.
- [Hoe83] H. Höhler, Pion-nucleon scattering (ed. H. Schopper), Landolt-Börnstein, volume 9, Springer, Berlin, 1983.
- [Hon98] B. Hong *et al.*, *Phys. Rev. C* **57**, 244(1998).
- [Ino04] T. Inoue, V.E. Lyubovitskij, T. Gutsche, A. Faessler, *Phys. Rev. C* **690** (2004) 035207.
- [Ish05] T. Ishikawa *et al.*, *Phys. Lett. B* **608** (2005) 215.
- [Ita00] K. Itahashi *et al.*, *Phys. Lett. C* **62** (2000) 025202.
- [Iva81] P.M. Ivanon *et al.* *Phys. Lett. B* **107** (1981) 297-300.
- [Kai95] N. Kaiser, P.B. Siegel, W. Weise, *Nuclear Phys. A* **594** (1995) 325.
- [Kai97] N. Kaiser, T. Waas, W. Weise, *Nuclear Phys. A* **6120** (1997) 297.
- [Kan10] T.I. Kang, Ph.D. thesis, Korea University (2010).
- [Kap86] D.B. Kaplan and A.E. Nelson, *Phys. Lett. B* **175**, 57 (1986).
- [Kar01] F. Karsch, E. Laermann, A. Peikert, *Nucl. Phys. B* **605** (2001) 579-599.
- [Kas07] M. Kaskulov, E. Hernandez, E. Ose *EPJA* **31** (2007) 245.
- [Kis10] M. Kis *et al.*, *Nucl. Instr. Meth. A* **646** (2011) 27.
- [Kli98] F. Klingl, T. Waas, W. Weise, *Phys. Lett. B* **431** (1998) 254-262.

- [Koc97] V. Koch Int.J.Mod.Phys. E **6** (1997) 203-250.
- [Kol95] E.E. Kolomeitsev, D.N. Voskresensky, B. Kämpfer, Nuclear Phys. A **588** (1995) 889.
- [Kot08] M. Kotulla *et al.*, Phys. Rev. Lett. **100** (2008) 192302.
- [KPia] K. Piasecki, private communication.
- [LanBor] Landolt-Bornstein, New Series I/12a.
- [Lat07] J. Lattimer and M. Prakash, Phys. Reports **442** (2007) 109.
- [LBen] M.L. Benabderrahmane, private communication.
- [Lut02] M.F.M. Lutz, E.E. Kolomeitsev, Nuclear Phys. A **700** (2002) 193.
- [Mar01] E. Marco and W. Weise, Phys.Lett. B **502** (2001) 59.
- [Mul90] A. Müller-Groeling, K. Holinde, J. Speth, Nuclear Phys. A **513** (1990) 557.
- [Mueh06] P. Mühlich and U. Mosel, Nuclear Phys. A **765** (2006) 188.
- [Nan13] M. Nanova *et al.*, Phys. Lett. B **727** (2013) 427.
- [Nan12] M. Nanova *et al.*, Phys. Lett. B **710** (2012) 600.
- [Nan10] M. Nanova *et al.*, Phys. Rev. C **82** (2010) 035209.
- [Nas07] R. Nasseripour *et al.*, Phys. Rev. Lett. **990** (2007) 262302.
- [Nar06] M. Naruki *et al.*, Phys. Rev. Lett. **96** (2006) 092301.
- [Nel87] A.E. Nelson, D.B. Kaplan, Nuclear Phys. Lett. B **192**, (1987) 193.
- [Olli97] J.-Y. Ollitrault, arXiv:nucl-ex/9711003v2.
- [Pia16] K. Piasecki *et al.*, arXiv:1602.04378 [nucl-ex].
- [PDG] <http://pdg.lbl.gov/2010/reviews/rpp2010-rev-kinematics.pdf>
- [Pol11] A. Polyanski *et al.*, Phys. Lett. B **695** (2011) 74.
- [PJ09] Physik Journal 8 Nr.3.
- [PurAic00] R. K. Puri and J. Aichelin, J. Comput. Phys. **162**, 245 (2000).
- [Ram00] A. Ramos, E. Oset, Nuclear Phys. A **671** (2000) 481.
- [Rit95] J. Ritman *et al.*, Nucl. Phys. B **44** (1995) 708.
- [Scha97] J. Schaffner-Bielich, J.Bondrof, I.N. Mishustin, Nucl. Phys. A **625** (1997) 325.

-
- [Scha01] J. Schaffner-Bielich, J. Phys. G **27** (2001) 337.
- [Sik00] B. Sikora *et al.*, Acta Phys. Polon. B **31** (2000) 135.
- [Sch91] R. Schlesier, Master's thesis, Universität Heidelberg, 1991.
- [Suz04] Suzuki *et al.*, Phys. Rev. Lett. **92** (2004) 072302.
- [Thi13] M. Thiel *et al.*, Eur. Phys. J. A **490** (2013) 132.
- [Tol01] L. Tolos, A. Ramos, A. Polls, T.T.S. Kuo, Nuclear Phys. A **690** (2001) 547.
- [Tol02] L. Tolos, A. Ramos, A. Polls, Phys. Rev. C **65** (2002) 054907.
- [Tsu98] K. Tsushima, K. Saito, A.W. Thomas, S.V. Wright, Phys. Lett. B **429** (1998) 239.
- [Uhl05] F. Uhling, *et al.*, Phys. Rev. Lett., **95**, 012301 (2005).
- [Waa96] T. Waas, M. Rho, W. Weise, Nuclear Phys. A **617** (1996) 449.
- [Wei12] W. Weise Prog. Part. Nucl. Phys. **67** (2012) 299.
- [VolZha96] S. Voloshin and Y. Zhang, Z. Phys. C **70** (1996) 665.
- [VZDTh] V. Zinyuk, Diploma Thesis, University of Heidelberg (2011).
- [Zin14] V. Zinyuk *et al.*, Phys. Rev. C **90**, 025210 (2014).

List of Figures

2.1	Quark condensate as function of temperature and density	12
2.2	In-medium energy shift and effective mass of K^+ and K^- mesons . . .	15
2.3	In-medium energy shift of K^- mesons	16
2.4	Spectral function of $\phi \rightarrow e^+e^-$ in vacuum	17
2.5	P_Z and P_t distribution for ϕ decaying in- and outside the lead nucleus .	17
3.1	Configuration of the FOPI Detector	22
3.2	Schematic view of the FOPI detector in the y-z plane	24
3.3	Energy loss-momentum and momentum-velocity correlations, S325e . .	26
3.4	Sketch of the trigger system	28
3.5	Triggered cross section as a function of the run number, S325(e)	29
3.6	Triggered cross section as a function of the run number, S339	31
4.1	S325e ToF mass spectrum	34
4.2	PID diagrams for K^+ meson in the S325e experiment	36
4.3	PID diagrams for K^- meson in the S325e experiment	36
4.4	Momentum-selected RPC mass distributions for the PID of K^- mesons in S325e, part 1	37
4.5	Momentum-selected RPC mass distributions for the PID of K^- mesons in S325e, part 2	38
4.6	Phase space distribution of K^+ and K^- mesons in S325e	39
4.7	Ollitrault correction factors as a function of event's multiplicity	43
4.8	Characterisation of centrality selection	45
4.9	IQMD, v_1 vs p_t , for different centrality selection methods	47
4.10	Influence of the Coulomb interaction on the HSD predictions of v_1 . . .	49
4.11	SACA after-treatment of the directed K^+ flow, differential	50
4.12	SACA after-treatment of the directed K^+ flow, integrated	51
4.13	v_1 and v_2 vs y_0 for $K^{+/-}$ mesons in comparison to HSD and IQMD . .	52
4.14	v_1 vs p_t for K^+ mesons in comparison to HSD and IQMD	54
4.15	v_1 vs p_t for K^+ mesons in a central event selection	55
4.16	v_2 vs y_0 for $K^{+/-}$ mesons in comparison to the KaoS results	56
4.17	v_2 vs y_0 for $K^{+/-}$ mesons in comparison to the KaoS results and transport calculations	57

5.1	Momentum distribution ratio of K_S^0 mesons from pion induced reactions at $p_{\pi^-} = 1.15$ GeV/ c	59
5.2	S339: Energy loss as a function laboratory momentum for C, Cu und Pb	61
5.3	S339: Momentum-velocity correlation for C, Cu und Pb	61
5.4	S339: ToF-mass spectrum	63
5.5	S339: Mass distribution of negatively charged particles, differentiated by momentum	64
5.6	S339: ‘Best case’ and ‘worst case’ BG description	65
5.7	S339: Phase space distribution of charged K mesons	66
5.8	Pb/C-ratio of the momentum distributions for K^+ and K^-	67
5.9	Invariant mass distribution of ϕ candidates	71
5.10	Localisation of ϕ candidates in the phase space	72
5.11	Input ϕ distribution to the MC simulations	72
5.12	Result of the Geant simulations for the ϕ meson	73
5.13	Reconstruction efficiency of the ϕ meson in different phase space cells	75
5.14	Reconstruction efficiency of the ϕ meson as a function of p_t	76
5.15	The invariant mass distribution of Λ candidates	78
5.16	Invariant mass distribution of Λ candidates for various momentum selections	79
5.17	Kinematic variables of Λ candidates for the background study	80
5.18	Kinematic variables for the Λ signal	80
5.19	S339: Phase space distribution of Λ candidates	81
5.20	Momentum ratio for Λ baryons	82
5.21	Invariant mass spectrum of K_S^0 candidates	84
5.22	Influence of the optimised selection on the K_S^0 identification	85
5.23	Influence of the optimised selection on the dynamic variables of K_S^0	86
5.24	Invariant mass distribution of K^0 in various momentum bins	87
5.25	Differences in K^0 rec. efficiency in lead and carbon at $p_{\pi^-} = 1.15$ GeV/ c	88
5.26	Differences in K^0 rec. efficiency in lead and carbon at $p_{\pi^-} = 1.7$ GeV/ c	88
5.27	Phase space distribution of K^0 meson candidates	90
5.28	Kinematic variables of K^0 meson candidates	90
5.29	Momentum distribution ratio of K^0 with and without trigger selection	91
5.30	Cross section ratio of K^0 as a function of momentum	91
5.31	The <i>ratio</i> observable of K_S^0 mesons in comparison to HSD	92
5.32	The <i>ratio</i> observable of $K^{+/-}$ mesons in comparison to HSD	93
B.1	Reconstruction efficiency of K_S^0 meson	111
B.2	MC input phase space distribution of K^0	112
B.3	MC output phase space distribution of K^0	112
B.4	S339 Mass spectra for K^+ identification, Carbon	113
B.5	S339 Mass spectra for K^+ identification, Lead	114

List of Tables

3.1	Geometrical acceptance of FOPI's sub-detectors	25
3.2	Technical characteristics of the S339 experiment	30
3.3	Physical properties of targets used during the S339 runtime	30
3.4	Trigger conditions of the S339 runtime	31
4.1	Production channels of charged kaons in heavy-ion collisions.	33
4.2	Properties of charged kaons, identified in S325	37
4.3	Definition of centrality classes	46
4.4	In-medium potentials as employed in presented HSD and IQMD calculations	48
5.1	Production channels of strange particles in π^- -induced reactions	60
5.2	Properties of kaons identified in the S339 experiment	65
5.3	Selection criteria for ϕ reconstruction	68
5.4	Selection criteria for K_S^0 preselection	69
5.5	Selection criteria for Λ reconstruction	69
5.6	Reconstructed ϕ meson candidates, sorted by trigger condition	70
5.7	Relevant quantities for the calculation of the ϕ production cross section	76
5.8	Properties of reconstructed Λ baryons	77
5.9	K^0 signal under different trigger conditions	83
5.10	Optimised selection criteria for K_S^0 candidates	85
F.1	Production cross section in pion induced reactions	121

List of Abbreviations

a.u.	arbitrary units
BAR	plastic scintillator BARrel
B.R.	Branching Ratio
BUU	Boltzmann-Uehling-Uhlenbeck
ChPT	Chiral Perturbation Theory
CDC	Central Drift Chamber
GOR	Gell-Mann-Oakes-Renner
GEM	Gas Electron Multiplier
GSI	Gesellschaft für Schwerionenforschung
HSD	Hadron String Dynamics
IQMD	Isospin Quantum Molecular Dynamics
LHC	Large Hadron Collider
MC	Monte Carlo
PID	Particle IDentification
PLAWA	PLastic Wall
QED	Quantum ElectroDynamics
QFT	Quantum Field Theory
QCD	Quantum ChromoDynamics
QMD	Quantum Molecular Dynamics
r.m.s.	root mean square
RPC	Resistive Plate Chamber
SIS	Schwerionen-Synchrotron
TOF	Time-Of-Flight
TPC	Time Projection Chamber

Acknowledgement

My sincerest gratitude goes to my supervisor Prof. Dr. Norbert Herrmann! You have always inspired me with your passion for physics, enthusiastic discussions and the rational way of thinking. I have learned a lot from working with you. Your patience, optimism and help are very much appreciated!

Dear Yvonne Leifels, thank you for your support, help and fruitful discussions.

Thank you dear Elena Bratkovskaya and Christoph Hartnack for providing the transport calculation and for your willingness to discuss and to develop solutions.

Thank you Arnaud Le Fèvre for the collaboration on the SACA analysis.

I am very grateful to my family Alla, Marina, Daniil, Max, Sergej and Stas. I have always felt supported, encouraged and loved. Thank you!

Thank you Krzysztof (Chris) Piasecki for always being helpful and enthusiastic! I have enjoyed and appreciated working with you.

Special gratitude goes to my fellow colleagues Ingo Martin Deppner, Pierre-Alain Loizeau, Christian Simon, Felix Böhmer and Sverre Dørheim for a friendly working space and a good time.

Thank you Laura Fabbietti for motivating discussions. Your enthusiasm was very contagious!

Thank you Britta Dittkris and Lukas Ofer for proofreading the manuscript and the encouragement.

I feel privileged to work in such friendly and motivating environment. Thank you all for caring!